Absract

In this work we wanted to underline the importance of Thermal Desorption Spectroscopy and its applications to several branches of Physics.

Temperature-programmed desorption techniques (TPD) are important to determinate kinetic and thermodynamic parameters of desorption processes and decomposition reactions.

Knowledge of the nature of the desorption process is fundamental to understand the nature of the elementary chemical processes of adsorbates, as the energetics of bonding, the specification of the chemical nature of the bound species and the nature and magnitude of interactional effect between adsorbed species.

We focused our attention on the applications of Thermal Desorption Spectroscopy (TDS) to High-Energies Physics, Astrophysics and Geophysics; in fact this technique was used, respectively, to investigate the molecular hydrogen adsorption on carbon nanotubes, the effects of electron bombardment on ammonia and methane ices and changes of zoisite mineral after heating.

The molecular hydrogen adsorption on carbon nanotubes was studied to find a possible solution to vacuum system problems of Large Hadron Collider (LHC); in fact, the circular path of photon beams produces synchrotron radiation which deteriorates LHC vacuum desorbing gas molecules from the ring walls. Among the desorbed species the most problematic to pump out is H_2. Since LHC elements operate at low temperatures, a possible solution to vacuum problem is the installation of cryosorbent materials on the LHC walls. In this work we study the possibility to use carbon nanotubes as criosorbers in future accelerators. Our sample, furnished by Prof. Nagy group of Chemical Engineering Department of Calabria University, is constituted by MWNTs synthesized by chemical vapor deposition using C_2H_4 and subsequently purified. Our investigations confirm that the carbon nanotubes have a great adsorption capacity also at low temperatures both for H_2 and noble gases as Kr; then we observed that H_2 adsorption on CNT is described by a first kinetic-order, while Kr adsorption is characterized by a zero kinetic-order. By means of TDS we calculate the activation energy for H_2 adsorption on carbon nanotubes and we found a value of about 3KJ/mol, perfectly coherent with theoretic one. Moreover, from a comparison between nanotubes and other carbon-based material (as charcoal), we noted that adsorption efficiency for CNT is almost an order of magnitude higher then charcoal. So carbon nanotubes are good candidates to cryosorbers in future accelerators.

As Thermal Desorption Spectroscopy application to Astrophysics we studied the effect of electron bombardment on ammonia and methane ices. The interstellar medium is composed for 99% by gas; molecules, atoms and radicals at gas state condense on dust grains surface of molecular clouds (at 10 K) creating an icy mantle with a thickness of 0.1 μm. The presence of ices is confirmed by IR spectroscopy of obscured stellar sources and in interstellar grains are localized solid mixture containing H_2O, CO, CH_4 and NH_3**.** In these environments ices are subjected to chemical and physical processes, specifically to bombardment of photons and cosmic rays, with the consequent synthesis of new organic species

In this work we conducted an investigation of the chemical processing of ammonia and methane ices subjected to energetic electrons. By Thermal Desorption Spectroscopy we verify the production of new organic species, after energetic irradiation in interstellar ices, as diazene (N_2H_2), ethane (C_2H_6) and acetylene (C_2H_2).

Finally, in Geophysics and Petrology Thermal Desorption Spectroscopy can be used to study minerals chemical composition. Our interest was focused on zoisite and the sample investigated was furnished by prof. Ajò from "Institute of Inorganic Chemistry and Surfaces" of CNR, in Padova. In this work we used TDS to investigate zoisite behaviour during heating form room temperature to 650^{o}C and to understand if its modification into tanzanite variety after heating is due to structural changes or to a dehydration mechanism.

Chapter 1

Thermal desorption spectroscopy

1.1 Adsorption and Desorption fundamental principles

Temperature-programmed desorption techniques (TPD) are important to determinate kinetic and thermodynamic parameters of desorption processes and decomposition reactions.

Knowledge of the distinctive features is fundamental to understand the nature of the elementary chemical processes of adsorbates, as the energetics of bonding, the specification of the chemical nature of the bound species and the nature and magnitude of interactional effect between adsorbed species**[1]**.

Adsorption takes place when attractive interaction between a particle and a surface is strong enough to overcome thermal disorder effects.

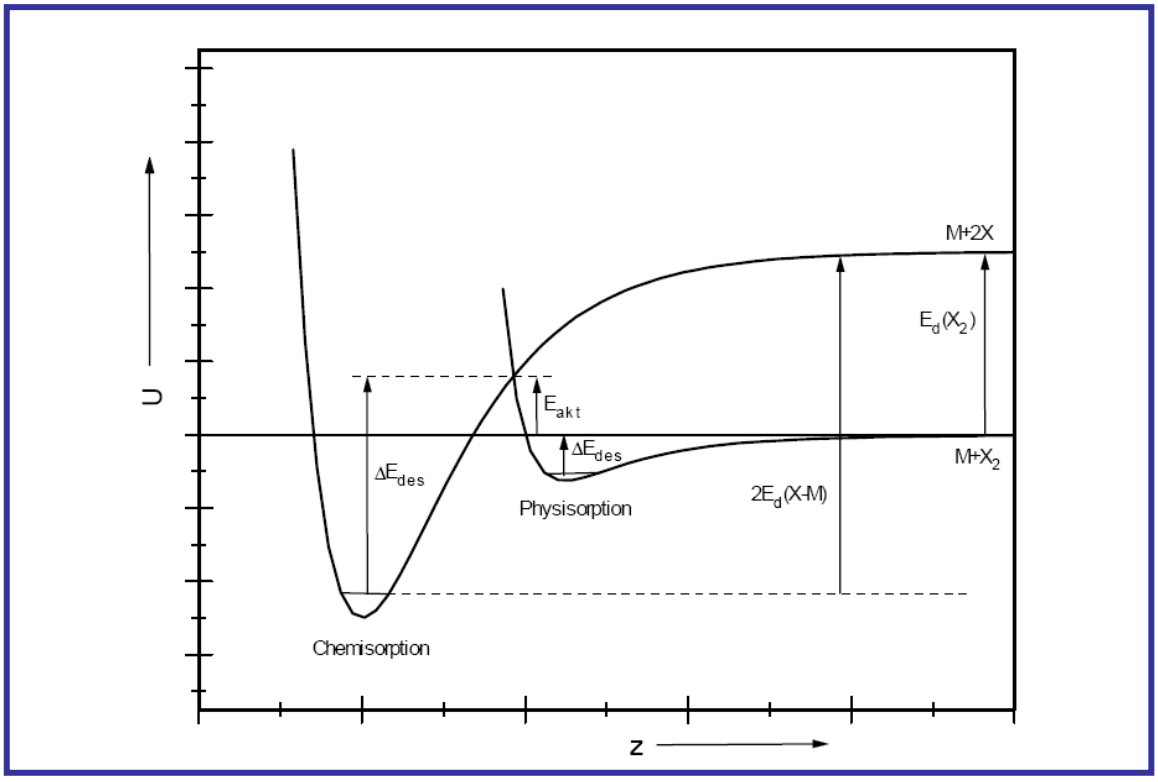

Fig. 1.1. Adsorption potential diagram for a diatomic molecule X_2 interacting with a substrate surface along the direction z. Physisorption potential has been described through the Lennard-Jones potential, while chemisorption has been represented by a Morse potential

The weakest form of adsorption to a solid surface is called “physisorption”. It takes place if the interaction is mainly due to the ubiquitous van der Waals interaction and typical binding energies are lower than 50kJ/mol. On the contrary, if gas particles that strike the surface bind to it through the formation of a surface chemical bond “chemisorption” occurs and typical binding energies are higher than 50 kJ/mol and comparable to a fraction of the substrate sublimation energy. Moreover we should remark that chemisorption is an activated process, i.e. the formation of a chemisorptive bond requires the overcoming of an activation barrier.

1.2 Adsorption and desorption kinetics

1.2.1 Adsorption isotherms

Theories from which arise studies about adsorption and desorption phenomena are essentially based on the following principles:

- Adsorption is a localized phenomenon, i.e. absorbed particles are motionless
- The substrate surface is saturated when all its adsorption sites are occupied, so a monolayer is formed : $\Theta = 1ML$,

with

$$\Theta = N_{ads} / N_{surf} , \tag{1.1}$$

where N_{ads} is the adsorption particles number , while N_{surf} represents the number of adsorption sites on surface.

- There is not interaction between adsorbed particles.

Adsorption is usually described through isotherms, that is, the amount of adsorbate on the adsorbent as a function of its pressure at constant temperature. The most important adsorption isotherm in the analysis of adsorption/desorption phenomena is the Langmuir isotherm, described through the following set of equations:

$$\begin{aligned} r_{ad}(\Theta) &= A_n p(1-\Theta)^n \\ r_{des}(\Theta) &= B_n \Theta^n \end{aligned} , \tag{1.2}$$

with A_n and B_n constants, n=1,2 and $r_{ad/des}$ the adsorption/desorption rate.

From the dynamic equilibrium condition, $|r_{ad}| = |r_{des}|$, it follows that:

$$\Theta_n = \frac{(b_n p)^{1/n}}{1+(b_n p)^{1/n}}. \tag{1.3}$$

For n=1 it is possible to observe an adsorption/desorption first order which corresponds to a sort of condensation process of adsorbed molecules on the surface, while for n=2 there is a second order process, which corresponds to a dissociative adsorption and to a recombining desorption for diatomic molecules. Moreover molecules dissociation can be reduced decreasing surface temperature.

Other common desorption isotherms are the Freundlich (4) and Brunauer, Emmett e Teller isotherms (BET)

$$\Theta_n = \alpha\, p^{\beta}, \quad \text{with } 0.2<\beta<1.0 \tag{1.4}$$

$$\frac{p}{(p-p_0)\gamma} = \frac{1}{C\gamma_{\max}} + \frac{C-1}{C\gamma_{\max}} \cdot \frac{p}{p_0}, \tag{1.5}$$

where

p_0 = vapour pressure of purely liquid phase at fixed temperature

C = system specific constant

γ = adsorption molality, $\gamma = N_{ads}/(m_A \cdot N_L)$ (1.6)

γ_{max} = the maximum molality that can be achieved whit a monoatomic layer

m_A = mass of the adsorbed particle.

The Bet isotherm extends the assumptions of Langmuir isotherm to multiple layers. It is hypothesized that only the first monoatomic layer is bonded to substrate surface and that, consequently, all the adsorbed layers are characterized by the same bonds that correspond to adsorbed molecules in liquid phase. This model describes chains of not interacting adsorbed molecules that grow perpendicularly to surface, so it is assumed that each molecule of the chain has coordination number of 2. For multiple coverages results achieved from BET isotherm are very different from experimental isotherms **[2]**.

1.3 Polanyi-Wigner equation

Adsorption of gaseous molecules on a solid surface, with pressure and temperature fixed, is governed by the equality of the chemical potential of the adsorbed layers and of the gas

$$\mu_{ad}(N) = \mu_{gas}(P,T),$$

where N is the number of molecules adsorbed on surface, characterized by a total number of adsorption sites of N_0.

The chemical potential of the adsorbed species is usually calculated through different techniques (ex. density functional method), while $\mu_{gas}(P,T)$ can be obtained by thermal dynamics consideration.

For a gas the Gibbs free Energy is defined as

$$G= H- TS = U + PV-TS, \tag{1.7}$$

where H ,S and U are respectively the enthalpy, the entropy and the energy of the system.

For isothermal adsorption at a temperature T_{ad} dG= VdP, so

$$\int_{G0}^{G} dG = \int_{P0}^{P} VdP \ , \tag{1.8}$$

from which

$$G = G_0 + \int_{P0}^{P} VdP \, . \tag{1.9}$$

The chemical potential is defined as the molar Gibbs free energy μ=dG/dn, so

$$\mu = \mu_0 + \int_{P0}^{P} \frac{V}{n} dP \, . \tag{1.10}$$

For an ideal gas

$$\mu = \mu_0 + RT_{ad} \ln \frac{P}{P_0}, \tag{1.11}$$

where μ_0 is the chemical potential at the reference pressure P_0.

If the gas is not ideal is necessary to calculate the integral in equation (1.10) using the equation of the state. For example, for the van der Waals interaction, V can be expressed as a series of P:

$$V = nRT(\frac{1}{P} + b + cP), \tag{1.12}$$

where the virial coefficients b and c are temperature dependent and the values can be found in literature.

The desorption rate is usually expressed through a law of n^{th} (with n = 0,1,2):

$$r_{des} = -\frac{d\Theta}{dt} = k_n \cdot \Theta^n \tag{1.13}$$

If the rate constant k_n is described by Arrhenius equation

$$k_n = \nu_n \cdot \exp\left(-\frac{\Delta E_{des}^{PW}}{RT}\right) \quad , \tag{1.14}$$

with ν_n = desorption frequency, equation (1.13) becomes:

$$r_{des} = -\frac{d\Theta}{dt} = \nu_n \cdot \exp\left(-\frac{\Delta E_{des}^{PW}}{RT}\right) \cdot \Theta^n \ , \tag{1.15}$$

that define the activation Energy of desorption ΔE_{des}^{PW} and it is important in the interpretation of the experimental spectra.

It is useful to observe the differences between the three kinetic orders:

i)Zero kinetic order 0 (n=0)

- Desorption rate is not dependent on coverage.
- Desorption exponentially increases with T.
- When dose increases the desorption peak moves to higher temperatures (fig.1.2).

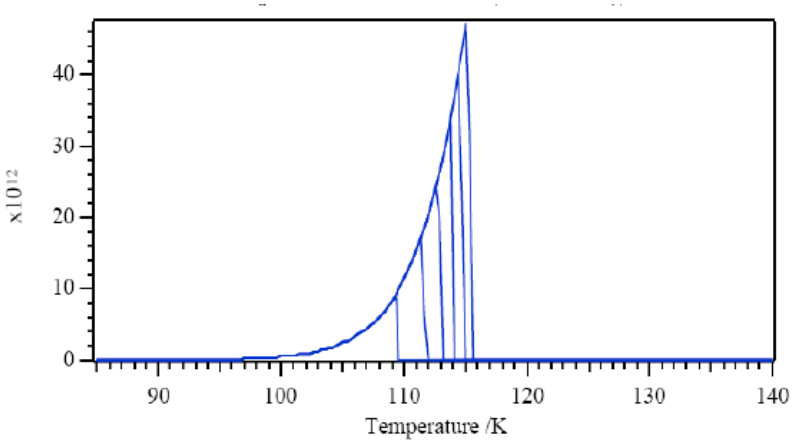

Fig. 1.2. Representation of a zero-order kinetic

ii) First kinetic order (n=1)

- Desorption rate is directly proportional to coverage.
- When coverage increases the temperature at which the maximum of the peak occurs does not vary (fig.1.3).
- The peak is asymmetrical.

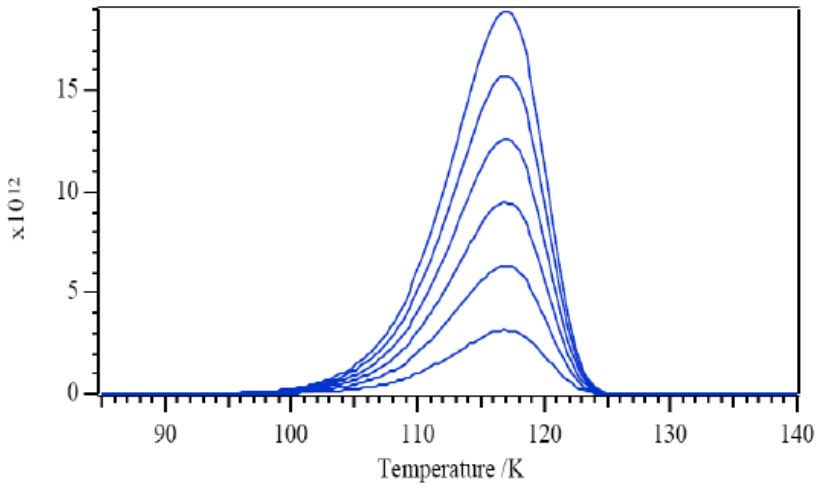

Fig. 1.3. First-order kinetic

iii) Second kinetic order (n=2)

- Desorption rate varies with the square of the coverage.
- The temperature at which maximum of the peak occurs increases with decreasing of the coverage (fig.1.4).
- The peak is symmetrical.

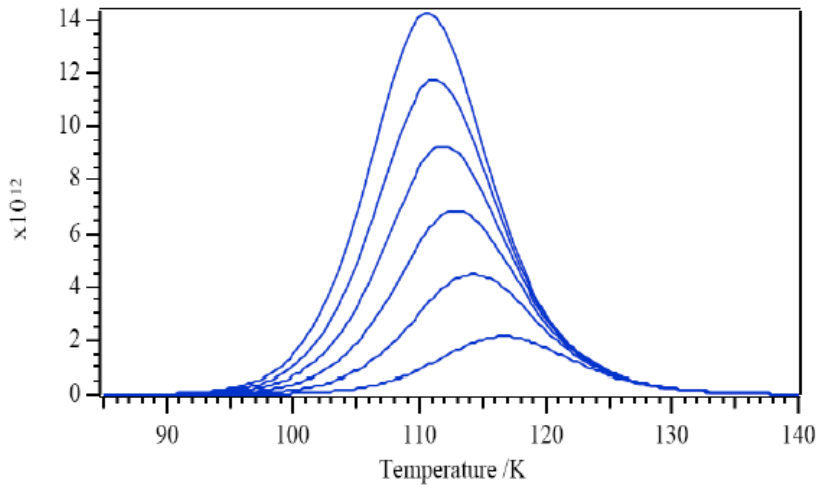

Fig. 1.4. Second-order kinetic

Zero-order kinetics are often indicative of desorption from a multilayer where the rate of desorption is independent on surface coverage; first-order kinetics may be indicative of the presence of a single surface species; second-order kinetics are an indication of adsorbate atom recombination process leading to the production of ~~a~~ diatomic molecules.

A fundamental condition to determinate a thorough set of data is that the observed desorption signal is proportional to desorption rate; each step of the desorption process has to take place more slowly than any secondary reaction involved (rate-limiting).

In equation (1.15) it is possible to note that the activation parameters depend generally from the coverage, but often it is possible a dependence from temperature, in particular a dependence from the heating rate β, an experimental parameter. So it is reasonable to think that thermal desorption technique gives information about nature of adsorbed molecules in conditions very distant from equilibrium and at temperatures lower than desorption temperature; as a consequence the Polany-Wigner equation can result insufficient for analysis and it is possible to couple with it equations based on simulation of desorption spectra with complex statistic models to describe the interactions of adsorbates **[2].**

1.3.1 Material balance equation for Thermal Desorption in a vacuum system

The basic equations for the measurement of thermal desorption spectra are given below **[1]**.

The desorption rate (R_d) of a species from a surface should be a function of the surface concentration N and of the temperature T of the species. The Arrhenius form is

$$-\frac{dN}{dt} = R_d = \nu_0^{(n)} N^n e^{-E_d/(kT)}, \tag{1.16}$$

where $\nu_0^{(n)}$ is the pre-exponential factor, n the desorption order (usually n=0,1,2) and E_d the activation energy for desorption. It is often assumed as a first approximation that $\nu_0^{(n)}$ and E_d are constant, but it has been shown that in many cases these kinetic parameters vary with coverage N.

If the pumping speed of the system (s) is constant, if the pressure rise ΔP above the base pressure P_0 is used and if no adsorption/desorption processes occur on extraneous surface, the Redhead equation is **[6]**

$$\frac{d(\Delta P)}{dt} = \frac{kT}{V}\left(-A\frac{dN}{dt}\right) - \frac{s\Delta P}{V} \tag{1.17}$$

= (rate of the gas evolution) –(incremental pumping rate above steady state background rate).

Thus,

$$R_d = \frac{V}{AkT}\frac{d(\Delta P)}{dt} + \frac{s\Delta P}{AkT}, \tag{1.18}$$

which may be rewritten as

$$R_d \frac{AkT}{V} = \frac{d(\Delta P)}{dt} + \frac{\Delta P}{\tau}, \tag{1.19}$$

where $\tau = V/s$ is the characteristic pumping time of the system.

Defining a characteristic time δt for the desorption of a binding state, two limits exist:

- for $\tau >> \delta t$ the Eq.1.19 becomes

$$R_d = \frac{V}{AkT}\frac{d(\Delta P)}{dt}; \tag{1.20}$$

- for $\tau << \delta t$

$$R_d = \frac{V}{AkT}\frac{\Delta P}{\tau}. \tag{1.21}$$

For most situations involving vacuum system with fast pumping speed ($\tau \leq 0.25$s) and $\delta t \geq 2$s, Eq. (1.21) is applied conveniently and the pressure rise ΔP is a direct measure of the desorption rate R_d.

For intermediate cases it is convenient to use both terms in Eq. (1.19).

In a glass or metal ultrahigh-vacuum system it is possible to measure τ by rapidly opening or closing the leak valve for the gas admission or by producing a pulse of gas by rapid desorption from a filament and, subsequently, following the decay of pressure with time. It is often found that τ is not constant. This problem may be due to wall effect or to re-emission of gas from ion pumps or other element within the system.

Redhead **[7]** proposed a method to determinate that wall effects are absent in adsorption/desorption experiments under flow conditions. The pumping speed of a gas under molecular flow conditions (with no wall effects) is directly proportional to the molecular mean velocity and, for a Boltzmann distribution, it is therefore proportional to $(mT)^{-1/2}$, where m is the molecular mass.

1.4 Theories of Thermal desorption

1.4.1 The Mobile Precursor Model in Adsorption and Desorption

Several studies about chemisorption on surfaces have shown that the sticking coefficient remains nearly constant (and often near unity) over a wide coverage range. This observation has led to the postulate that in chemisorption is present a precursor state , that may sample both filled and empty adsorption sites as it migrate, until finally becoming chemisorbed **[1]**.
King **[3]** was the first to propose the passage through a mobile precursor state also in thermal desorption and he computed the influence that this process might have on the shape of thermal desorption spectra.
Gorte and Schmidt **[4]** have formulated a desorption kinetic model involving transition through a precursor state, illustrated below for first-order desorption kinetics.
For an adsorbed molecule A(s), the elementary reaction describing desorption process is

$$A(s) \underset{k_a}{\overset{k_d}{\rightleftharpoons}} A^* + \text{site} \xrightarrow{k^*} A(g) \tag{1.22}$$

where the k's represent first-order rate constants for the elementary steps.
If the precursor state A^* is in equilibrium with A(s) at coverage θ_s and it is at a low steady-state concentration during desorption, is it possible to write

$$d\theta_{A^*}/dt = k_d\theta_s - k_a\theta_{A^*}(1-\theta_S) - k^*\theta_{A^*} = 0 \tag{1.23}$$

and

$$d\theta_S/dt = -k^*\theta_{A^*} = -k^*k_d\theta_S/\left[k^* + k_a(1-\theta_S)\right]. \tag{1.24}$$

For $k^* >> k_a$ the first-order desorption kinetics is obtained

$$d\theta_S/dt = k_d\theta_s\ ; \tag{1.25}$$

while for $k^* << k_a$ we have

$$d\theta_S/dt = -k^*k_d\theta_S/\left[k_a(1-\theta_S)\right] \tag{1.26}$$

Using the rate expression, the equation (1.20) becomes

$$d\theta_S / dt = -\left[\nu^* \nu_d / \nu_a\right]\left[\theta_S /(1-\theta_S)\right] e^{-\left(E^* + E_d - E_a\right)/(RT)} \qquad (1.27)$$

The activation energy term in the exponential factor is just the total barrier height for the process going from A(s) to A(g), i.e. the heat of adsorption.

Fig. 1.5 show a comparison between the theoretically calculated first-order temperature-programmed desorption behaviour for a mobile precursor model and the normal first order desorption.

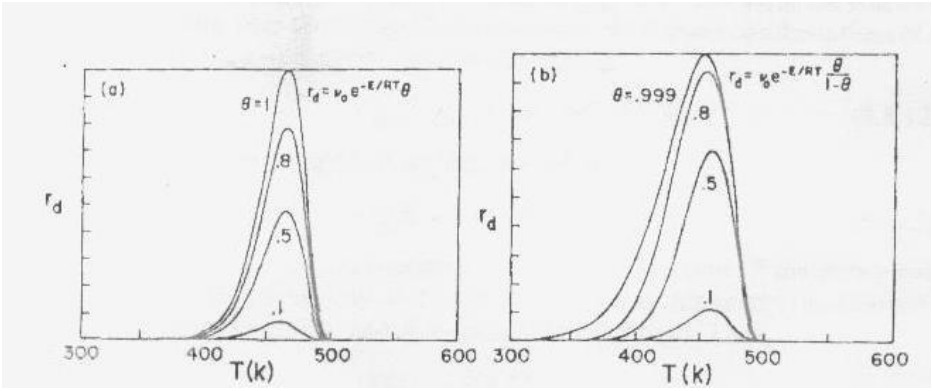

Fig. 1.5. (a)A normal first order desorption spectra, calculated assuming E_d=26 kcal mole^{-1}, $\nu_0^{(1)}$=10^{13} s^{-1} and β=100 K/s; (b)limiting case for single precursor.

Is it possible to note that the θ/(1-θ) factor in equation (1.27) causes a significant broadening of the desorption peak and a shift to lower temperature.

Thus if a mobile precursor is involved in desorption, estimates of pre-exponential factors and desorption energies from the peak shapes will be inexact, because of the dependence of these parameters on peak shape.

Dissociative adsorption, followed by second-order desorption via a mobile precursor, will introduce a $\theta^2/(1-\theta^2)$ term into Eq. (1.27), with a consequent desorption peak broadening and shifting to lower temperature.

So the mobility of the activated complex is an important factor to consider in some kinetic measurements of thermal desorption.

The absence of a precursor in condensation at low temperature implies the absence of a precursor expression for desorption and the presence of a precursor in condensation suggests that these expressions might be anticipated in desorption **[4]**.

1.4.2 Statistical Thermodynamics of Adsorption and Desorption

The Eyring theory of reaction rates **[5]** postulates that the reaction (adsorption or desorption) proceeds via an energetically activated state (or complex) that is intermediate in structure between the reactants and the products in the process under consideration. It exist at the top of a potential energy barrier whose height is the activation energy for the reaction process. Passage over the energy barrier occurs by motion along a path called the reaction coordinate, that describe the molecular configuration of the reactants and the products. The activated complex at the top of the barrier exists in low concentration in equilibrium with the reactants.

For adsorption on a uniform surface, let N^* be the equilibrium concentration of activated complexes (molecules cm^{-2}), N_S the number of adsorption sites per square centimeter and N_g the number of gas-phase molecules per cubic centimeter.

In an adsorption process in which a molecule is adsorbed without dissociation on the surface, the equilibrium constant is:

$$K^*(eq) = N^* / N_g N_s = f^{*'} / f_g f_s \ , \qquad (1.28)$$

where the three term *f* above are the complete partition functions for the species or for the site ($f = \sum_i g_i e^{-\varepsilon_i/(kT)}$ and g_i is the degeneracy of the quantum state of energy ε_i).

From Eq.(1.28) the activated complexes concentration is

$$N^* = f^{*'} N_g N_s / f_g f_s \ . \qquad (1.29)$$

The rate of the reaction is equal to the product of the concentration of activated complexes N^* and the frequency of crossing of the barrier. Let us assume that the activated complex exists in a region of length δ along the reaction coordinate at the top of the barrier. Using the Maxwell-Boltzmann statistics is it possible to determinate the average velocity for translation over the barrier ($\bar{v}$):

$$\bar{v} = \left(kT / 2\pi m^*\right)^{1/2}, \qquad (1.30)$$

where *m** is the effective mass of the complex. Thus the average time of crossing the barrier is

$$\tau = \delta/\bar{v} = \delta\left(kT/2\pi\, m^{*}\right)^{-1/2}. \tag{1.31}$$

Moreover it follows that the rate of transmission over the barrier is $K'N^{*}/\tau$, where K' is a transmission coefficient reflecting the probability of the activate complex of passing over the potential barrier. Thus,

$$-\frac{dN_g}{dt} = K' N^{*}/\tau = K'/\tau\,(f^{*'} N_g N_s / f_g f_s). \tag{1.32}$$

It is convenient to re-express the complete partition function $f^{*'}$ as $f^{*'}=f^{*}f^{*}_{trans,(1\text{-}dim)}$, where $f^{*}_{trans,(1\text{-}dim)}$ is the one-dimensional translation partition function corresponding to motion along the reaction coordinate, over the barrier. So, from mechanical consideration of a particle in a box of length δ, it follow that

$$f^{*}_{trans,(1-\dim)} = \left(2\pi\, m^{*} kT\right)^{1/2} \delta/h. \tag{1.33}$$

So the Eq. (1.32) becomes

$$-\frac{dN_g}{dt} = K' N^{*}/\tau = K' kT/h\,(f^{*} N_g N_s / f_g f_s). \tag{1.34}$$

It is convenient to make the zero-point energy of the initial state of the system the arbitrary zero reference energy and to redefine f^{*}. Thus,

$$-\frac{dN_g}{dt} = K' \frac{kT}{h} \frac{f^{*}}{f_g f_s} N_g N_s e^{-\varepsilon_1/(kT)}, \tag{1.35}$$

where ε_1 is the activation energy for the process.

This theory has been treated for the cases of immobile and mobile adsorption by Glasstone **[5]**.

So the rate of the first-order desorption via an activated complex is given by

$$\frac{dN_g}{dt} = K' \frac{kT}{h} \frac{f^{*}}{f_a} N_a e^{-\varepsilon_2/(kT)}, \tag{1.36}$$

where N_a and f_a refer to the adsorbed species and ε_2 is the activation energy for desorption of a single molecule, referred to the zero-point energy of the adsorbed species.

For the first-order kinetics of desorption in which both the adsorbate species and the activated complex are considered to be immobile, $f^*/f_a \cong 1$. Many experiments have shown that first-order desorption process exhibits pre-exponential factor of $K' \frac{kT}{h}$ magnitude.

For thermodynamics consideration is important to remember that

$$K^*_{(eq)} \equiv e^{-\Delta G^*_0/(RT)}, \tag{1.37}$$

where $\Delta G^*_0 \equiv \Delta H^*_0 - T\Delta S^*_0$ and ΔH^*_0 and ΔS^*_0 are respectively the activation enthalpy and entropy for formation of the activated complex from the reactants.

For the first-order desorption, with

$$K^*_{(eq)} = \frac{N^*}{N_a} = \frac{f^*}{f_a} e^{-\varepsilon_2/(kT)}, \tag{1.38}$$

the desorption rate is given by

$$\frac{dN_g}{dt} = K' \frac{kT}{h} e^{\Delta S^*_0/R} e^{-\Delta H^*_0/(RT)} N_a. \tag{1.39}$$

For a *n*-order desorption the equilibrium constant becomes

$$K^*_{(eq)} = N^* N_s^{(n-1)} \Big/ N_a^n, \tag{1.40}$$

where N_s is the number of sites per square centimeter.

So the general equation for the *n*th order desorption rate is:

$$\frac{dN_g}{dt} = \frac{K'}{N_s^{(n-1)}} \frac{kT}{h} e^{\Delta S^*_0/R} e^{-\Delta H^*_0/(RT)} N_a^n. \tag{1.41}$$

N_s is about 10^{15}cm^{-2} for most adsorbents. For little or no activation entropy ($\Delta S^*_0 \approx 0$) and for $K' \cong 1$, the pre-exponential factor $\nu_0^{(n)}$ is

$$\nu_0^{(n)} = kT/hN_s^{(n-1)} \,. \tag{1.42}$$

In the temperature range (50-2000)K, for first order kinetics, $10^{12} \le \nu_0^{(1)} (= kT/h) \le 4 \cdot 10^{13}\, s^{-1}$, while for the second order kinetics $10^{-3} \le \nu_0^{(2)} (= kT/(hN_s)) \le 4 \cdot 10^{-2}\, cm^2 s^{-1}$.

When the activated complex is characterized by two degrees of translational freedom, the two-dimensional translational partition function for a single particle is

$$f^*_{(2D,tr)} = \frac{2\pi mkT}{h^2} A, \tag{1.43}$$

where *A* is the total surface area available to the translating complex.

For N indistinguishable and independent particles , the canonical ensemble partition function is

$$F^*_{(2D,tr)} = \frac{1}{N!}\left(f^*_{(2D,tr)}\right)^N . \tag{1.44}$$

The Helmholtz free energy is given by

$$A^* \equiv E^* - TS^* \equiv -kT \ln F^* = -NkT \ln\left(\frac{2\pi mkT}{h^2}\frac{Ae}{N}\right). \tag{1.45}$$

So for a two-dimensional gas E^*=NkT,

$$S^*_{(2D,tr)} \equiv \frac{E^* - A^*}{T} = 2Nk + Nk \ln\left(\frac{2\pi mkT}{h^2}\frac{A}{N}\right), \tag{1.46}$$

with an increasing of the pre-exponential factor. Additional enhancement of the pre-exponential factor can occur if other degrees of freedom are permitted for the activated complex in desorption.

1.5 Treatment of experimental Desorption data

Experimental data can be treated with several methods. In this work we used the Heating Rate Variation Method, through which we obtain a value of activation energy for H_2 adsorption on carbon nanotubes absolutely coherent with the theoretic value.

1.5.1 Heating Rate Variation Method

Desorption spectra can be treated with several models. In this work we used the Heating Rate Variation Method, that is based on the collection of a series of spectra characterized by the same adsorbate coverage but different heating rates $\beta = dT/dt$ = const.
From each spectra it is possible to obtain the temperature corresponding to the maximum desorption rate (Tmax) and then the expressions related to first and second kinetic order.
From $dt = dT/\beta$ and substituting it in Polany Wigner equation (1.15):

$$-r_{des} = \frac{d\Theta}{dT} = -\frac{1}{\beta}\nu_n \cdot \exp\left(-\frac{\Delta E_{des}}{RT}\right)\cdot \Theta^n \quad , \qquad (1.47)$$

where r is the desorption rate.
Imposing at $T=T_{max}$ the maximum condition

$$\left.\frac{dr_{des}}{dT}\right|_{T\max} = 0 \qquad (1.48)$$

in equation (1.14) we obtain that

$$0 = \left.\frac{d^2\Theta}{dT^2}\right|_{T\max} = n\cdot\Theta^{n-1}\cdot\frac{d\Theta}{dT} + \Theta^n \cdot \frac{\Delta E_{des}}{RT_{\max}^2} \qquad (1.49)$$

So, from the expression for $d\Theta/dT$ in (1.13)

$$\frac{\Delta E_{des}}{RT_{\max}^2} = \frac{1}{\beta}\nu_n \cdot n \cdot \Theta^{n-1}\cdot\exp\left(-\frac{\Delta E_{des}}{RT}\right). \qquad (1.50)$$

The first kinetic order (n=1) is independent on the coverage, but dependent on the heating rate β:

$$\frac{\Delta E_{des}}{RT_{\max}^2} = \frac{1}{\beta}\nu_1 \cdot \exp\left(-\frac{\Delta E_{des}}{RT}\right). \tag{1.51}$$

Taking the logarithm of both parts of equation (1.51) , rearrangement yields:

$$\ln\frac{T_{\max}^2}{\beta} = \frac{\Delta E_{des}}{RT_{\max}} + \ln\frac{\Delta E_{des}}{\nu_1 \cdot R} \tag{1.52}$$

Plotting , $\ln(T_{\max}^2/\beta)$ as a function of *1/T*$_{max}$ for a series of heating rate values, it is possible to obtain ΔE_{des} and ν_1 respectively from the slope and the intercept with the ordinate of the line.
For the first kinetic order desorption depends on the heating rate β, but not on the coverage Θ; instead the last dependence is present in equation for the second kinetic order.
For the second kinetic order (n=2) instead, from (1.51) we obtain

$$\frac{\Delta E_{des}}{RT_{\max}^2} = \frac{2}{\beta}\nu_2 \cdot \Theta(T_{\max}) \cdot \exp\left(-\frac{\Delta E_{des}}{RT}\right) \tag{1.53}$$

The second order curves are asymmetrical with respect to T_{max}, so $\Theta_0 = 2\Theta(T_{max})$, where Θ_0 is the coverage value before desorption. So

$$\ln\frac{T_{\max}^2}{\beta} = \frac{\Delta E_{des}}{RT_{\max}} + \ln\frac{\Delta E_{des}}{\nu_2 \cdot R \cdot \Theta_0} \tag{1.54}$$

Plotting $\ln(T_{\max}^2/\beta)$ vs *1/T*$_{max}$ and if Θ_0 is known, it is possible to obtain ΔE_{des} from the slope and ν_2 from the intercept. Through this method we calculated an experimental value of the activation energy coherent with the theoretic value.
In figure 1.6 is showed the Polany-Wigner equation plot at the first kinetic order, for a tipical value of desorption activation energy. As previously written, the peak is clearly asymmetrical.

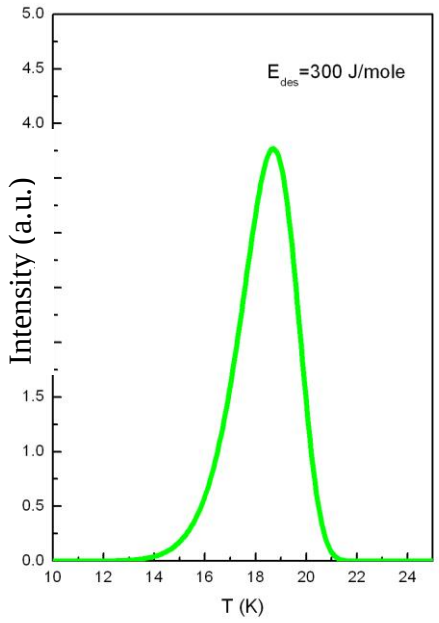

Fig. 1.6. Polanyi-Wigner plot: emission intensity as function of temperature for different activation energies, with β and E_{des} fixed.

1.5.2 Gas Evolution Method (constant Heating Rate)

Let consider a surface desorbing gas into a pumped ultrahigh-vacuum system, in which the average residence time for a gas molecule is τ. Equation (1.18) may be written, in a dimensionless, for as:

$$\frac{dP^*}{dt} + \frac{P^*}{\tau} = -\frac{1}{N_0}\frac{dN}{dt} \equiv g(T), \tag{1.55}$$

where P^* is a dimensionless quantity equal to P/P_{max} and P_{max} is the maximum pressure observed for desorption of N_0 molecules cm^{-2} into the same vacuum system with zero pumping speed ($\tau = \infty$); N_0 is the initial coverage on the surface.

For $\beta = dT/dt$ it is possible to obtain

$$P(T) = \exp\left(\frac{-T}{\beta\tau}\right)\frac{\nu_0^{(1)}}{\beta}\left[\int_0^T \exp\left[\frac{T}{\beta\tau} - \frac{E_d}{RT} - \frac{\nu_0^{(1)}R}{\beta E_d}T^2\exp\left(-\frac{E_d}{RT}\right)\right]dT\right], \tag{1.56}$$

where $\nu_0^{(1)}$ is the pre-exponential factor at the first-order (s^{-1}), E_d is the activation energy for desorption and R is the gas constant. P(T) describes the normalized profile of a desorption spectrum characterized by β, τ, $\nu_0^{(1)}$ and E_d.

To determinate the kinetic parameters $\nu_0^{(1)}$ and E_d it is convenient to utilize the following relationship, derived by Redhead:

$$\frac{E_d}{RT_p} = -\ln\frac{\nu_0^{(1)}T_p}{\beta} - \ln\frac{E_d}{RT_p}, \tag{1.57}$$

where T_p is the temperature at which the rate of desorption is maximum.

Since the experimental desorption peak maximum temperature $T_m \approx T_p$ it is useful to determinate pairs of the parameters $\nu_0^{(1)}$ and E_d which satisfy Eq.(1.57). So the desorption peak shape may be generated from Eq.(1.56), using each pair of values which satisfy Eq.(1.57). By matching the theoretical peak to the experimental peak shape, it is possible to deduce the best values of $\nu_0^{(1)}$ and E_d that fit data.

1.5.3 Coverage measurement made during Programmed Desorption

Pfnur *et al*. **[8]** have used the vibrating capacitor method for measuring the instantaneous surface coverage of CO on Ru(001) during TPD. This method is based on the observation that the work function change $\Delta\phi$ was directly proportional to coverage of CO and independent on temperature.

Therefore,

$$\phi = \frac{d(\Delta\phi)}{dt} = k\frac{dN}{dt} \tag{1.58}$$

and it is possible to use Eq. (1.41) to determine $\nu_0^{(1)}$ and E_d as a function of coverage for the system plotting $\ln(\phi)/\phi$ versus 1/T for various constant coverages.

1.5.4 Leading Edge Analysis

This method **[1]** was introduced by Habenschaden and Kuppers and allows the determination of the activation parameters dependent on coverage and temperature. To keep temperature T and coverage Θ a small section of the spectrum on its leading edge is selected. This part of the spectrum is then plotted as ln r_{des} vs $1/T$, according to the logarithmic Polany-Wigner equation (1.15):

$$\ln r_{des} = -\frac{\Delta E_{des}}{RT} + \ln \nu_n + n \ln \Theta . \tag{1.59}$$

From the slope of this Arrhenius plot ΔE_{des} can be determined, while from the intercept the frequency factor ν_n can be determined if the reaction order and coverage are known.
Closer examination of the method reveals that an exact determination of ν_n is possible under certain condition. The first step is to differentiate Eq.(1.15) with respect to T for n=1 and T=$T_{\max}$, then taking account of the fact that the activation parameters are coverage dependent:

$$\left.\frac{d^2\Theta}{dt^2}\right|_{T_{\max}} = 0 , \tag{1.60}$$

so

$$\frac{d}{dt}\left[-\frac{\nu_1}{\beta}\exp\left(-\frac{\Delta E_{des}}{RT}\right)\Theta\right] = \left[-\frac{d\nu_1}{d\Theta}\frac{d\Theta}{dt}\cdot\Theta + \nu_1\frac{\Delta E_{des}}{RT^2}\cdot\Theta - \frac{\nu_1\Theta}{RT}\cdot\frac{d(\Delta E_{des})}{d\Theta}\cdot\frac{d\Theta}{dt} + \nu_1\frac{d\Theta}{dt}\right]. \tag{1.61}$$

Assuming n=1, using Eq.(1.47) and imposing condition described by Eq.(1.60) yields:

$$\left[\left(\frac{d\nu_1}{d\Theta}\cdot\Theta + \nu_1 - \frac{\nu_1\Theta}{RT}\cdot\frac{d(\Delta E_{des})}{d\Theta}\right)\cdot\left(\frac{1}{\beta}\cdot\exp\left(-\frac{\Delta E_{des}}{RT}\right)\right) - \frac{\Delta E_{des}}{RT^2}\right]_{T_{\max}} = 0 . \tag{1.62}$$

Then it is possible to separate all terms containing ν_1 :

$$\frac{\beta\cdot\Delta E_{des}}{RT^2}\cdot\exp\left(\frac{\Delta E_{des}}{RT}\right) = \nu_1 + \frac{d\nu_1}{d\Theta}\cdot\Theta - \frac{\nu_1\Theta}{RT}\cdot\frac{d(\Delta E_{des})}{d\Theta} . \tag{1.63}$$

The frequency factor ν_1 can be determined directly in two cases:

- when ΔE_{des} and ν_1 are independent of Θ so, from Eq.(1.63)

$$\nu_1 = \frac{\beta \cdot \Delta E_{des}}{RT^2} \cdot \exp\left(\frac{\Delta E_{des}}{RT}\right); \tag{1.64}$$

- when the last two terms on the right of Eq.(1.63) compensate each other, *i.e.* when

$$\frac{d\nu_1}{d\Theta} \cdot \Theta - \frac{\nu_1 \Theta}{RT} \cdot \frac{d\left(\Delta E_{des}\right)}{d\Theta} = 0 \tag{1.65}$$

In both cases ν_1 may be easily determined.

It is useful to note that Eq.(1.65) can be rearranged to

$$d\left(\ln \nu_1\right) = \frac{d\left(\Delta E_{des}\right)}{RT}\ , \tag{1.66}$$

which states that the logarithmic frequency factor scales linearly with the desorption energy. This result is an expression of the so-called *compensation effect*, that consists in the frequent observation that an increase in the exponential term in the Arrhenius equation is linked to a decrease of the frequency factor.

Chapter 2

Thermal Desorption Spectroscopy applications

Thermal desorption spectroscopy is useful to determinate kinetic and thermodynamic parameters of desorption processes and decomposition reactions. In this chapter the application of TDS to astrophysical processes is explained. We used this technique to investigate recombination and decomposition mechanisms occurred in ammonia and methane ices subjected to electron bombardment. We obtained that new species are produced when solid methane or solid ammonia are irradiated with electrons. In the first case we observed the production of acetylene (C_2H_2) and ethane (C_2H_6) while in the second case we detected diazene (N_2H_2).

2.1 Thermal desorption spectroscopy application to Astrophysics

2.1.1 The interstellar medium

The term "Interstellar Medium" (ISM) describes the matter diffused among the stars, that mostly thickens in wide regions named *interstellar clouds* (fig.2.1). In our galaxy, the *Via Lattea*, the interstellar clouds concentrate mainly along the spiral arms, but also in the regions between the spiral arms and the galactic halo, on and under the galactic plan.

The star light that crosses the interstellar medium is partially attenuated. This fact represented an important problem to the astronomers interested in the observation of stars and galaxies, until they understood the importance of studying the interstellar medium itself. The interstellar clouds, in fact, play an important role in the stars cycle of life: the explosions of supernovae enrich of heavier elements (synthesized into new stars) the interstellar clouds, which contribute to the rising of new stars because of gravitational collapse.

The interstellar medium represents the 10-15% of our galaxy mass and it is made largely of gas (99%) and for a small part (1%) of dust grains with dimensions in the order of micron. The dust grains are mainly the cause of the stellar extinction phenomenon, consisting in the partial stellar light attenuation due to the scattering and the adsorption physical processes. The

interstellar clouds are composed by gases and dusts and their interaction produces a rich interstellar chemistry.

Fig. 2.1. The Horse's head nebula belongs to the molecular Orione's cloud. The nebula is made of dusts that block the light of the incandescent gas on background.

2.1.2 The interstellar gas

The interstellar matter chemical composition is similar to the cosmic composition, describing the abundance of several elements of our Sun. Thus the interstellar gas is made mainly of hydrogen (90%) and helium (10%), while oxygen, carbon and nitrogen represent only the 0.1% of the entire mass; other heavier elements are present in very small amounts. The physical and chemical properties of interstellar clouds are mainly determined by interstellar gas because of its great abundance contrarily to dusts. Furthermore the interstellar clouds are classified according to hydrogen state. Many chemical species have been identified by the adsorption spectra of the stellar light that arrives on hearth passing through an interstellar cloud (Fig.2.2).

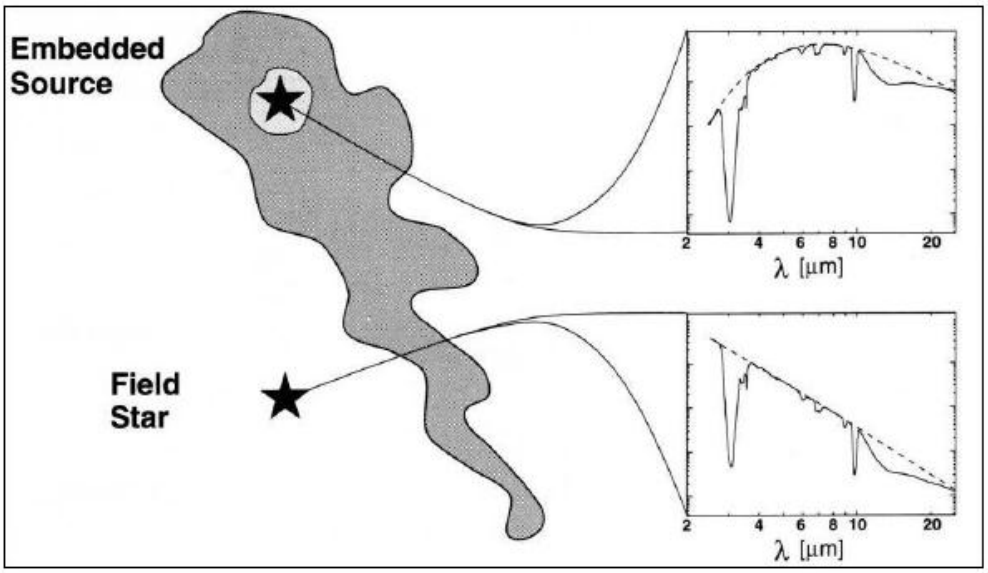

Fig. 2.2. The interaction between the interstellar light and the interstellar medium, placed along the observation direction, gives information about the chemical elements constituting the interstellar clouds.

The information about interstellar gas mostly come from radio observations. At the beginning of 1950 Purcell and his collaborators pointed out the line of 21cm of interstellar atomic hydrogen. Consequently to this observation the analysis of the 21cm line became a powerful instrument for the interstellar gas investigation; this technique gives information only about atomic hydrogen. Although the molecular hydrogen is the most abundant molecule in nature, its individuation is very difficult; in fact H_2 is a diatomic homo-nuclear molecule with no permanent electric dipole, so it can emit radiation only through quadrupole transitions. For this cause the abundance of H_2 in the interstellar medium is indirectly estimated by the observation of other molecules as CO, that is the second more abundant species (about 10^{-4}-10^{-5} of hydrogen concentration).

When a CO molecule collides with a H_2 molecule (which is the most probable partner in collisions because of its abundance) the former may be excited in a higher roto-vibrational state; the consequent CO de-excitation through a photon emission gives information about the presence of H_2. The ratio of H_2 molecular abundance with H_2 atomic abundance varies with the position of our Galaxy. Near the Sun the gas density is about 0.04 solar mass per $(\text{parsec})^3$, where a solar mass is equal to 1.99×10^{30} kg and 1 parsec=$3.0.86\times10^{16}$ m; the entire mass is made of hydrogen for 77%, molecules for 17% and ions for 6%.

The interstellar medium regions which are better screened from the stellar radiations are characterized by a great presence of H_2, while regions with high radiation fields are dominated by the H presence.

Although H_2 is the simpler molecule, its formation in the interstellar medium has generated many discussions. In fact the radioactive association of two hydrogen atoms is a less efficient process of formation because it involves prohibited roto-vibrational transitions; moreover the reaction of three bodies in gaseous phase in the interstellar medium is rare.
Hollenbach and Salpeter suggested that H_2 formation may occur efficaciously on the dust grains surface, which may operate as catalysts **[9]**. Many other studies both theoretical **[10,11]** and experimental **[12, 13, 14]** have been analyzed this topic.

2.1.3 The interstellar dust

Although the dust grains represent only the 1% of the interstellar medium mass, they play a fundamental role in the chemistry and evolution of the interstellar clouds. In fact they operate as catalysts permitting to the chemical species adsorbed on their surface to interact and to form new species. The formation of new species on the grain surface can be described according to the following steps: 1) arrival of species in gaseous phase which are adsorbed on the grain surface; 2) scansion of the grain surface by species with more mobility; 3) meeting and chemical reaction between two chemical species on grain surface; 4) release of exceeding energy by the new species created and consequent molecular stabilization (as in the case of H_2); 5) probable desorption of the new species formed (fig. 2.3).

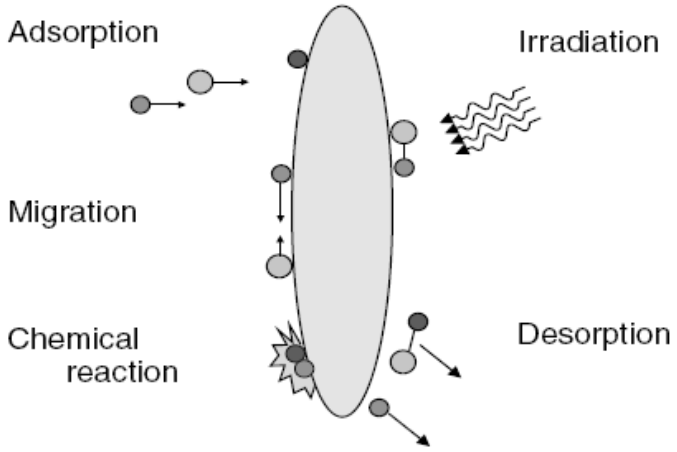

Fig.2.3. Schematic illustration of interactions on grains surface.

The presence of dust grains into interstellar medium is confirmed by some evidences, among which the stellar light extinction curve at wavelengths of visible and ultraviolet (fig. 2.4). The stellar light extinction is due to scattering and adsorption processes involving the dust grains. The extinction is a function of wavelength; a wavelength decrease corresponds to an extinction increase. As a consequence of this observation the stellar light is more red than it is in reality. Another evidence of the interstellar dust grains existence is the weak linear polarization of stellar light; this implies also that the grains cannot have a spherical shape. The dust grains in fact are elongated particles made of paramagnetic materials and so aligned to interstellar magnetic fields.

Although the evidence of these observations, the dust grains models (for example utilized for understanding the interstellar extinction curve) often consider a spherical shape for the grains. The typical dimensions of the dust grains are in the range of 1nm-3μm.

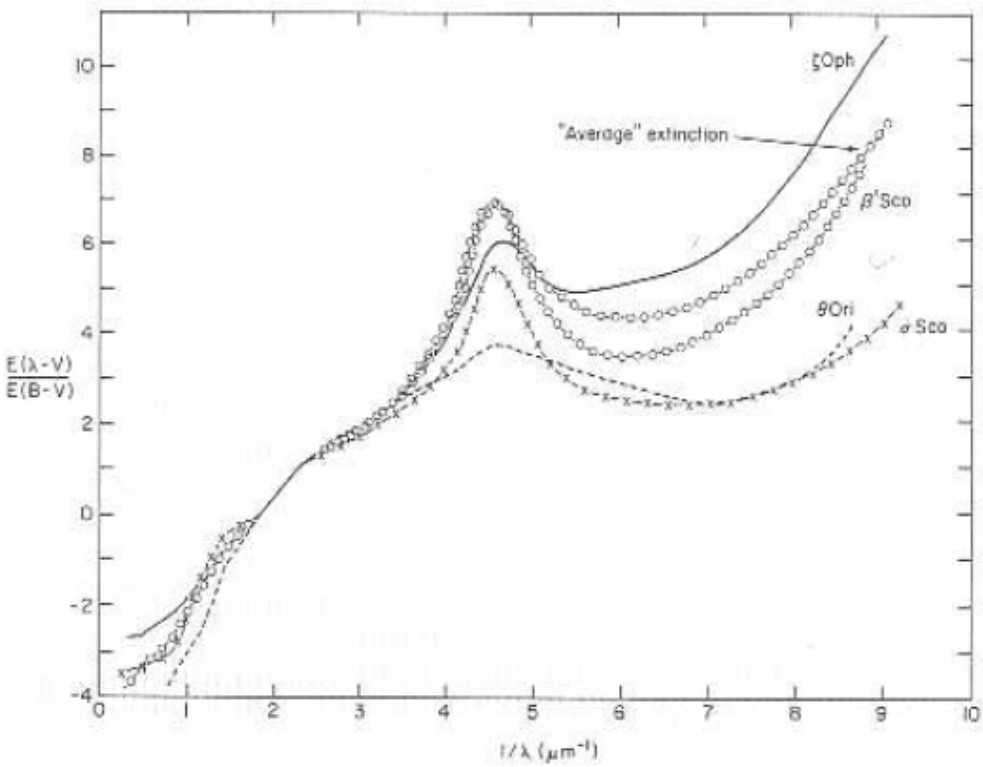

Fig. 2.4. Stellar extinction curve for several stars plotted as function of 1/λ

The analysis of adsorption spectra in the infrared (for example spectra acquired by the satellite ISO) shows that the dust grains are mainly made of silicates and carbon materials. The spectral characteristics at 10 μm and 12 μm are due to vibrational transitions of silicates

(SiO e SiO_2) and water ice, while the interstellar extinction in ultraviolet may be explained by the presence of small graphitic grains. Another observation about the grains chemical composition is that some elements as N and S in gaseous phase have abundances similar to solar ones, while several elements (as Mg, Al, Si, Ti, Ca, Fe, Ni, Cr) are less abundant (figure 2.5). It is note that the interstellar abundances are similar to solar ones **[15]**, so the elements which are absent in gaseous phase are probably located in the dust grains **[16]**.

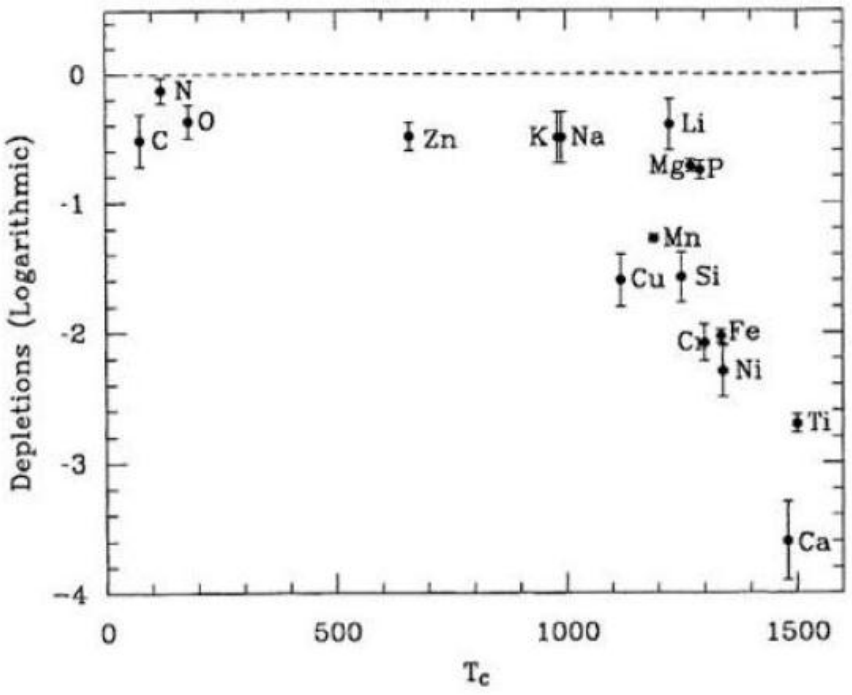

Fig. 2.5. Reduction of elements (respect to cosmic abundances) in the interstellar cloud ζ Oph as a function of the condensation temperature of the elements. The ordinate is represented by the difference between the logarithm of measured abundances and the logarithm of cosmic abundances. For $T_c \geq 1200$ K the elements are able to form refractory solids. For example Ca has an abundance 10^4 lower then solar one.

It is thought that the dust grains are ejected by hot stars; in fact the dust grains cannot form in situ in interstellar cloud because of its very low density. So the dust grains formation mechanism is very probably the following. At the end of their life, the so-called Asymptotic Giant Branch stars (AGB) emit a large part of their envelope into space, so they are surrounded by very large atmospheres which are sufficiently cold and dense to permit atoms and molecules nucleation leading to the formation of small solid particles. The flow of stellar

materials may contain mainly carbon or oxygen, characterizing the composition of the dust produced: if carbon is more abundant then oxygen, the latter forms mainly CO and the former produces several carbon molecules, so dust grains contain carbon; if oxygen is more abundant, the oxygen excess produces metallic oxides which for nucleation permit the formation of solid oxides and silicates **[17]**.

2.1.4 Ices in interstellar medium

In the very dense and cold interstellar clouds (the minimum density is about 10^4 atoms for cubic centimetre) the observations have revealed the existence of frozen mantles on the dust grains surface **[18]**. These ices are mainly made of water, identified by the features at 6.0 μm and 3.1 μm, respectively assigned to the bending mode of the amorphous water ice and to the stretching mode of O-H in the water ice. Other molecules which contribute to formation of the grains ice mantel are CO, CO_2, CH_3OH, CH_4, NH_3, OCS (see table1 and figure 2.6).

Molecule	Abundance(%)	Molecule	Abundance(%)
H_2O	100	CO	3-50
CO_2	7-25	NH_3	< 10
CH_3OH	2-25	CH_4	0.9-1.9
H_2CO	3-7	OCS	0.1
C_2H_6	≤ 0.4	OCN^-	≤ 1.9
NH_4^+	3-17	$HCOOH$	≤ 1.7

Table 2.1. Molecules observed in the interstellar ices, with abundances relative to water ice.

In general these molecules condense on grains in gaseous phase, but the grains mantle composition does not exactly reflect the composition and the abundances of the gaseous phase. For example it is known that CO_2 is present in the grains, but it is not observed in gaseous phase yet **[19]**.

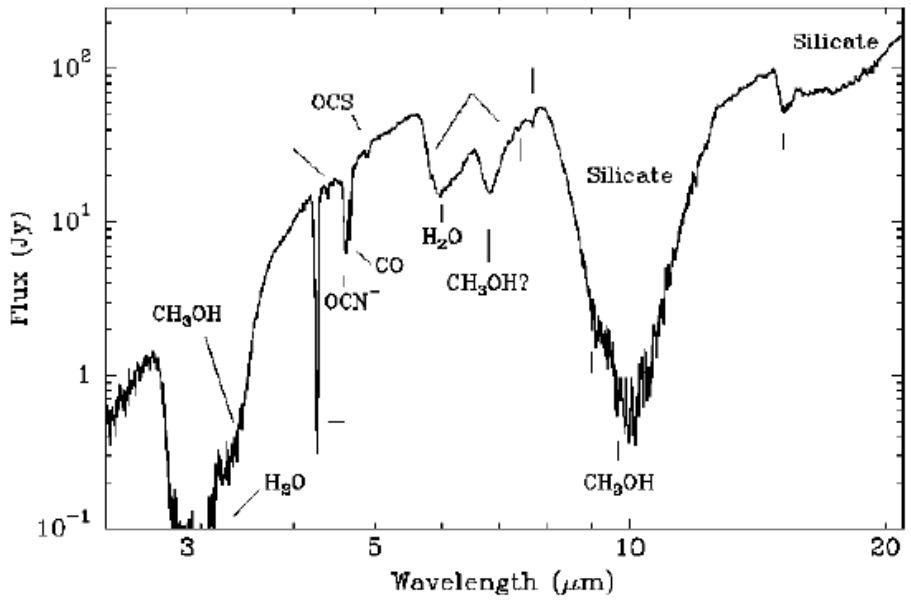

Fig. 2.6. Inventory of interstellar ices pointed out in the protostar W33A (Gibb et al., 2000). The spectra shows the adsorption characteristics due both to the dust grains (silicates) and to the dirty ice mantles.

So it is reasonable to think that when reactive chemical species condense on the dust grains may form new molecules through chemical reaction. New molecules form also after irradiation by UV photons and cosmic rays at which the interstellar ices are subjected, as noticed through experiments conducted in laboratories (see **[20]** for the ion bombardment and **[21]** for the photons irradiation) . Also the water ice forms by chemical reaction on the dust grains surface. Instead the direct increase of complex molecules from gaseous phase influences little the chemical composition of the mantles. However mantles composition mainly reflects the local conditions (figure 2.7). Because hydrogen is the more abundant species in the Universe the chemistry on the grains surface is determined by the ratio H/H_2. When this ratio is high the chemistry is dominated by hydrogenation reactions and the more abundant chemical species are H_2O, NH_3 and CH_4. Instead if the ratio H/H_2 is lower then 1, some very reactive species as O and N may react between them and they may form CO, CO_2, O_2 and N_2. Consequently it is expected that two different mantle types are produced by reactions on the grains surfaces: the first type is dominated by polar molecules linked by hydrogen bond, while the second one is dominated by unsaturated non-polar molecules (or weakly polar) **[22]**. In fact, from the analysis of carbon monoxide profiles in solid phase, generated by young stellar objects, it is possible to observe two types of ice mixtures (polar

and non-polar) and a third type whose nature is uncertain. The profile attributed to CO stretching (2140 cm^{-1}) is formed by the superimposition of three components, describing three different ice mixtures. In general, a component prevails over the two others according to the physical condition of each interstellar cloud **[23]**.

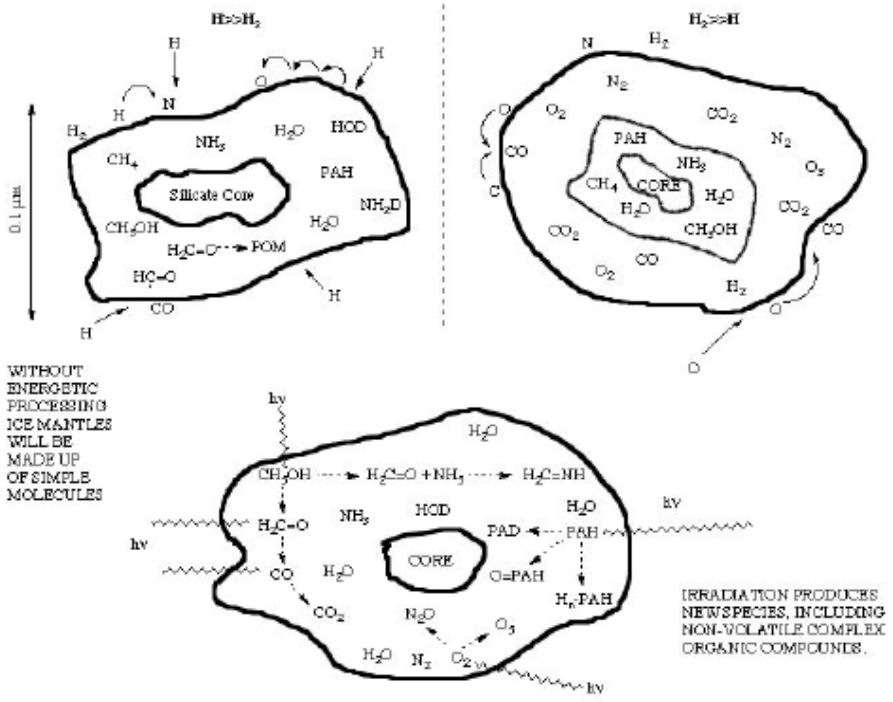

Fig. 2.7. Schematic representation of the different mantle types. The interstellar ice composition in interstellar clouds depends on local conditions as the ratio H/H_2 , the intensity of cosmic rays and the radiation field.

The main constituent of ice mantles is water, whose chemical origin is not jet understood. Some theoretical works **[24, 25]** suggest three possible reactions for the formation of H_2O: hydrogenation of O, O_2 and O_3. Actually, because of the few experiments simulating these reactions, it is not possible to determinate all their contributes. However the water formation in gaseous phase and its consequent increase on grains does not explain the H_2O abundances observed **[26]**. Both experimental **[27]** and theoretical **[28]** evidences confirm that the water ice in the interstellar medium is mainly amorphous, but there are few indications about its morphology. Some experiments have showed that the ice porosity considerably influences the H_2 formation efficiency **[29]** and the H_2 energetic content when, after its formation, it is released by grain in gaseous phase **[30]**. Moreover it is observed that a porous ice film has an adsorption efficiency 20-50 times larger then a compact ice film **[31]**.

The ice porosity may be identified by the weak adsorption features in the infrared (~ 2.7 μm) due to vibration of the O-H dangling bond on the pore surface **[32]**. This feature is not ~~jet~~ observed yet for the interstellar ices, so it is reasonable to think that they have a compact nature **[33]**.

2.1.5 Ices and energetic agents

When inside an interstellar cloud bright stars form, they may induce both physical and chemical changes into surrounding material irradiating energy into their local environment. In particular the frozen mantles of the dust grains may be heated producing (partially or totally) the ices sublimation or crystallization. Moreover the mantles composition may be modified through chemical reactions inducted by the radiation field. The ices spectroscopy gives three methods to analyze these changes: 1) the abundance variations of the more volatile species, attributable to sublimation; 2) the profile evolution as function of temperature; 3) the individuation of features connected to photo-processes products. Figure 3.8 shows schematically the sublimation zones around a young stellar object (YSO). Among the molecules commonly observed in the ice mantles, CO is the most volatile, H_2O is the least volatile and CO_2 represents an intermediate case.

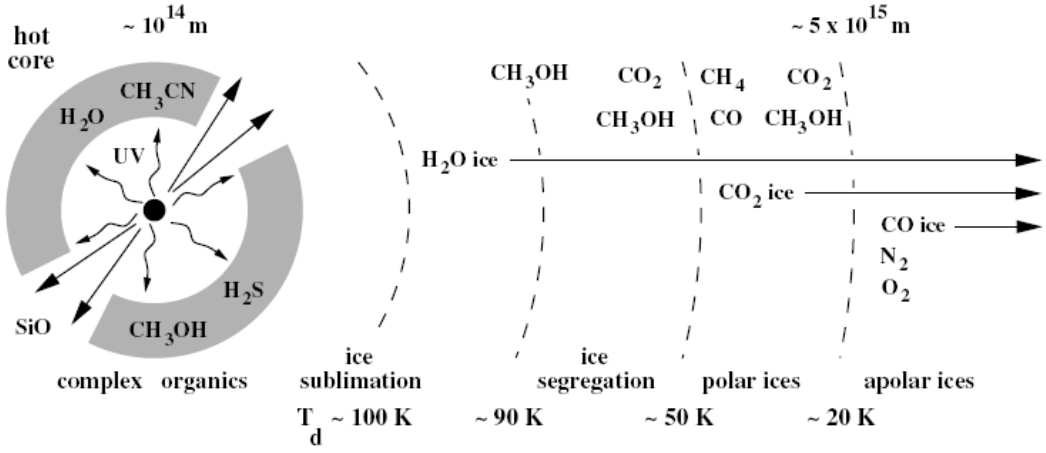

Fig. 2.8. Schematic representation of chemical environment of a massive young star inside a dense molecular cloud. The presence of several molecules into mantles is indicated, respect to the grains temperature (T_d) and as a function of the star radial distance.

So the heating may remove the non-polar layer (dominated by CO) faster then the polar layer (dominated by H_2O); particularly the non-polar ice may vaporize at about 20 K, while the

polar one may survive at least until 100 K. This assumption is confirmed by observations. Analyzing the differences in mantles sublimations observed along several observation lines, Chiar et al. proposed the existence of three general classes of objects, subdivided in accordance with an evolutionary sequence: 1) objects with few or with no sublimation of non-polar mantles, with a ratio of the two ice type CO/H_2O about (25-60)%; 2) objects subjected to a moderate or high sublimation of non-polar mantles, with a ratio CO/H_2O about (1-20)%; 3) objects characterized by a total CO sublimation.

As already written, at the beginning of their formation the ices are amorphous, because accretion happens at temperature very lower then fusion or sublimation ones of remarkable molecules.

The spectral profiles of amorphous solids are very large Gaussians. If material is heated the spectral lines become narrower and more similar to the crystalline solids spectral profiles, because of molecules rearrangement in energetically more favourable configurations. Through these differences it has been possible to verify that in the so-called quiescent dark clouds the ices are at a temperature between 10 K and 20 K, while in many YSO the ices are at a temperature in the range of (70-100)K **[27]**. It is important to note that although is favourable to characterize ices in accordance with distinct polar and non-polar components (deposited sequentially), it is possible to observe an intermediate stadium of mantle growth in which H_2O and CO accumulate in comparable rates.

Oxidation and hydrogenation reactions, involving CO, may lead to CO_2 and CH_3OH production and so to formation of an amorphous mixture containing CO_2, CH_3OH e H_2O with similar proportions.

If this mixture is heated, the consequent structural changes lead to the formation of complexes in which the oxygen atoms of CH_3OH bond with the carbon atoms of CO_2 creating strong intermolecular bonds.

The ices thermal evolution is mainly determined by the adsorption of infrared radiation emitted from stars inside gas and dusts entanglement. When the circumstellar material gradually disperses, more energetic radiation and particles flow may permeate the surrounding medium. Photons with energies in the order of eV may break the chemical bonds and they may convert saturated molecules as H_2O, NH_3 e CH_4 in radicals. If irradiation is followed by heating, the radicals may migrate through the mantles and they may react with other chemical species. Moreover when the grains come back from the molecular clouds to the diffuse interstellar medium, they maintain their mantles which are consequently and

remarkably modified by photochemical reactions; these reactions convert the volatile ices in refractory organic material, as pointed out in laboratory simulations (see **[34]**, **[35]** and **[36]**). Into dense molecular clouds the grains mantles are also subjected to ion bombardment. Comparing the adsorption spectra obtained by observations with the spectra of ices bombarded in laboratory, it is possible to obtain information about the ion bombardment effects to which are subjected the interstellar ices. For example figure 2.9 (**[20]**) shows a comparison between the band profile at 2165 cm^{-1} observed in the direction of the protostellar object W33A and the band formed after ion bombardment of an ices mixture containing H_2O, CH_4 e N_2. The good comparison confirms the hypothesis that the energetic agents play an important role in the grains mantels evolution and that their chemical composition may be strongly influenced by interaction with cosmic rays **[20]**.

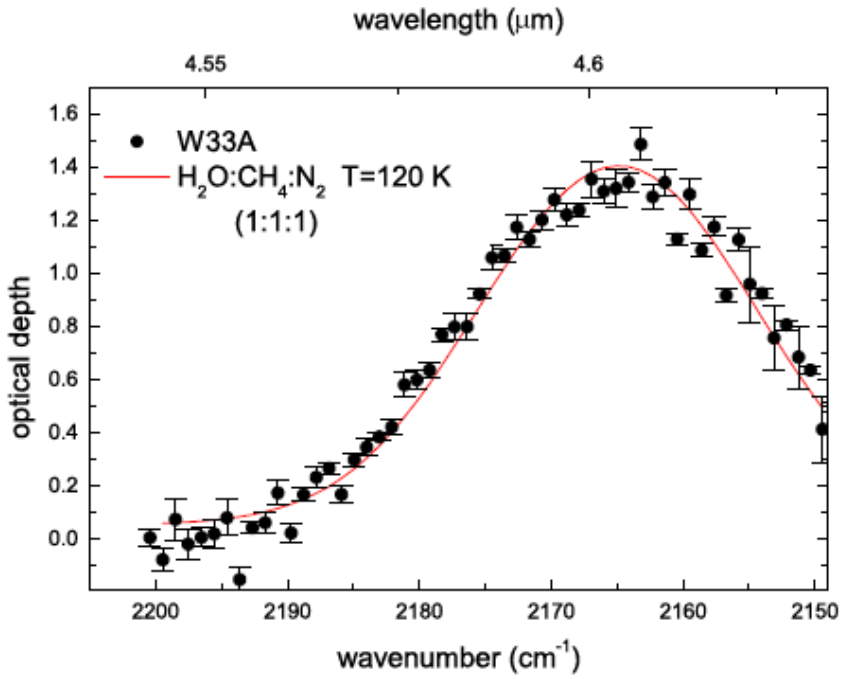

Fig.2.9. Comparison between the band profile at a 2165 cm^{-1} observed in the direction of W33A and the spectra obtained in laboratory from a mixture of H_2O:CH_4:N_2 bombarded at 12 K and heated up to 120 K (**[20]**).

The electronic bombardment effect on interstellar ices with laboratory experiments has been recently investigated **[37]**.

Solid ammonia (NH_3) was irradiated in the temperature range of (10-60) K with high-energy electrons to simulate the processing of ammonia-bearing ices in the interstellar medium and in the solar system.

Ammonia and ammonia hydrate have been found in the atmosphere of Jupiter, Saturn, Uranus and on the surfaces of their icy satellites such as Miranda, Mimas, Enceladus, Tethys and Rhea. Ammonia has been identified in the dust grains in cold molecular clouds with an abundance of 1%-10% with respect to water. The ammonia abundance in the ices of comets and protostars is lower than water (H_2O), carbon monoxide (CO) and carbon dioxide (CO_2), but higher than methane (CH_4). The ices in these cold molecular clouds and on solar system bodies are subjected to the irradiation by cosmic-rays, UV photons, the solar wind or by energetic particles trapped in planetary magnetospheres.

Ammonia is hardly a pure ice, but mixed with species such as water, so it is essential to study the mixture of ammonia with several molecules under realistic conditions. The solid ammonia properties are very interesting from both astrophysical and chemical viewpoint.

As a result of the experiments of Zheng et al. the synthesis of hydrazine (N_2H_4), diazene (N_2H_2 isomers), hydrogen azide (HN_3), the amino radical (NH_2), molecular hydrogen (H_2), and molecular nitrogen (N_2) has been confirmed. So ammonia may be the main source of nitrogen in comets and the interaction of ammonia with ionizing radiation can produce a greater amount of molecular nitrogen. As consequence it is expected , on various solar system objects, an ammonia decreasing corresponding to an increasing of molecular nitrogen fraction.

The results show that the production rates of hydrazine, diazene, hydrogen azide, molecular hydrogen, and molecular nitrogen are higher in amorphous ammonia than those in crystalline ammonia; this behaviour is similar to the production of molecular hydrogen, molecular oxygen, and hydrogen peroxide found in electron-irradiated water ices.

These studies have been analyzed also in this work and they will be described particularly in chapter 4.

2.2 Thermal desorption spectroscopy application to Geophysics

In Geophysics and Petrology Thermal Desorption Spectroscopy can be used to study minerals chemical composition. Our interest was focused on zoisite. In fact, in this work we used TPD to investigate zoisite behaviour and to understand if its modification into tanzanite variety after heating is due to structural changes or to a dehydration mechanism.

2.2.1 Zoisite

Zoisite ($Ca_2Al_3[Si_2O_7][SiO_4]O(OH)$) is a sorosilicate, i.e. a silicate in which are present isolate groups made of tetrahedral couples (SiO4) sharing an apical oxygen. The zoisite empirical formula is $Ca_2Al_3Si_3O_{12}(OH)$.

The crystal structure consists of one type of endless octahedral chains parallel to *b* with two distinct octahedral sites M1,2 and M3. These chains are cross by isolated tetrahedral SiO_4 (T3) and Si_2O_7 groups (T1 and T2) in the *a* and *c* directions(fig.3.10).

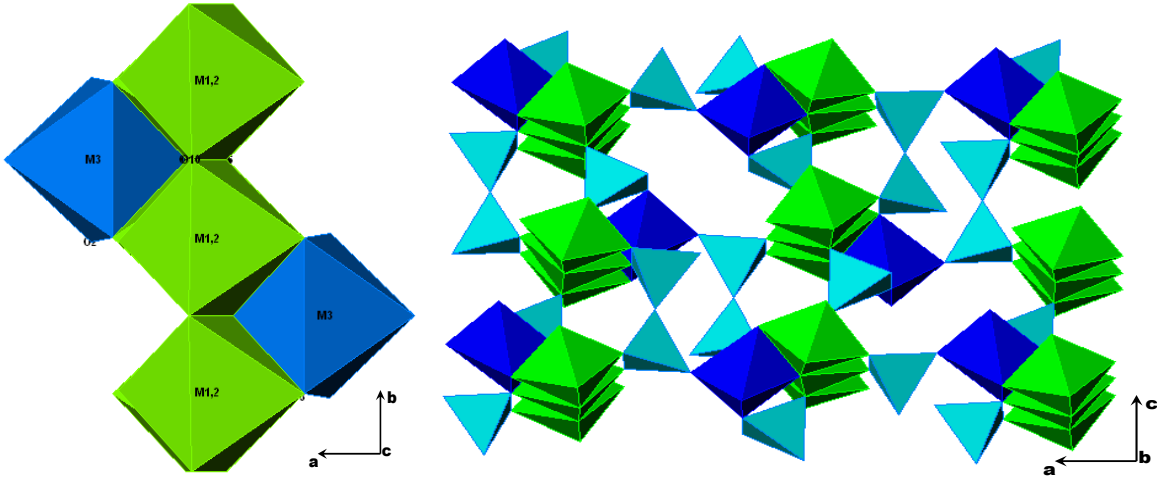

Fig.2.10. The elementary crystal structure of zoisite.

Zoisite is an allocromatic mineral, because its milling produces a white dust. So the colour is not due to its chemical composition, but it can vary because of the presence of cromophores ions or structural defects of crystal lattice.

Zoisite chemical composition (in %) is mainly described in the following table **[38]**:

Calcium (Ca)	17.64%	CaO	24.68
Aluminum (Al)	17.82%	Al_2O_3	33.66
Silicon (Si)	18.52%	SiO_2	39.67
Hydrogen (H)	0.22%	H_2O	1.98
Oxygen (O)	45.78%		

Table 2.2

Among the typical impurities of zoisite the most common is water.

The optical adsoprtion spectra of natural yellow zoisite shows three spectral bands, respectively at 13.400 cm^{-1}, 22.500 cm^{-1} and 27.000 cm^{-1}.

Tanzanite is the blue variety of zoisite, which was discovered in the Merelani Hills of Northern Tanzania in 1967. When yellow zoisite is heated between 370°C-650°C, it becomes an intense violet-blue colour (variety tanzanite) **[39]**; this behaviour was explained in terms of change of the oxidation state of transition metal ions, such as V **[40, 41]**.

Rodeghero et al. **[42]** studied the dependence of the colour changes in yellow and blue zoisite after heating not only on the concentration of metal ions and their oxidation states, but also on possible changes in bond lengths and bond angles or on distortion of coordination polyhedron.

Yellow and blue crystal of zoisite were characterized by XRF analysis, that reveal that the same minor elements (particularly V and Sr) are present in both samples but in different amounts; this aspect can play a fundamental role in the change colour.

The samples were heated in air flux from room temperature to 520°C (heating rate 5°C/min). PXRD data were collected on a diffractometer before and after heating; XRD diffraction patterns were analysed by the Rietveld method. Finally, the samples were optically characterized by UV-VIS technique, using a Xenon lamp and an integrating sphere.

UV-VIS spectra show that yellow zoisite becomes blue during heating both in air and nitrogen. The spectral changes induced by heating indicates that the colour change is connected the disappearance of the 22500 cm^{-1} band (fig.3.11).

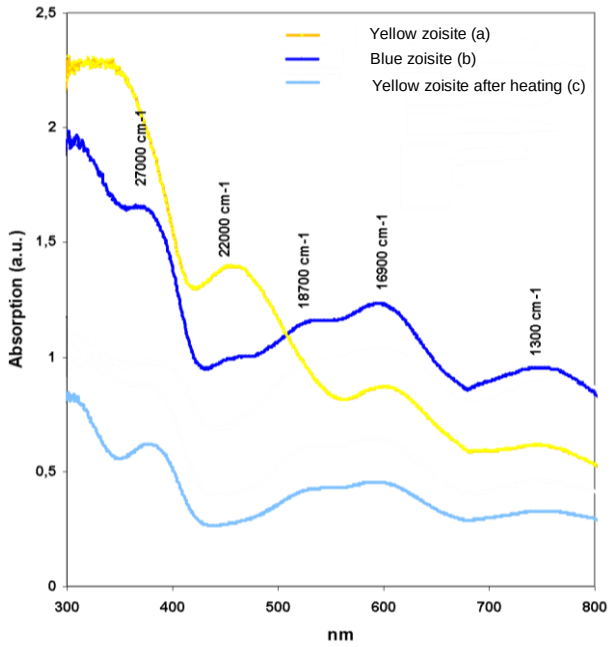

Fig.2.11. UV-VIS spectra for (a) yellow zoisite, (b) blue zosite and (c) yellow zoisite after heating.

Differences in the spectrum between the originally blue-coloured zoisite and the heat-treated zoisite could be explained on the basis of the structural refinements.

The analysis of PXRD patterns shows, for structural refinement of natural yellow (a) and blue (b) samples at room temperature, differences in the unit cell parameters and also in the orientation and dimension of coordination polyhedron. In both samples, M3 polyhedron is larger than M1 one (fig. 2.12). After heating, structural refinement of yellow and blue samples reveals that the orientation and dimension of coordination polyhedron becomes similar. The rotation of M3 parallel to *a* is compensated by a rotation of the Si_2O_7 group, which is reflected by the shortening of the O_7-O_8 distance and the narrowing of T1-O9-T2 angle.

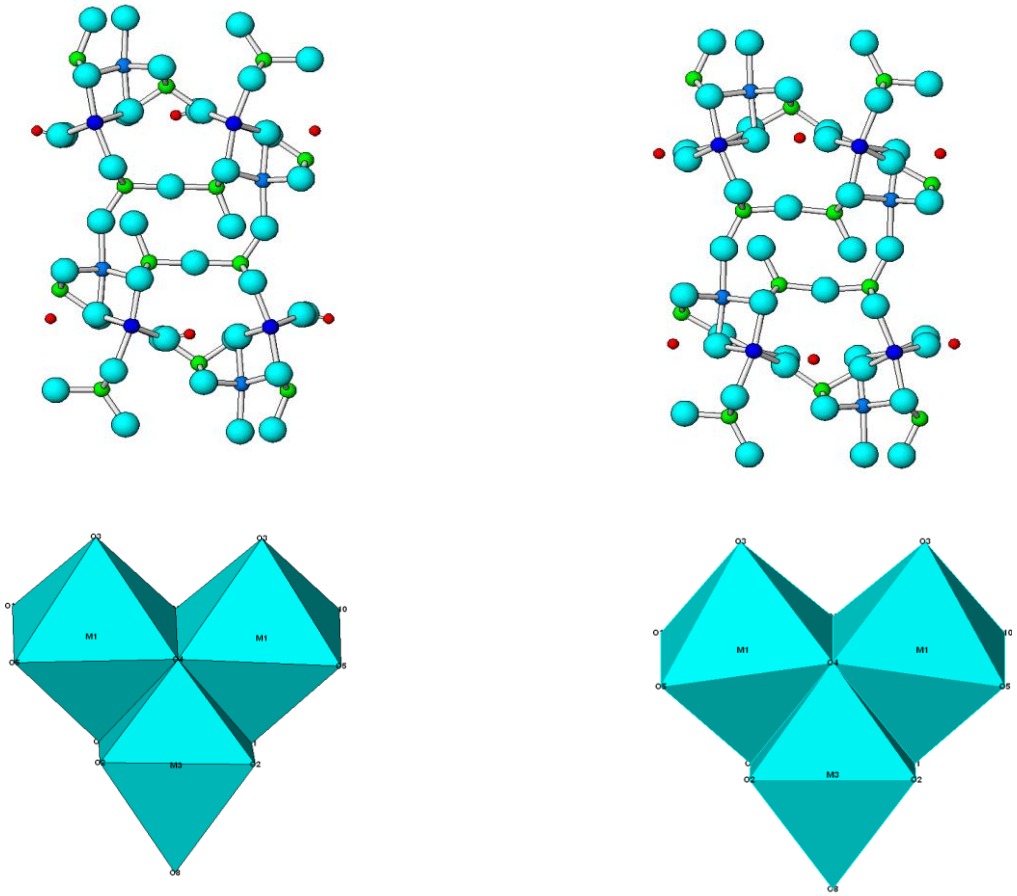

Fig. 2.12. Structural refinement of natural yellow (a) and blue (b) zoisite at room temperature

The essential elements of zoisite ($Ca_2Al_3[Si_2O_7][SiO_4]O(OH)$) are Al, Ca, H, O, Si, but water is a common impurity. When zoisite is heated its structure is subject to a change and it is important to verify if the structural change is due to the loss of an essential element as H or to a H_2O release. In the following chapter, a TPD experiment on zoisite heating from room temperature to 650°C is analysed to evaluate a possible H_2O release and to explain changes in structure.

In fact, the products of zoisite heating are H, O, OH and H_2O; by analysing thermal desorption spectra for these species it is clear that intensity and shape are the same for all elements. So it is reasonable to think that H, O, OH are due to cracking fraction of water (released by zoisite during heating) operated by quadrupole filament. So the main mechanism of zoisite change in colour after heating is the dehydration.

2.3 Thermal desorption spectroscopy application to high-energies Physics

In this work we use Thermal Desorption Spectroscopy to evaluate molecular hydrogen adsorption properties of carbon nanotubes to find a possible solution for vacuum system problems in future accelerators. In fact molecular hydrogen represents the critical species for desorption in Large Hadron Collider. We verified that carbon nanotubes have a great H_2 adsorption capacity also at very low temperatures (12K-20K) so they may be good candidates to criosorbers in the future accelerators.

2.3.1 Large Hadron Collider: problems to vacuum system

The Large Hadron Collider (LHC) is made of a couple of two semi-conducting rings with a circumference about 26.7 Km; inside these rings two protons beams with energy of 7 TeV circulate **[43]-[46]**.

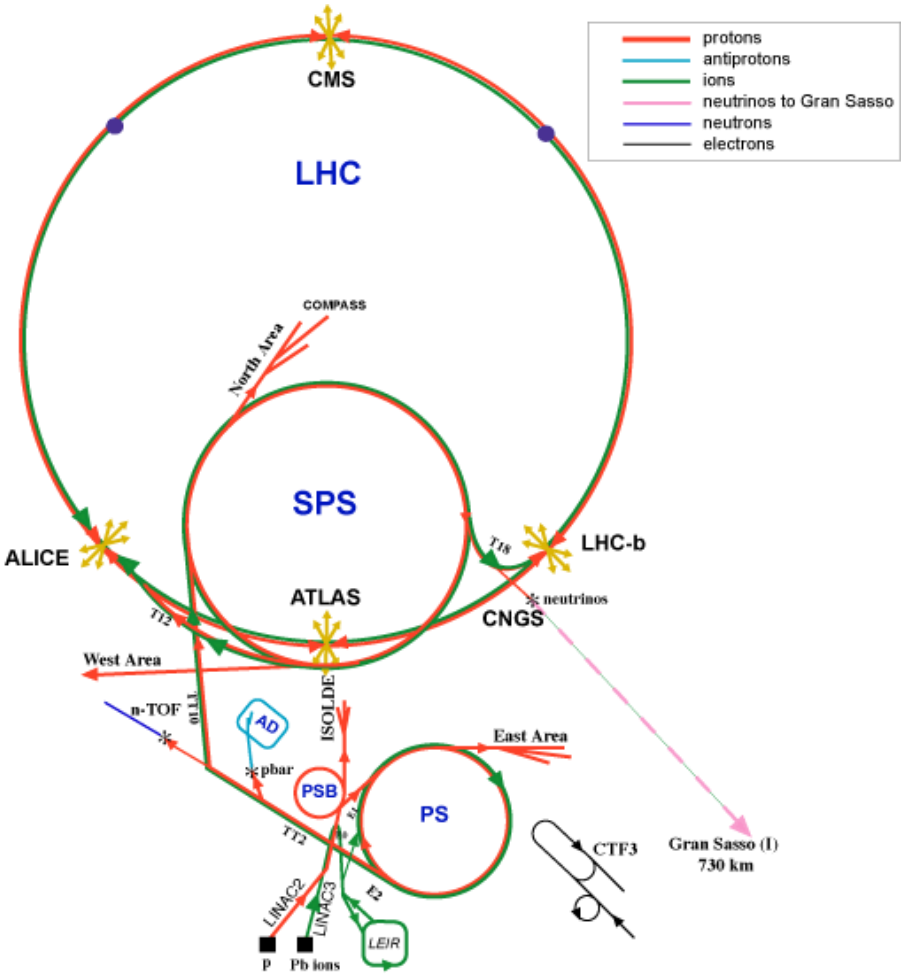

2.13. Schematic representation of LHC

There are also two magnets in a direct contact with liquid helium at 1.9 K. The inner walls of semi-conducting magnets ("cold bore") work at very low temperatures and they are efficient cryo-pumps. The core of these magnets is made of super-conducting cables, wrapped in coils, which generate a magnetic field at current passage. A couple of coils (super-conducting dipole) provides the magnetic field necessary to bend the beams forcing them on a circular trajectory. So is produced an intense centripetal acceleration.

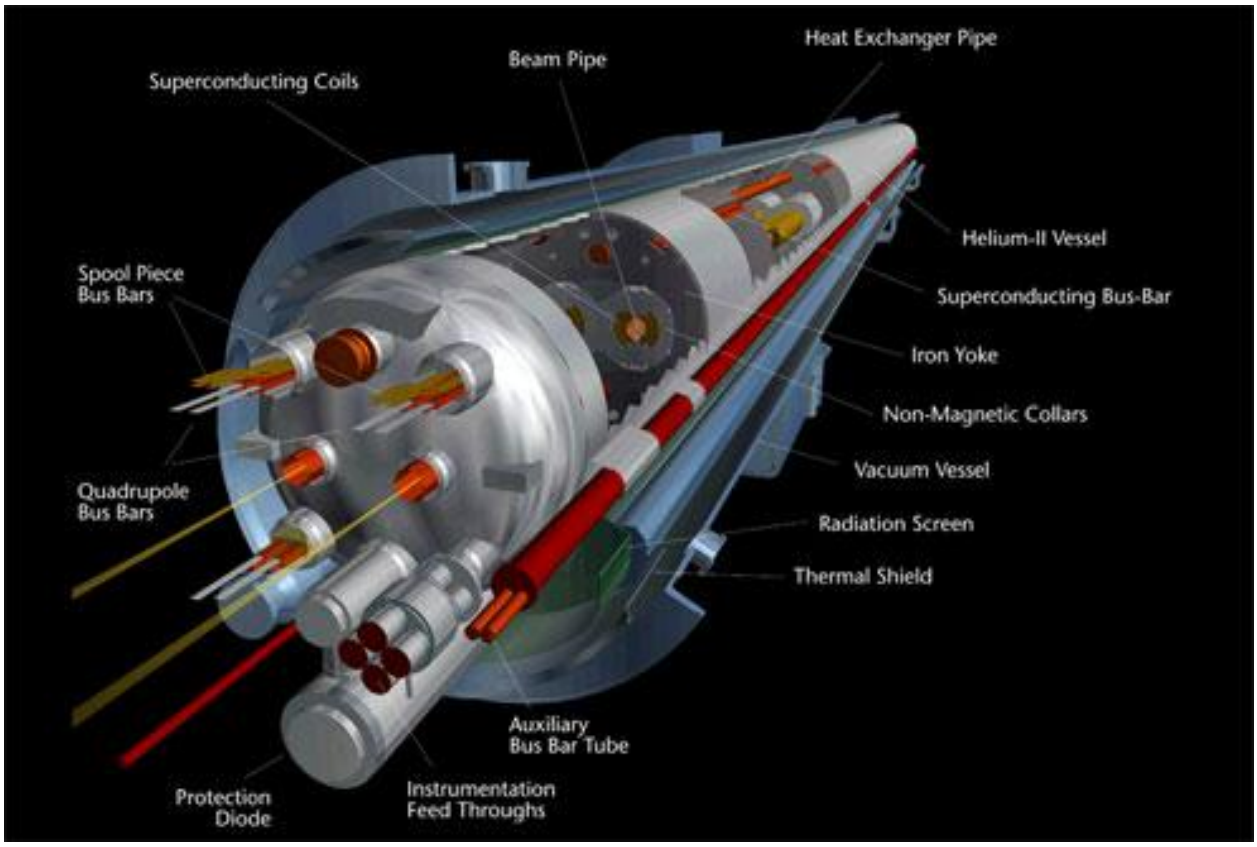

2.14. LHC section

As consequence, inside the magnetic rings every beam emits a synchrotron radiation with a flow of about 10^7 photons $s^{-1}m^{-1}$, a critical energy of 45.4 eV and a power of 0.22 Wm^{-1}. The radiation emitted by relativistic protons deteriorates the vacuum system; in fact, because of photons scattering with residual gas, the desorption of gas and electrons from the ring walls is produced **[47].**

It is important to take into account the possibility that desorbed particles settle on super-conducting magnetic coils, stopping the machine operations. To avoid a decrease of cryogenic power, the heat load (due to synchrotron radiation) and the dissipation of resistive power (due to beam currents) must be adsorbed on a *beam screen*, inserting inside the vacuum chamber and operating at temperature between 5 K and 20 K (fig.2.15).

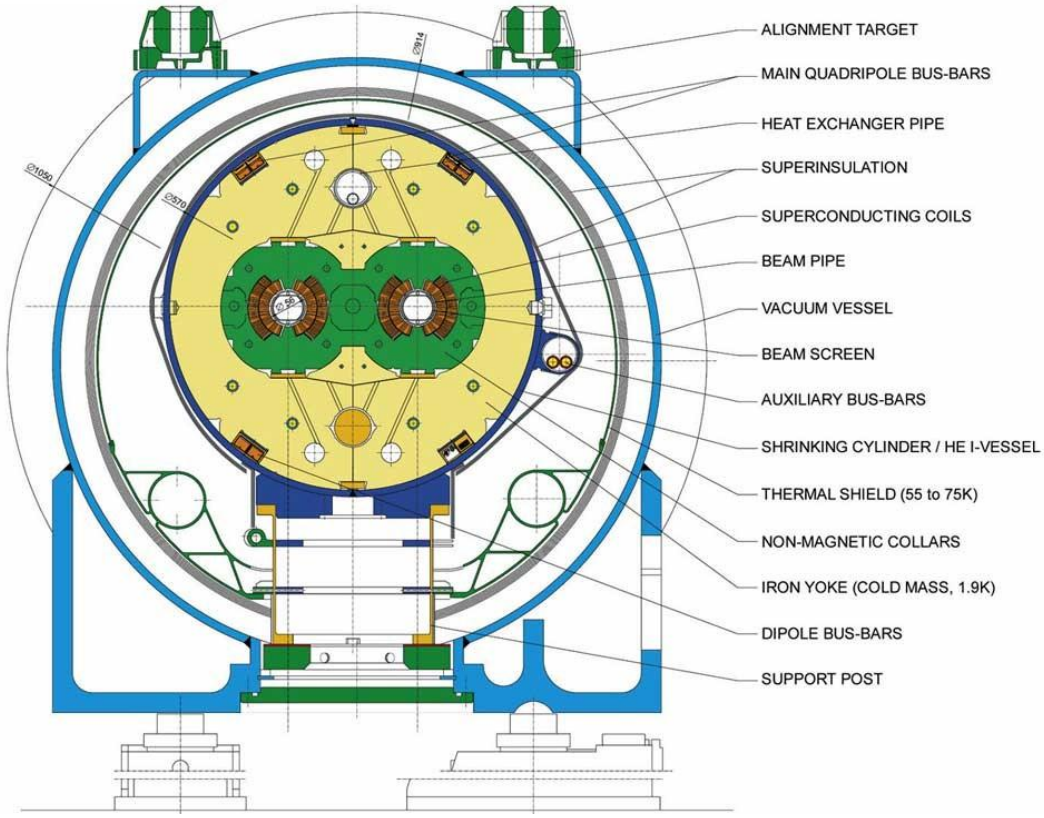

2.15. Schematically representation of LHC section

The cryo-pumping on cold surfaces gives a good vacuum in chamber, but it is important to guarantee that the vapour pressure of cryo-adsorbed molecules (whose critical species are H_2 and He) remains in acceptable limits. This is a serious problem because it may compromise the LHC functioning.

The possibility to use Carbon Nanotubes as cryo-pumps to solve vacuum system problems in LHC and their adsorption power are analysed in detail in the following chapter. In fact using CNTs to cover the vacuum chamber walls it may promote the adsorption of residual gases (particularly for H_2 **[58])** at temperatures on the range of (5÷20)K.

2.3.2 The LHC vacuum system

The LHC vacuum system is made of two parts, according to the different vacuum conditions at which the apparatus is subjected:

- the cryogenic insulation vacuum, which required pressures in the order of 10^{-6} mbar;
- the dynamic vacuum, necessary to guarantee a good beam lifetime; pressures required are about 10^{-10} mbar.

The dynamic vacuum is a specific vacuum for the beam.
The "beam pipe" is localized in the centre of super-conducting magnetic coil (figure 3.15) and it is in direct contact with helium at 1.9K("cold bore beam pipe").
At these temperatures the vacuum chamber walls become an efficient cryo-pump with an infinite adsorption power, with the exception of helium and hydrogen.
It is possible to individuate four distinct heat sources inside the system, whose temperature is maintained at 1.9K (fig.2.16):

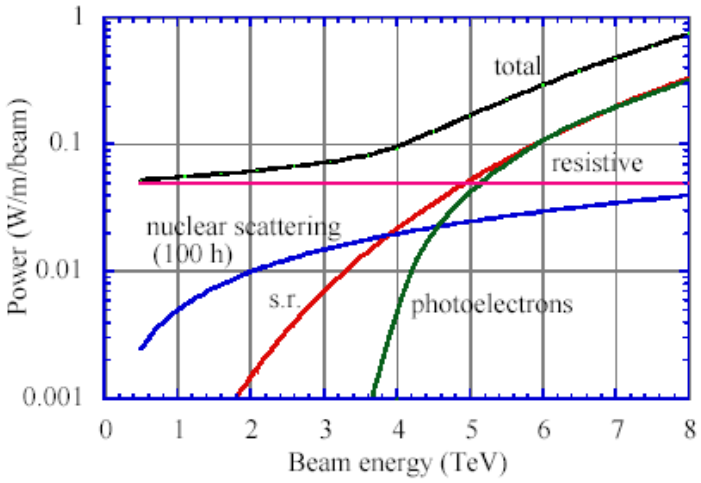

2.16. Losses induced by beam in LHC

- Synchrotron radiation

As already written, because of the centripetal acceleration into magnetic rings, the protons beam emits a synchrotron radiation with a flow of about 10^{7} photons $s^{-1}m^{-1}$, a critical energy of 45.4 eV and a power of 0.22 Wm^{-1}. The radiation flux depends on beam current and energy and on the system bending radius. The flux of photo-desorbed gas is proportional to photons flux and to the molecular desorption yield, defined as the number of emitted particles after collisions per incident particles.

Among the adsorbed gas from walls, the more critical species for vacuum are H_2 ,CO_2, CO, H_2O and CH_4. The following table shows the molecular desorption yield values of several gases for temperature in the range of (4.2K÷300K).

T (K)	H_2	CH_4	CO	CO_2
300	$5.0\ 10^{-4}$	$1.6\ 10^{-3}$	$2.5\ 10^{-4}$	$2.2\ 10^{-4}$
77	$2.5\ 10^{-4}$	$4.0\ 10^{-6}$	$1.5\ 10^{-5}$	$7.0\ 10^{-6}$
4.2	$3.5\ 10^{-5}$	$8.0\ 10^{-7}$	$6.0\ 10^{-6}$	$7.0\ 10^{-6}$

Table 2.3. Molecular desorption yield

The previous results show a decrease of molecular desorption yield with the increase of temperature, with significant values also at very low temperatures. In the figure 2.17 it is possible to observe the desorption yields trend as function of dose, after 3.6 h of LHC functioning at 7 TeV.

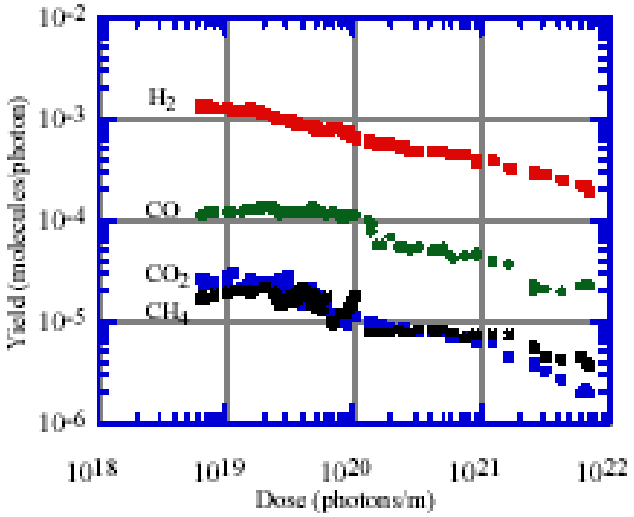

2.17. Molecular desorption yield as function of dose

The H_2 molecular yield from a cupper surface at 10 K is typically in the order of $5{\cdot}10^4$ molecules per photon; this value is considerably grater then values of other species. So molecular hydrogen represents the critical species for desorption.

- Beam current

The interior of *beam pipe* dissipates power in the order of $0.05 Wm^{-1}$, directly depending on resistivity ρ of the vacuum chamber material. For limiting this heat loss and for avoiding the beam instability, it is necessary to maintain low the resistivity of chamber wall. This effect can be obtained covering the beam pipe (made of stainless steel) with a thin cupper layer. In fact, at low temperature the resistivity for pure cupper is strongly reduced and it is possible to observe a gain factor 10^3 times greater than the factor of only stainless steel.

- Photoelectrons

The synchrotron radiation determinates the electrons production through the photoemission and the Auger effect. The produced electrons may create an electronic cloud which may led to the system instability.
The electronic cloud can be caused by the following mechanisms and by their combination:

1) residual gas ionization;
2) photoemission due to synchrotron radiation;
3) secondary emission or multipacting induced by the beam.

When LHC operates at 7 TeV, the main source of primary electrons is photoemission, due to synchrotron radiation. Primary electrons hit the chamber producing secondary electrons and a consequent increase of electronic density during successive crossing of protons beam (fig.2.18).

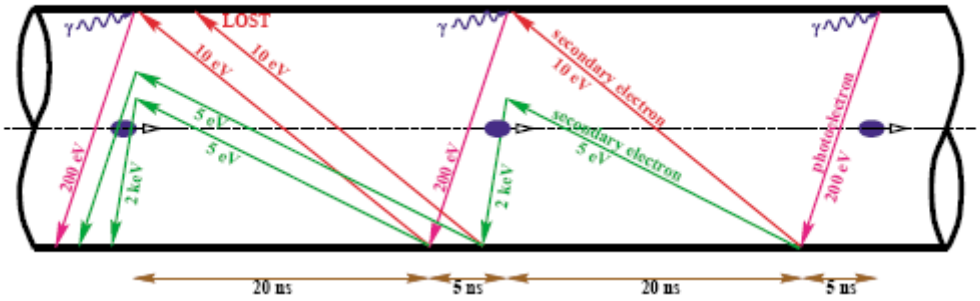

Fig.2.18. Schematically representation of creation mechanism of electronic cloud

The secondary electrons are defined, conventionally, through three contributes: the real secondary electrons (produced from primary electrons), the elastically reflected electrons and re-diffuse electrons.
The electron beam is characterized by a strong electric field, so these electrons may be accelerated and they may transfer their energy to cold walls, creating an intense heat load **[47]**.

- Nuclear scattering

The nuclear scattering of high-energy protons on residual gas generates a secondary particles fall; particles with a sufficient energy escape from the vacuum chamber and deposit their energy on cryo-magnets then they are adsorbed into the system at 1.9K. The loss due to nuclear scattering on residual gas generates a heat load not negligible. So the heat provided to cryogenic system is directly proportional to gas density.
Two limits for residual gas density exist; the first is due to a local heat load which can deteriorates the magnet, while the second is connected to the total heat load in the cryogenic system.
The first limit regards the high pressure regions of system, while the second one can be expressed through the beam lifetime in nuclear scattering (τ).
Considering for protons with an energy of 7 TeV , on hydrogen atoms, a cross section of $\sigma \sim 5\ 10^{-30}\ m^2$, the beam lifetime is given by

$$\frac{1}{\tau} = c\,\sigma\,n \ , \tag{2.1}$$

where c is the lightning speed.
The linear power P(W/m) is proportional to the beam current I and to the beam energy E and it can be expressed as a function of lifetime τ:

$$P = \frac{IE}{c\tau} = 0.93\frac{E(TeV)I(A)}{\tau(h)} \ . \tag{2.2}$$

So for H_2 a lifetime in the order of 100h implies a relative pressure $\leq 1\cdot 10^{-9}$ torr; heavier gases obviously require lower densities, as showed in table 2.4.

Gas	S/s_{H2}	N (m^{-3}) for τ = 100 h
H_2	1	$1\ 10^{15}$
He	1.26	$7.8\ 10^{14}$
CH_4	5.4	$1.8\ 10^{14}$
H_2O	5.4	$1.8\ 10^{14}$
CO	7.8	$1.2\ 10^{14}$
CO_2	12.2	$8.0\ 10^{13}$

Table 2.4.Cross-sections and maximum density for several gas species

The heat loads due to synchrotron radiation and photoelectrons can be limited at about 20 K, inserting a thermally isolated screen (beam screen), cooled by gaseous helium, into the cold bore of vacuum chamber (fig. 2.19).

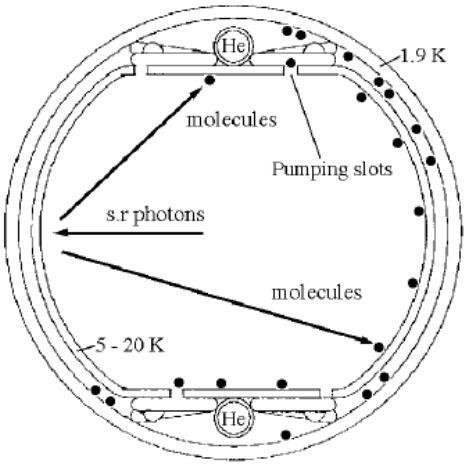

Fig. 2.19. Beam screen section with active cooling into magnet cold bore

The beam screen is equipped for all its length of a series of small holes ("pumping slots") which permit to gas molecules to leave the beam pipe for being adsorbed by cold bore walls.

The pumping holes represent about 4% of the entire beam screen surface.

The beam screen is partially transparent to permit to H_2 molecules desorbed by synchrotron radiation to be permanently pumped by cold bore surface at 1.9K.

Among the desorbed molecules hydrogen has the bigger molecular desorption yield and it represents a very critical species because of high value of its vapour pressure, contrary to beam screen pumping power.

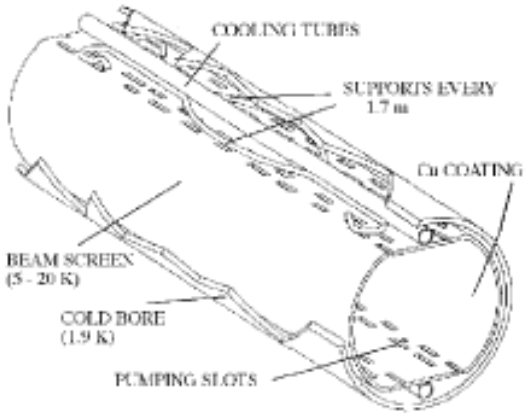

Fig. 2.20. Cold bore and beam screen section

Without *pumping holes* the beam screen cryo-pumping could be little efficient, since the vapour density at equilibrium for a H_2 monolayer (T~5K) overcomes with several orders of magnitude the acceptable limits; instead the presence of holes on surface induces into beam screen an approximately infinite pumping power. So hydrogen and other species may be pumped on a surface at 1.9K with a saturated vapour density negligible. Moreover *pumping holes* give a constant pumping speed which is proportional to the beam screen surface occupied from them.

2.3.3 Gas recycling and instability pressure induced by ions

Because of photons collision on the beam screen inner surface, the cryo-pumped gas molecules on screen may desorb again giving place to the secondary desorption phenomenon. Studies about the secondary adsorption coefficient (recycling coefficient) for H_2 show an increase proportional to the amount of covered surface, until the value of one molecule per photon respect as a monolayer; for H_2 the effect of secondary desorption is very bigger than primary desorption for great screen coverages.

As a consequence of Thermal Desorption and Recycling, only a limited amount of gas stay on beam screen surface; beyond this limit the gas load due to primary desorption migrates to vacuum chamber wall (at 1.9K) through pumping holes, with a pumping speed determined by the total area occupied by holes.

It has been observed that heavier gases as CH_4,CO and CO_2 have very low recycling coefficients for thin physisorbed layers (10-20 monolayers) and these secondary desorption coefficients are indistinguishable respect to primary desorption coefficients; instead for H_2 the coefficients remains constant as is it possible to note in figure 2.21.

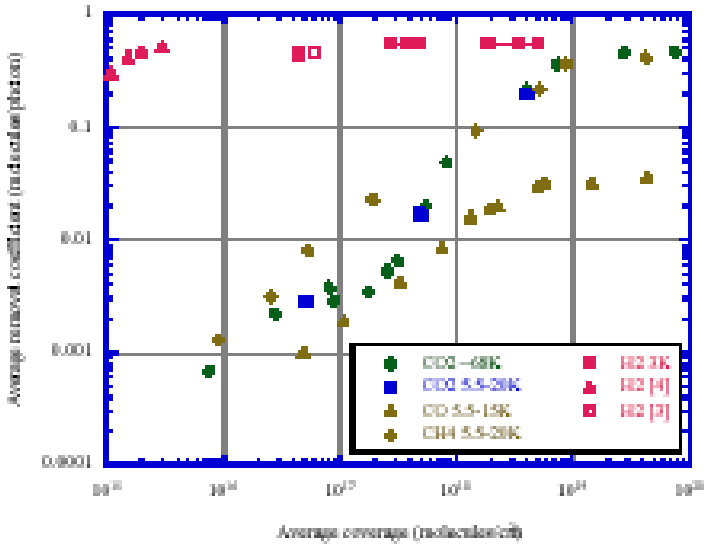

Fig. 2.21. Recycling coefficients as function of coverage for several gas species

The behaviour of the vacuum system is showed in figure 2.22, which describes the H_2 density evolution during the photons exposition.

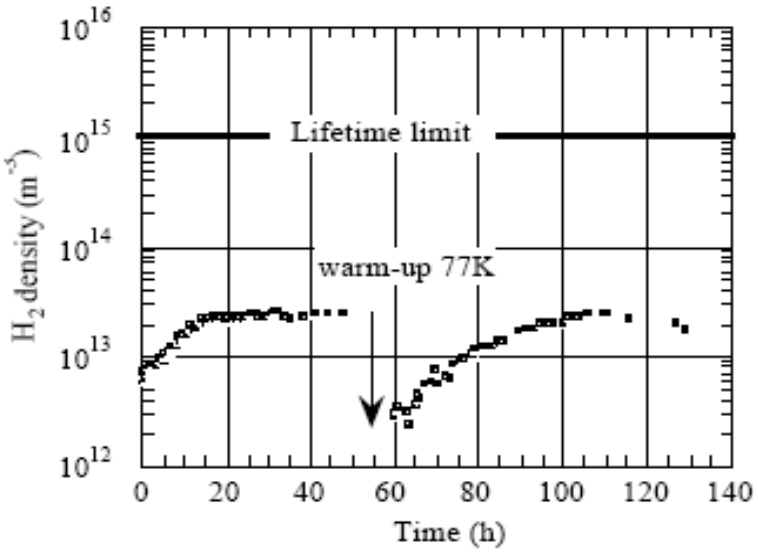

Fig.2.22. H_2 density as function of LHC operation time

The ionization of gas molecules in LHC produces ions, accelerated toward the beam screen or the vacuum chamber, with a final energy higher than 300 eV.

Also energetic ions (as photons) may desorb thin layers of gas molecules, so it is possible to define a molecular yield for ions (η_i); the desorbed molecules may be ionized and they may take part in the consequent desorption process.

So there is an instability pressure due to ions, dependent on the local purity of surface, on the molecular desorption yield and on the effective pumping speed (S_{eff}).

The condition which describes the stability limit is

$$\eta_i I < \frac{e}{\sigma} S_{eff}\,, \tag{2.3}$$

where I is the beam current, e is the electron charge and σ the crossing section of residual gas molecules for high energy protons.

In the cold regions of LHC, the pumping inferior limit is determined by cryosorption on vacuum chamber surface at 1.9 K; the stable vacuum condition is expressed by

$$\eta_i I < \sqrt{\frac{K_B T}{2\pi m}}\,\frac{e}{\sigma} A_f\,, \tag{2.4}$$

where A_f is the pumping holes area per length unit, K_B the Boltzmann constant and m the molecule mass.

With LHC parameters, the calculated stability limit for hydrogen is $\eta_i I = 10^3$ A. Since the primary desorption yield for H_2 is unitary and a great recycling coefficient does not allow the formation of a H_2 thin layer on screen, this limit is acceptable for the LHC cold sections. For sections operating at room temperature the limit is defined by the beam pipe conductance.

2.3.4 Cryosorbent materials

In recent years several materials have been analysed to investigate their cryogenic properties **[48]**. Charcoal is one of the most famous cryosorbent materials and it presents a sufficiently high adsorption power. However this material shows some disadvantages for the use in vacuum chambers: in fact it has a little free surface ad it is difficult to create bonds in surface.

Recent studies about different cryosorbent materials (at 4.2 K) show that the adsorption power of filters, anodized aluminium and other materials is lower than charcoal and only the latter may be utilized in LHC.

Other cryosorbers, as new forms of anodized aluminium, porous cupper and charcoal materials, are analysed in collaboration with numerous research institutes in H_2 cryo-pumping at temperatures in the range of 10 K÷20 K.

Among the cryo-sorbent material which may be utilized in LCH there are also the carbon fibres.

Figure 2.23 shows the pumping speed at different temperatures as function of surface density of adsorbed molecules (molecules/cm^2), for several materials subjected to a fast cooling: anodized aluminium (AA3), porous cupper (Cu 1), charcoal with super-conducting ceramics (C+SCC) and carbon fibres covered by a thin layer of stainless steel.

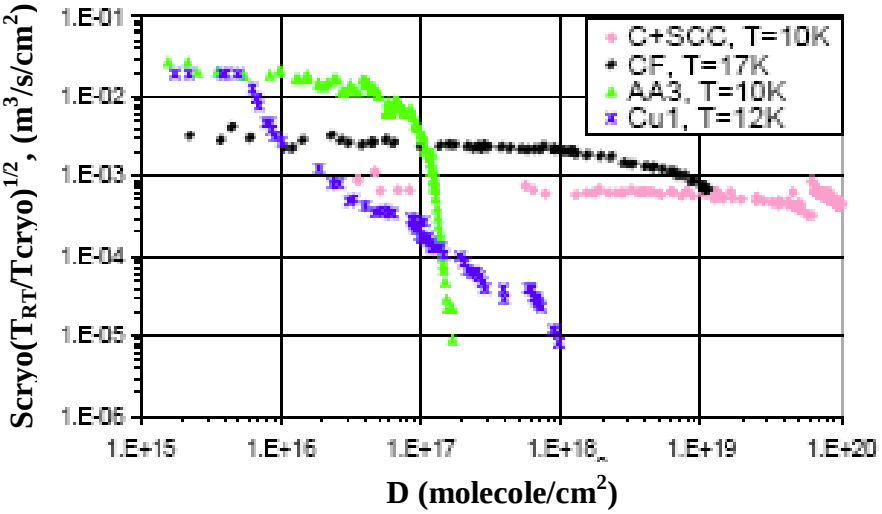

Fig. 2.23. Pumping speed trend for several cryo-sorbent materials as function of H_2 adsorbed molecules density.

It is possible to note that the H_2 adsorption power overcomes the value of 10^{17} molecules/cm only for charcoal and carbon fibres samples, while for other materials the surface density of adsorbed molecules does not have appreciable values. So only charcoal and carbon fibres have the correct characteristics to be used as cryo-sorbers in LHC.

The experimental results described in chapter 4 show that MWCNTs have an efficiency clearly higher than charcoal and they may be a possible solution to vacuum problems of LHC.

Chapter 3

Carbon nanotubes: properties and applications

In this chapter we analyse structure and properties of carbon nanotubes. We focuse our attention on gas adsorption property, particularly on molecular hydrogen adsorption at low temperatures. Problems of Large Hadron Collider vacuum system are due mainly to H_2 desorption from chamber wall caused by synchrotron radiation; we studied gas adsorption properties to candidate carbon nanotubes as good criosorbers in future accelerators.

3.1 Single-Wall Carbon Nanotubes (SWCNT)

Carbon exists in nature in several allotropic structures, depending on the different regular atomic arrangement (fig. 3.1); the main carbon structures are:

- Graphite: described by a planar geometry (hybridization sp^2)
- Diamond: characterized by a three-dimensional tetrahedral geometry (hybridization sp^3)
- Fullerene: formed by regular arrangement of hexagonal and pentagonal atomic structures.

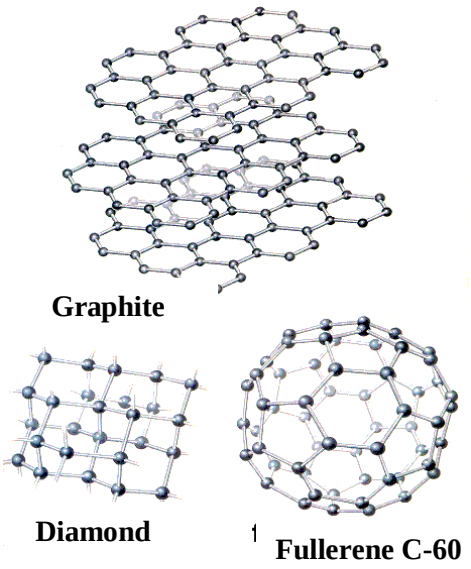

Fig.3.1. Allotropic carbon structures.

In 1991 the researcher Sumio Iijimaal observed that the product of an electric discharge between two carbon electrodes contained structures made of concentric carbon tubes: the nanotubes **[49, 50]**. It is possible to distinguish two general groups of nanotubes: single-walled (SWNT) and multi-walled (MWNT) nanotubes.

An ideal SWNT can be described through a graphitic tube rolled up into itself forming a cylinder, closed at the end by two hemispherical caps (fig.3.2).

Fig. 3.2. Carbon SWNT structure

The lateral wall of cylinder is made only of hexagons, while the two caps are constituted also by pentagons as fullerene(fig. 3.3).

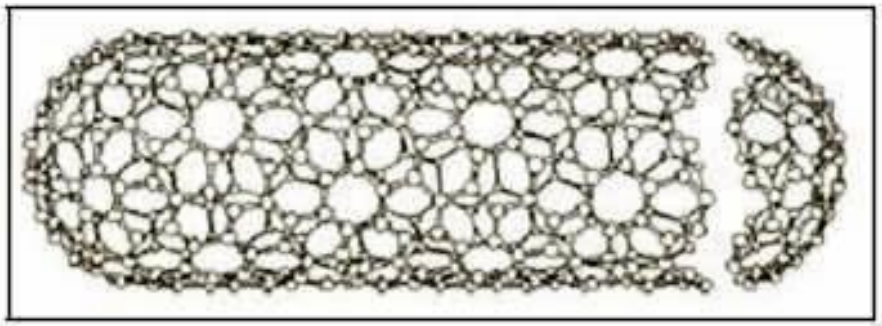

Fig. 3.3. Ideal SWNT closed at the end by two fullerenes.

SWCNT diameter is in the range of 0,7 nm (corresponding to twice the graphite interplanar distance) and 10 nm, but for their big ratio between diameter and length SWCNT are considered as virtually monodimensional nanostructures.

MWCNTs consist of many concentric SWCNT ; their diameter increases with walls number and it is about 10 nm (fig. 3.4). In MWCNT it is possible to observe lip-lip interactions that stabilize the growth.

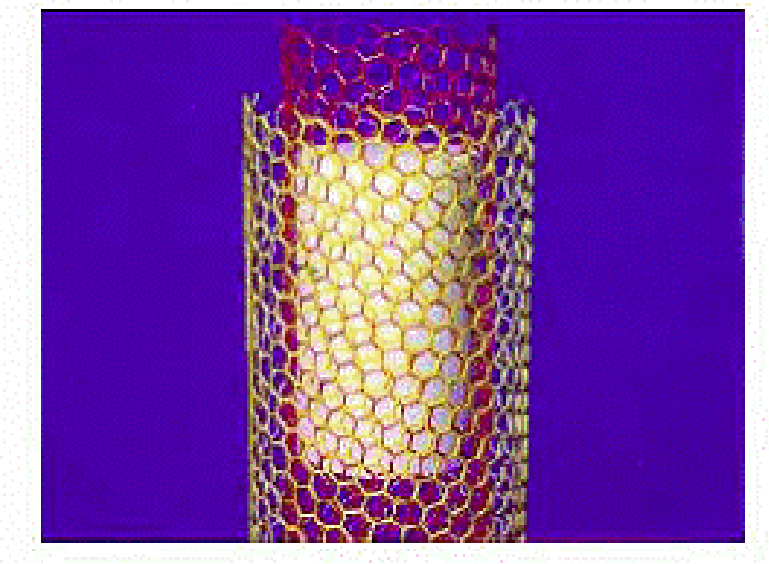

Fig. 3.4. MWCNT example

The CNTs' bonding mechanism is obviously similar to graphite's one. Graphite is characterized by sp_2 hybridization, which occurs when one s-orbital and two p-orbitals combine to form three hybrid sp_2-orbitals (fig.3.5).

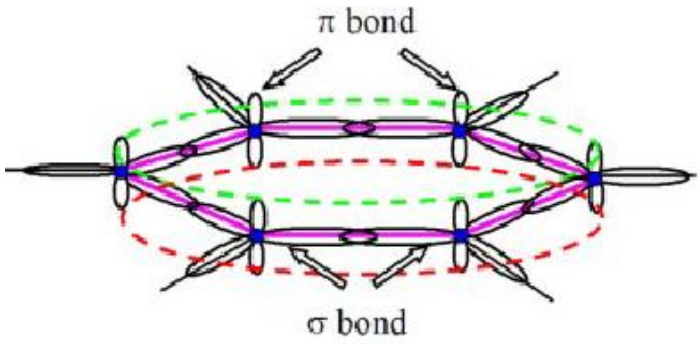

Fig. 3.5. The bonding structure for one graphite plane: σ-bonds connect carbon nuclei atoms (filled circles) in the plane and π-bonds contribute to a delocalization.

The strong covalent bond that binds the atoms in the plane (σ-bond) produces the high stiffness and the high strength of CNts. The p-orbital, perpendicular to the plane, contributes

to interlayer interaction forming a π-bond. This π-bond interacts with the π-bond in the neighboring layer ,but this interaction is weaker than a σ-bond.

So the remaining p-electron of CNT contributes to a delocalized p-electron system **[51]**.

Nanotubes often present structural defects as, for example, the presence of pentagonal and octagonal structure in the lateral wall of cylinder (fig. 3.6).

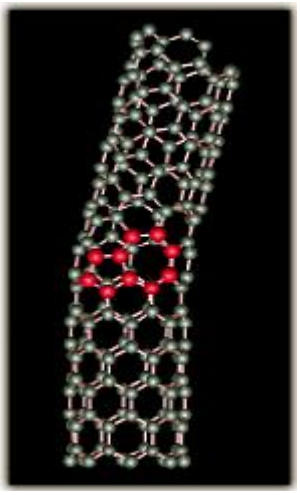

Fig. 3.6. Examples of defects on SWNT nanostructure

Figure 3.7 shows a generic graphitic plane rolled up; it is possible to observe the CNT axes (green line) and $\bar{a}_1$, $\bar{a}_2$ vectors of direct lattice.

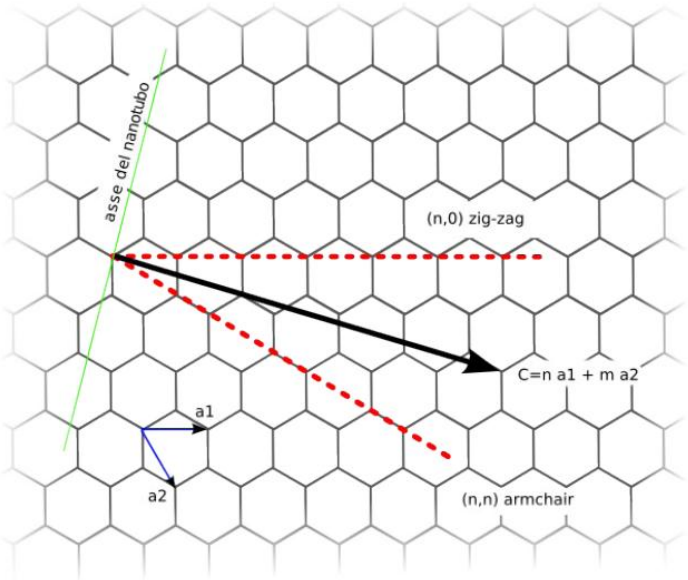

Fig. 3.7. Graphite layer and possible rolling up directions.

The main characteristics of SWCNT are due to *chiral vector* $\boldsymbol{C_h}$, describing the rolling up direction of graphite with respect to its axes and to nanotube length **[59].** This vector links the two carbon atoms that superimpose themselves in nanotube formation and it is due to linear combination of $\bar{a}_1$ ed $\bar{a}_2$:

$$\bar{C}_h = n\bar{a}_1 + m\,\bar{a}_2, \text{ with } m,n \text{ integers, } 0 \leq |m| \leq n \tag{2.1}$$

Based on simple geometry, the diameter d is given by L/π, where L is the length of carbon nanotube circumference:

$$d_t = \frac{L}{\pi} = \frac{|C_h|}{\pi} = \frac{\sqrt{C_h \cdot C_h}}{\pi} = \frac{a}{\pi}\sqrt{n^2 + nm + m^2} \quad \text{Å}, \tag{3.2}$$

where the lattice constant a=2.49 Å= $\sqrt{\bar{a}_1 \cdot \bar{a}}_1 = \sqrt{\bar{a}_2 \cdot \bar{a}_2}$
The angle between chiral vector and the straight line defined by $\bar{a}_1$ is the *chiral angle* θ and some nanotube properties depend on it. Because of the hexagonal symmetry and the honeycomb lattice $0 \leq \theta \leq 30^o$ and it is described by the following equation:

$$\cos\theta = \frac{\bar{C}_h \cdot \bar{a}_1}{|\bar{C}_h||\bar{a}_1|} = \frac{2n+m}{2\sqrt{n^2+nm+m^2}}. \tag{3.3}$$

According to m and n there are several SWCNT typologies, particularly "zigzag" structures correspond to $m = 0$, while "armchair" one for $m = n$; finally if $m \neq n$ (con $m \neq 0$ and $n \neq 0$) it is possible to observe "*chiral* " structures (fig. 3.8).

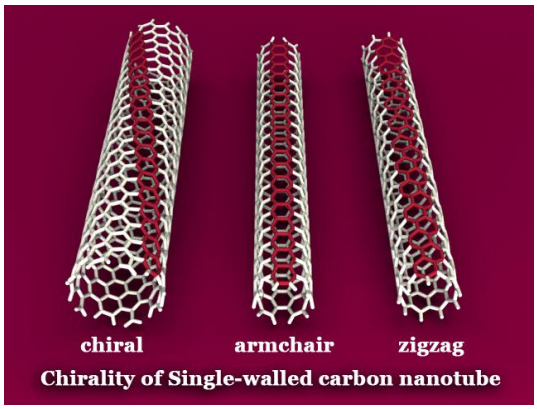

Fig. 2.8. Examples of SWCNT structures: "chiral", "armchair" and "zigzag".

In particular *zigzag* and *armchair* nanotubes correspond to θ=0° and θ=30°, respectively.

Among carbon nanotubes it is also possible to distinguish between *achiral* (symmorphic) or *chiral* (non-symmorphic). The former is a carbon nanotubes whose mirror image has the same structure of the original one, while *chiral* nanotube mirror image cannot be superimposed on to the original one. The only two types of *achiral* carbon nanotubes are *armchair* and *zigzag* nanotubes.

Another important vector characterizing carbon nanotubes is the *translation vector* ***T*** ,defined as the unit vector of a 1D carbon nanotube. The vector ***T*** is parallel to nanotube axis and it is normal to the vector $\boldsymbol{C}_h$ in the unrolled honeycomb lattice (fig. 3.7).

The expression of vector ***T*** in terms of the basic vectors is **[52]**:

$$\bar{T} = t_1\bar{a}_1 + t_2\,\bar{a}_2\text{, with } t_1 \text{ and } t_2 \text{ integers.} \qquad (3.4)$$

From the condition $\boldsymbol{C_h} \cdot \boldsymbol{T} = \boldsymbol{0}$, is it possible to determinate the expression for t_1 and t_2:

$$t_1 = \frac{2m+n}{d_R},\ t_2 = -\frac{2n+m}{d_R} \qquad (3.5)$$

where d_R is the greatest common divisor of (2m + n) and (2n + m). Defining *d* as the greatest common divisor of *m* and *n*, d_R is given by:

$$\begin{cases} d \text{ if } n-m \text{ is not a multiple of } 3d \\ 3d \text{ if } m \text{ is a multiple of } 3d \end{cases}.$$

The length of the translation vector ***T*** is defined by

$$T = \sqrt{3}L / d_R, \qquad (3.6)$$

where L is the circumferential nanotube length.

The length of ***T*** is reduced when *m* and *n* have a common divisor or when (*n*-*m*) is a multiple of 3*d*.

Furthermore, dividing the area of nanotube unit cell $\left|\bar{C}_h \times T\right|$ by the area of a hexagon ($\left|\bar{a}_1 \times \bar{a}_2\right|$) it is possible to obtain the number of hexagons per unit cell (N) as a function of *m* and *n*:

$$N = \frac{\left|\overline{C}_h \times \overline{T}\right|}{\left|\overline{a}_1 \times \overline{a}_2\right|} = \frac{2\left(m^2 + n^2 + nm\right)}{d_R} = \frac{2L^2}{a^2 d_R}, \tag{3.7}$$

where d_R is given by equation (3.5). Each hexagon contains to carbon atoms, so there are N carbon atoms in each unit cell of the carbon nanotube.

The coordinates of carbon atoms in a nanotubes unit cell are described by the vector ***R***, expressed in terms of its projections on the orthogonal vectors $\boldsymbol{C_h}$ and ***T*** (fig. 3.9):

$$\overline{R} = p\overline{a}_1 + q\,\overline{a}_2, \tag{3.8}$$

where p and q are integers and they not have any common divisor except for unity.

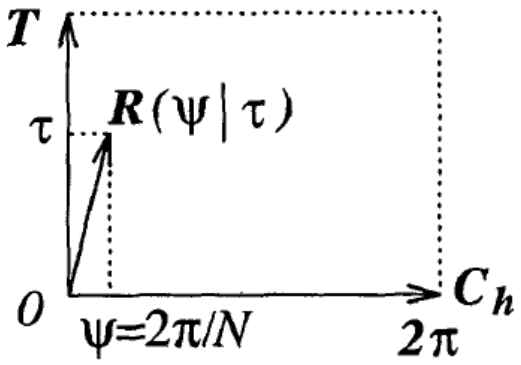

Fig. 3.9. The symmetry vector ψ denotes the angle of rotation around the nanotube axes and τ is the translation in the ***T*** direction.

It is possible to note that

$$\frac{\overline{C}_h \cdot \overline{R}}{L} = \frac{\left|\overline{T} \times \overline{R}\right|}{T}, \tag{3.9}$$

where

$$\overline{T} \times \overline{R} = \left(t_1 q - t_2 p\right)\left(\overline{a}_1 \times \overline{a}_2\right) \tag{3.10}$$

and $\left(t_1 q - t_2 p\right)$ is an integer.

It is important to choose p and q of ***R*** to form the smallest site vector (i = 1),such that

$$\left(t_1 q - t_2 p\right) = 1, (0 < mp - nq \leq \mathrm{N}). \tag{3.11}$$

The vector ***R*** consists of a rotation around the nanotube axis, by an angle ψ, combined with a translation τ in the direction of ***T***, and reflect the basic space group symmetry operation of a chiral nanotube.

The projection of ***R*** on $\boldsymbol{C_h}$ gives the angle ψ, while the projection of ***R*** in ***T*** represents the translation τ of the basic symmetry operation of the 1D space group of the carbon nanotube.

From definition of ***T***, *N*, *d* and from the equation (3.11), it is possible to obtain the expression for the length of τ and the rotation angle ψ:

$$\tau = \frac{\left|\bar{R} \times \bar{C}_h\right|}{L} = \frac{(mp - nq)\left|\bar{a}_1 \times \bar{a}_2\right|}{L} = \frac{(mp - nq)T}{N} \tag{3.12}$$

$$\psi = \frac{\left|\bar{T} \times \bar{R}\right|}{T}\frac{2\pi}{L} = \frac{d(t_1 q - t_2 p)}{\sqrt{3}L}\frac{\sqrt{3}a^2}{2} = \frac{2\pi}{N}, \tag{3.13}$$

where N is the number of hexagons in the 1D unit cell of the nanutube (eq. (3.7)).

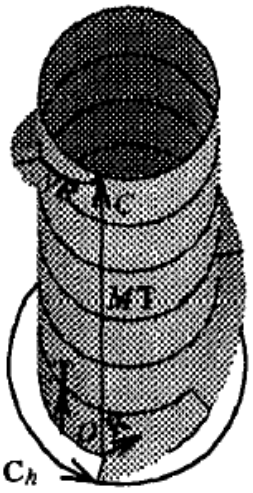

Fig. 3.10. The vector $N\boldsymbol{R}=(\psi \mid \tau)^N$ on the cylindrical surface, in the case of C_h=(4,2) and M=6.

The symmetry operator $(\psi \mid \tau)^N$ brings the lattice point O to an equivalent lattice point C (fig.3.10); this mechanism is described by the equation below:

$$N\bar{R} = \bar{C}_h + M\bar{T}, \tag{3.14}$$

where $M = mp\text{-}nq$ is an integer that gives indication of the number of vector $\boldsymbol{T}$ that are necessary for reaching the distance from O to $N\boldsymbol{R}$.

After a rotation of 2π around the tube, the vector $N\boldsymbol{R}$ reaches a lattice point C equivalent to O, but separated from it by the vector $M\boldsymbol{T}$.

The unit cell for a carbon nanotube in real space is represented by the rectangle generated by the chiral vector $\boldsymbol{C_h}$ and the translation vector $\boldsymbol{T}$ (fig. 3.11).

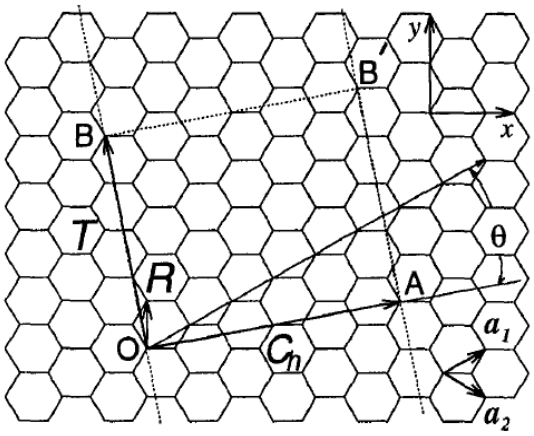

Fig. 3.11. The unrolled honeycomb lattice of a nanotube. $\boldsymbol{C}_h$ is the chiral vector, $\boldsymbol{T}$ the translational vector and $\boldsymbol{R}$ the symmetry vector of the nanotube. The rectangle $\boldsymbol{OAB'B}$ defines the unit cell for the nanotube.

In the unit cell there are 2N carbon atoms, there are N pairs of π bonding and anti-bonding π^* electronic energy bands.

Defining $\boldsymbol{K}_2$ as the reciprocal lattice vector and $\boldsymbol{K}_1$ as a vector that gives the discrete k values in the direction of C_h, their expression is obtained from the relation $\overline{R}_i \cdot \overline{K}_j = 2\pi\delta_{ij}$, where $\boldsymbol{R}_i$ and $\boldsymbol{K}_j$ are, respectively, the lattice vectors in real and in reciprocal space.

Using the definition of t_1, t_2 and N and the following relations

$$\overline{C}_h \cdot \overline{K}_1 = 2\pi \qquad \overline{T} \cdot \overline{K}_1 = 0$$
$$\overline{C}_h \cdot \overline{K}_2 = 0 \qquad \overline{T} \cdot \overline{K}_2 = 2\pi \quad , \tag{3.15}$$

the expression for $\boldsymbol{K}_1$ and $\boldsymbol{K}_2$ are:

$$\overline{K}_1 = \frac{1}{N}\left(-t_2\overline{b}_1 + t_1\overline{b}_2\right) \qquad \overline{K}_2 = \frac{1}{N}\left(m\overline{b}_1 - n\overline{b}_2\right), \tag{3.16}$$

where $\boldsymbol{b}_1$ and $\boldsymbol{b}_2$ are the reciprocal lattice vectors of two-dimensional graphite (fig. 3.12).

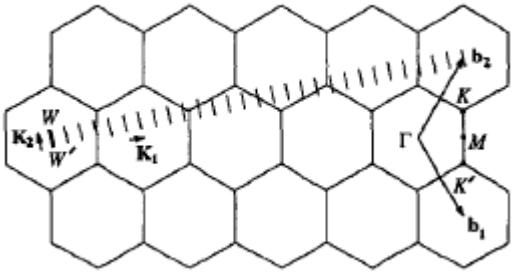

Fig. 3.12. The Brillouin zone of a carbon nanotube, represented by the line segment WW'.

The vector $\boldsymbol{K}_1$ and $\boldsymbol{K}_2$ are reciprocal lattice vectors corresponding to $\boldsymbol{C}_h$ and $\boldsymbol{T}$, respectively. The first Brillouin zone of carbon nanotube is represented by the segment WW'. From equation (3.16), N$\boldsymbol{K}_1$ corresponds to a reciprocal lattice vector of two dimensional graphite, so two wave vector which differ by N$\boldsymbol{K}_1$ are equivalent. The length of the one-dimensional first Brillouin zone , corresponding to the length of all the parallel lines in figure 2.12, is $2\pi/T$. Because of the translational symmetry of $\boldsymbol{T}$, there are continuous wave vectors in the K2 direction for a nanotube of infinite length. It has been experimentally observed that for a nanotube of finite length L, the space between wave vector is $2\pi/L$ **[52]**.

3.2 Electronic structure of Single-Wall Carbon Nanotubes

The electronic structure of a single-wall carbon nanotube can be obtained simply from that of two-dimensional graphite. Using the periodic boundary condition for the chiral vector $\boldsymbol{C}_h$, the wave vector associated to the $\boldsymbol{C}_h$ direction becomes quantized, while the wave vector associated to the direction of the translational vector $\boldsymbol{T}$ is continuous for a nanotube of infinite length. Thus the energy bands consist in a set of one-dimensional energy dispersion relations. If E_{g2D} is the energy dispersion relations of two dimensional graphite, the 1D energy dispersion relations for single-wall carbon nanotubes are given by

$$E_{\mu}(k) = E_{g2D}\left(k\frac{\overline{K}_2}{|\overline{K}_2|} + \mu\overline{K}_1 \right), \quad \text{with } \mu=0,\ldots..,N\text{-}1 \text{ and } \quad -\pi/T < k < \pi/T \qquad (3.17)$$

The N pairs of energy dispersion curves, described in the previous equation, correspond to the cross section of the two-dimensional energy dispersion surface, shown in figure 3.13.

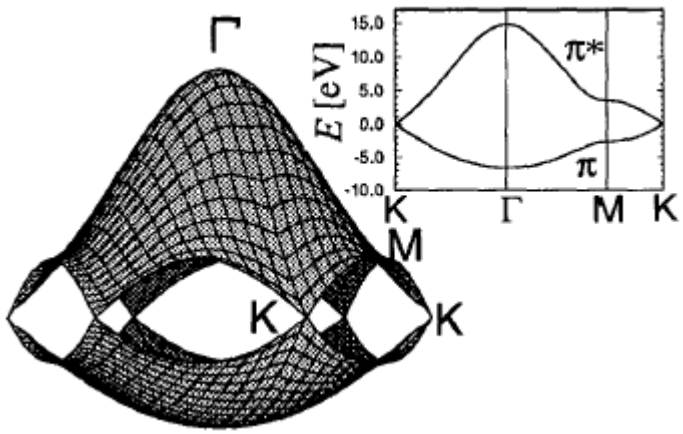

Fig. 3.13. The energy dispersion relation for 2D graphite in the whole region of the Brillouin zone

For a particular (n,m) nanotube, if the cutting line passes through a K point of the 2D Brillouin zone, where the π and π^* energy band of 2D graphite are degenerated by symmetry, the 1D energy band has a zero energy gap (inset of figure 2.13). In this case the carbon nanotube are metallic and the density of state at the Fermi level has a finite value, while if the cutting line does not pass through a K point it is expected that these nanotubes have a semiconducting behaviour with a finite energy gap between the valence and the conductance bands (fig. 3.14).

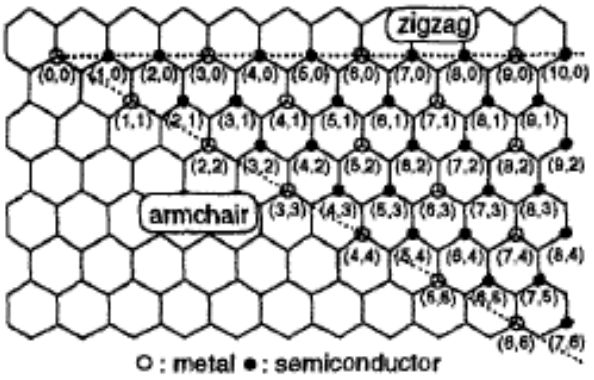

Fig. 3.14. Map of chiral vectors (n,m): the carbon nanotube (n,m) metallic and semi-conductive are denoted , respectively, by open and solid circles.

In particular SWCNTs can be characterized by electric properties of a semiconductor with an energetic gap in the range of (0,2 ÷ 1.2) eV in the band structure or of a conductor: nanotubes with *armchair* structure (*n*,*n*) have always metallic characteristic, while *zigzag* nanotubes *(n,0)* show a metallic behaviour if *n* is multiple of 3, otherwise they have semi-conductive properties.

3.2.1 Energy dispersion relation of Armchair, Zigzag and Chiral nanotube

To obtain explicit expression for the dispersion relations, it is useful to analyse the simplest case of nanotube having the highest symmetry.
Starting from the energy dispersion relation from the two-dimensional graphite

$$\mathrm{E}_{\mathrm{g2D}}\left(k_x, k_y\right) = \pm t\left\{1 + 4\cos\left(\frac{\sqrt{3}k_x a}{2}\right)\cos\left(\frac{k_y a}{2}\right) + 4\cos^2\left(\frac{k_y a}{2}\right)\right\}^{1/2} \qquad (3.18)$$

and using the discrete allowed values for the wave vector $k_{x,q}$

$$n\sqrt{3}k_{x,q}a = 2\pi q \qquad (q=1,\ldots\ldots,2n)\,, \qquad (3.19)$$

is it possible to obtain the energy dispersion relations $E_q^a(k)$ for the armchair nanotube (C_h=(*n*,*n*):

$$\mathrm{E}_{\mathrm{q}}^{\mathrm{a}}(k) = \pm t\left\{1 \pm 4\cos\left(\frac{q\pi}{n}\right)\cos\left(\frac{ka}{2}\right) + 4\cos^2\left(\frac{ka}{2}\right)\right\}^{1/2}, \qquad (3.20)$$

in which $-\pi < ka < \pi$, q = 1,….2n, the superscript *a* indicates an armchair type and ***k*** is a one-dimensional vector in the direction corresponding to the Γ to K point vector in the two-dimensional Brillouin zone of graphite (fig.3.15).

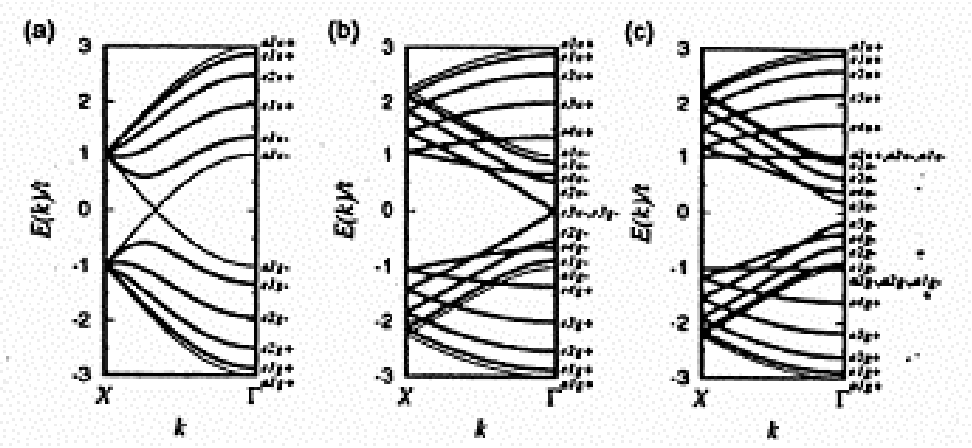

Fig.3.15. One-dimensional energy dispersion relations for (a) armchair (5,5), (b) zigzag (9,0) and (c) zigzag (10,0) carbon nanotubes. The a-bands are no-degenerate ,while the e-bands are doubly degenerate at a general k-point. x point for armchair and zigzag nanotubes correspond to $k = \pm \pi / a$ and $k = \pm \pi / \left(\sqrt{3} a \right)$, respectively. In figure a) it is possible to observe that armchair structure has semi-conductive characteristic, how confirmed by the absence of a gap; figure b) represents the properties of a semi-conductive zigzag nanotube (9,0), how showed by the small gap width(~ 0.2 eV); figure c) describes the semi-conductive behaviour of a zigzag nanotube (10,0) with a big gap(~1.2 eV).

For the (5,5) armchair nanotube (fig. 3.15) there are six dispersion relations $\mathrm{E}_{\mathrm{q}}^{\mathrm{a}}(k)$ for both the conduction and the valence band. In each case, the two bands labeled by "a" are no-degenerate, while the four bands signed with "e" are doubly degenerate, for a total of ten levels consistent with the ten hexagons around the circumference of the (5,5) armchair nanotube.

The two carbon atoms on the same sublattice of a graphene sheet are symmetrically equivalent and it causes a degeneracy of the energy bands at the boundary of the Brillouin zone. The valence and conduction bands for the armchair nanotubes cross at a point $k = 2\pi / (3a)$; the crossing takes place at the Fermi level and the energy bands are symmetric for ± k values (fig.3.15). Because of this degeneration point between valence and conduction bands, the (5,5) armchair nanotube is a zero-gap semiconductor, that will exhibit metallic conduction at finite temperatures, because only infinitesimal excitation are needed to excite carriers into the conduction band.

In general, (*n*,*n*) armchair nanotubes have a band degeneracy between the highest valence band and the lowest conduction band at $k = \pm 2\pi / (3a)$, with the band cross at Fermi level.

All armchair nanotubes are expected to exhibit metallic conduction, similarly to 2D graphene sheets.

For (*n*,o) zigzag nanotube, the energy band $E_q^z(k)$ can be obtained from equation (3.18) by writing the periodic boundary condition on k_y:

$$n\,k_{y,q}a = 2\pi q \quad (q=1,\ldots\ldots,2n)\,, \tag{3.21}$$

and the 1D dispersion relations for (*n*,o) zigzag nanotube is:

$$E_q^z(k) = \pm t\left\{1 \pm \cos\left(\frac{q\pi}{n}\right) 4\cos\left(\frac{\sqrt{3}ka}{2}\right) + 4\cos^2\left(\frac{q\pi}{n}\right)\right\}^{1/2}\,, \tag{3.22}$$

with $\left(-\frac{\pi}{\sqrt{3}} < ka < \frac{\pi}{\sqrt{3}}\right)$ and (q = 1,….2n).

How is it possible to note in figure 2.15, for the (9,0) nanotube there is no energy gap at k = 0, while (10,0) nanotube shows it. Particularly, for the (10,0) nanotube there is a dispersion energy band at n= ½, which gives E(π/a) = ± t. In general for a (*n*,0) zigzag nanotube, when *n* is a multiple of 3 the energy gap at k = 0 is zero, while when *n* is not a multiple of 3 there is an energy gap at k=0.

Nanotube electronic structure can be metallic or semi-conductive according to its diameter and its chirality. **[53, 54]**. The band gap of semi-conductive CNts is approximately inversely proportional to the tube diameter.

It has been noted that the band degeneracies for metallic nanotube correspond to $k = \pm 2\pi/(3T)$ for armchair nanotube and $k = 0$ for zigzag nanotube; in the latter case these k-values are also the locations of the band gaps for semiconducting nanotubes. In general k values denote the position of the energy gaps for the case of chiral nanotubes. It is important to remember that a (*n*,*m*) chiral nanotube is metallic if *n*-*m* is a multiple of 3. More generally the nanotubes can be classified into three general categories, if: *n*-*m* is or not a multiple of 3 and if *n*-*m* is or not a multiple of 3*d* whenever *n*-*m* is a multiple of 3 ,where *d* is the highest common divisor of *n* and *m* (see table 3.1).

Properties	$gcd(n-m,3)^{(a)}$	$d_R^{(b)}$	Degeneracy$^{(c)}$
Semiconductor	1	d	0 (Energy gap $\propto 1/d_t$).
Metal-1	3	d	4 at $k=0$.$^{(d)}$
Metal-2	3	$3d$	2 at $k=\pm 2\pi/3T$.

Table 3.1: Classification of carbon nanotube properties, $\mathbf{C}_h$=(n,m); *gcd* denotes the greatest common divisor

3.2.2 Density of States and Energy gap

The density of states per unit length along the tube axis, for metallic nanotube, is given by

$$N(E_F) = \frac{8}{\sqrt{3}\pi a|t|} \ , \tag{3.23}$$

where a is the lattice constant of graphene layer and $|t|$ is the nearest neighbor C-C tight binding overlap energy.

There is an important energy dependence of nanotube density of states, as shown in figure 3.16, in which it is described the density of state for metallic (9,0) and semiconducting (10,0) zigzag nanotube.

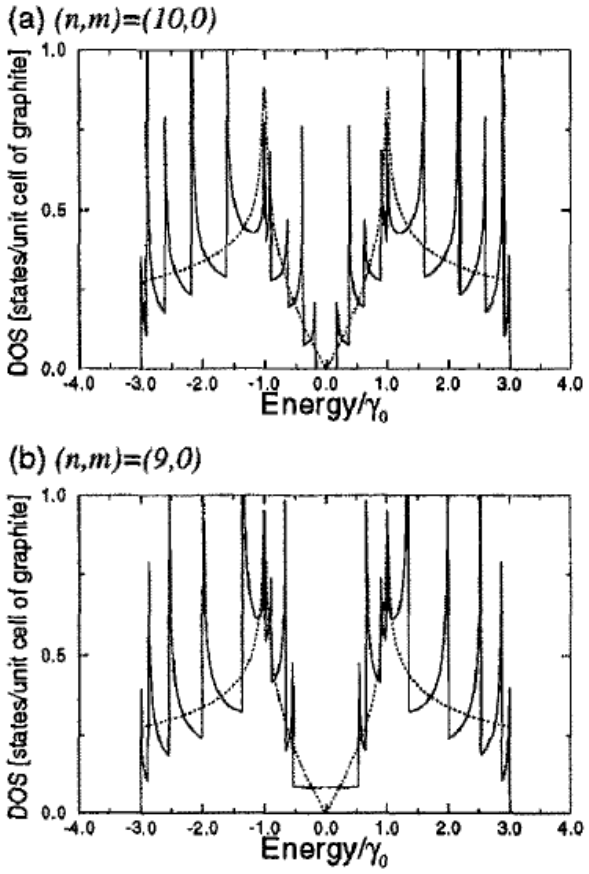

Fig. 3.16. Electronic 1D density of states for unit cell of a 2D graphene sheet for (a) a (10,0) zigzag nanotube which has semi-conducting behavior and (b) a (9,0) zigzag nanotube which has metallic behavior. γ_0 is the nearest neighbour C-C tight binding overlap energy for a graphite sheet.

It is important to note that the density of states near the Fermi level E_F (at E=0) is zero for semiconducting nanotube, but is not-zero for metallic nanotube. Moreover for semiconducting nanotubes, the gap energy depends on the reciprocal nanotube diameter d_t, through the following relation:

$$E_g = \frac{|t|\, a_{C-C}}{d_t}, \tag{3.24}$$

where $a_{C-C} = a/\sqrt{3}$ is the nearest neighbour C-C distance on a graphene sheet. This result is independent on the chiral angle of the semiconducting nanotube and it is important because allows measurements on individual semiconducting nanotube, which are characterized only with regard to nanotube diameter without regard to their chiral angles.

Since about one third of the cylinder of a multi-wall nanotube are conducting , certain electronic properties, such as the electrical conductivity of nanotubes, will be dominated only by the contribute from the conducting constituent.

3.3 Multi-Wall Carbon Nanotubes

Multi-wall carbon nanotubes physical properties have not been described in detail because of the difficulty of making measurements on the individual shell of the nanotube, but they are characterized by interesting properties.

For two coaxial nanotubes which share the same nanotube axis, the chiral vector of the inner and the outer nanotubes can be determined separately. The structure will not be commensurate with each other in all concentric nanotube. For an (n,m) nanotubes, the length of the chiral vector $\boldsymbol{C}_{\mathrm{h}}$ is proportional to an irrational number: $\left|\overline{C}_h\right| = a\sqrt{n^2 + nm + m^2}$

The only commensurate case are the cases of achiral co-axial nanotubes for the two armchairs nanotube (n_1,m_1), (n_2,m_2) and for two zigzag nanotubes (n_1,0), (n_2,0), in which the translational vectors $\boldsymbol{T}$ are the same and, respectively, T = a and $T = \sqrt{3}a$.

It is clear that an armchair nanotube and a zigzag nanotube cannot be commensurate in the direction of the z axis, because the ratio of T is $1/\sqrt{3}$. Instead for the general case of two chiral nanotube, the ratio of the $\boldsymbol{T}$ vector will be an irrational number because $\boldsymbol{T}$ length is an irrational number in units of a ($T = \sqrt{3}L/d_R$, see Eq. (3.6)).

In the case of incommensurate co-axial nanotube no periodicity appears along the *x* axis, so for the inner and the outer nanotubes will not be any atoms in a line parallel to the *x* axis. When we slide the inner nanotube along the *z* axis relative to the outer nanotube, the elastic potential is a periodic function, with a period that is the larger value of the $\boldsymbol{T}$ vector for the constituent nanotube. For a great number of carbon atoms in the unit cell of the constituent nanotube, the potential becomes flat, since the average of the inter-atomic potential at different distances does not depend on *z*.

The nanotube has two degenerate share modes in the *x* and the *y* direction and a third shear mode which corresponds to the rotation around the *z* axis. Since there are two chiral vectors in a plane perpendicular to the nanotube axis, the rotation around the *z* axis has a periodicity of

$2\pi/d_c$, where d_c is the common divisor of the four integers n_1, n_2, m_1 and m_2 for the (n_1,m_1)and (n_2,m_2) nanotubes. So the motion will be smoother, the smaller is the value of d_c. The direction of the normal mode displacement is determined by the two chiral vectors. It is expected a downward shift for the shear stress between the adjacent walls of a multi-wall nanotube, relative to the shear mode in graphite. Many nanotubes present caps which prevent the sliding motion; the result of the sliding motion will be a rotational mode.

The electronic structure for a commensurate double carbon nanotube has been calculated by a tight-binding calculation. In this calculation, for the largest interlayer interaction in graphite associated with the overlap of the wave function of the two π electron is used the value γ_1= 0.35eV, with a separation between the two A carbon atoms (0,0,*c*). Moreover the interlayer interaction between two carbon atoms on two different shells, with a separation *r*, is γ_1 exp(-Ar), where A=1/a is an empirical damp factor. In the calculated results for the commensurate (5,5)-(10,10) and (9,0)-(18,0) nanotube is it possible to observe that the energy dispersion curve repeals the other one at the crossing point (anti-crossing), with the same symmetry of the wave functions belonging to the two different nanotubes.

Although it is important to take account of the interlayer interaction, the results show that the electronic property of a two shell coaxial nanotube may be the sum of the electronic structure of the two independent nanotubes, except for the anti-crossing phenomenon. The calculation shows that the constituent nanotube remains either metallic or semiconducting, depending on the chirality of the constituent nanotube. If the electronic structure of a multi-wall carbon nanotube is determined by the electronic structure of the constituent single-wall nanotube, in a STM experiment only the outermost nanotube contributes to the STM image or to the STM conductance measurement.

In the limit of large diameters, the multi-wall carbon nanotubes have the properties of graphite. In the multi-layer structure, the cross section of the hollow core decreases when the numbers of the carbon layers increases, so the multi-wall structure would be useful to obtain high strength per unit area in the direction of nanotube axis.

3.4 Carbon nanotube bundles

In this work our samples were not constituted by isolated carbon nanotubes, but by disordered systems as bundles. Nanotubes have a strong tendency to aggregate into bundles bound by Van der Waals interactions.

Properties of these disordered systems are mediated on isolated nanotube properties; particularly porosity and adsorption properties are enhanced by the disordered state.

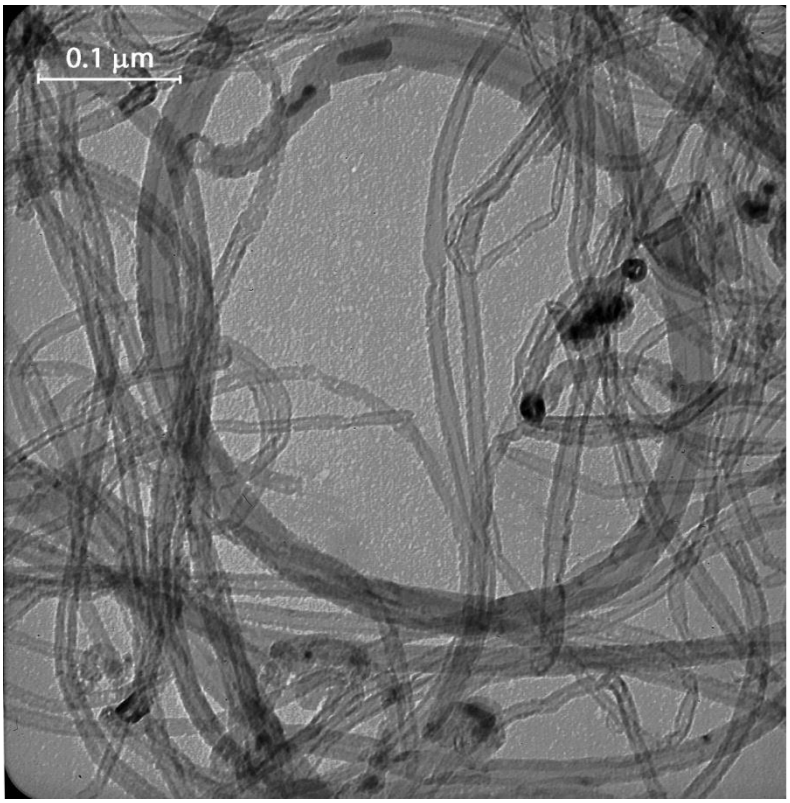

Fig. 3.17. Transmission electron micrograph of multi walled carbon nanotube sample used in this study.

In fact gas molecules are not adsorbed into a single nanotube, but they more easily occupy spaces between several nanotubes. Carbon nanotubes bundles and the other disordered structures are more porous then isolated carbon nanotubes, so also adsorption properties are much better in disordered states.

3.5 CNTs properties

Many studies have been effectuated to determine physical and chemical properties of nanotubes both through direct experimentation on samples and through simulations.
Some of the main properties and their connection with nanotubes structures are analysed below.

- **Gas Adsorption and capillarity**

Pores of molecular dimensions can adsorb large quantities of gases owing to the enhanced density of the adsorbed materials inside the pores, as consequence of the attractive potential of the pore walls. Carbon nanotubes, which typically have diameters of a few nanometres, should be able to draw up liquids by capillarity and this effect has been seen for low-surface-tension liquids in large-diameter, multi-wall carbon nanotubes **[57]**. Nanotubes are not "super-straws," although they can be wet and filled by substances having low surface tension, such as sulphur, selenium and cesium, with an upper limit to this tension less than 200 millinewtons per meter. This limit implies that typical pure metals will not be drawn into the inner cavity of nanotubes through capillarity, whereas water and organic solvents will. These results have important implications for the further use of carbon nanotubes in experiments on a nanometer scale.
Dillon *et al.* **[58]** show that a gas can condense to high density inside narrow single-wall carbon nanotubes. Temperature-programmed desorption spectroscopy shows that hydrogen will condense inside SWCNTs under conditions that do not induce adsorption within a standard mesoporous activated carbon. Dillon *et al.* (**[58]**) analyse the H_2 adsorption on both SWCNT soots and amorphous carbon (AC). The desorption must be from nanoporous environments associated with the high–surface-area amorphous carbon fractions present in material. So the results show that the signal from SWCNT samples is about 10 times greater then the signal from AC, consistent with the higher amorphous carbon content in SWCNTs.
The very high hydrogen uptake in these materials suggests that they may be effective as hydrogen-storage materials, for example for fuel-cell electric vehicles.
The hydrogen adsorption on MWCNT will be analysed in detail in chapter 4.

- **Mechanics properties**

The mechanics resistance of a material depends on several factors, also on the strength of link between the atoms and on the presence of structural defects in crystal lattice. In graphite and in carbon nanotubes the characteristic elastic properties are due to three kinds of forces: the strong σ-bonding, π bonding and the weak interlayer interaction.

To break a nanotube with non defects it is necessary to split all covalent C-C links between the atoms, but these bonds are the strongest in nature so nanotubes have an high mechanics resistance.

These materials are also very flexible and they can be repeatedly bend at about 90^o without damns.

By rolling a graphite sheet to form a single-wall carbon nanotube, the total energy of the nanotube is increased by the strain energy associated with the curvature of the nanotube. The strain energy increases with nanotube diameter decrease, so a nanotube with a small diameter may be less stable than a nanotube with a large diameter.

Single-wall carbon nanotubes have many mechanical properties of carbon fibres, but in addition they are characterized by other important properties as flexibility, their ability to withstand twisting distortion and compression without fracture. Moreover carbon nanotubes show excellent strength characteristic under extension; in fact some studies indicate an increase of several percent in their length without fracture.

Although the π electrons contribution to the elastic energy is smaller than the σ electrons one, it is however important to obtain the lattice distortion, well known as Peierls distortion.

If a single-wall carbon nanotube is considered as an elastic sheet, the strain energy E_σ as a function of nanotube diameter d_t is:

$$E_\sigma = \frac{\pi E T d_f^3}{6 d_t}, \tag{3.25}$$

where E_σ is the elastic modulus of the sheet, T is the nanotube length per 1D unit cell in the direction of the axis and d_f is the thickness of the thin film. Since the number of carbon atoms for unit cell $N = 2LT/\left(\sqrt{3}a^2\right)$ (see eq. (3.7)) is proportional to d_t , because $L = 2\pi d_t$, the strain energy per carbon atoms results inversely proportional to the square of the nanotube diameter:

$$\frac{E_\sigma}{N} = \frac{\sqrt{3} E d_f^3 a^2}{24 d_t^2}. \tag{3.26}$$

The energy dependence on d_t^{-2} is confirmed by many studies about the strain energies for nanotubes with different diameters and chiralities, as shown in fig 3.18.

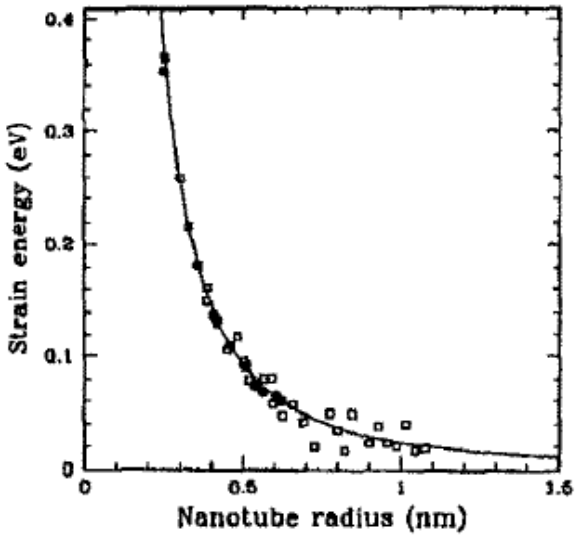

Fig. 3.18. Strain energy per carbon atom E_σ as a function of nanotube radius ($r_t = d_t / 2$). Is evident the square dependence of E_σ on $1/ d_t$.

The small deviation of the strain energy as function of the nanotube radius suggests that there is a small dependence of E_σ / N from chirality.

When a force acts perpendicularly to the nanotube axis, the nanotube bends, as described by the Young's modulus Y.

The deflection *d* of a cantilever of length *l* , subjected to a force *f* at its free end, is given by

$$d = \frac{f\, l^3}{3YI}, \tag{3.27}$$

where I is the moment of inertia of the cross-section of the nanotube about its axis: $I = \pi\left(r_0^4 - r_i^4\right)/4$, in which r_0 and r_i are respectively the outer and the inner radii of an

elastic cylinder. Is it possible to calculate the Young's modulus for a single nanotube using equation (3.27) and considering the wall thickness to be 3.44 Å.

When the diameter of single-wall nanotube increases, the nanotube is unstable in the direction perpendicular to its surface, how is confirmed by TEM observations.

Therefore measurements on vibrating CNTs can be used to estimate Young's modulus.

The experimental observation of the Young's modulus of a single nanotube is difficult because of its small diameter so a new method, based on the observation of the amplitude of thermal vibration as a function of the temperature, has been employed.

Using the usual Boltzmann distribution of probabilities ($P \propto -E/(k_B T)$), the average of the vibrational energy for a vibrational mode n becomes $\langle W_n \rangle = k_B T$, where k_B is the Boltzmann's constant. The dependence of $\langle W_n \rangle$ on the square of the amplitude u_n^2 is given by

$$\langle W_n \rangle = \frac{1}{2} c_n \langle u_n^2 \rangle = k_B T, \tag{3.28}$$

where c_n is a spring constant, which is related to the amplitude of the thermal vibration by the standard deviation **[52]** :

$$\sigma^2 = k_B T \sum \frac{1}{c_n} \tag{3.29}$$

In simplified continuum model for CNT and in the approximation of simple beam theory for small deformations, the equation which describes the motion for the beam is:

$$\rho A \frac{\partial^2 u}{\partial t^2} + EI \frac{\partial^4 u}{\partial x^4} = q(x), \tag{3.30}$$

where u is the displacement, ρ the density, A the cross-section area, E the Young's modulus, I the moment of inertia and q an applied load. So the natural frequency of the n^{th} vibration mode is described by:

$$\omega_n = \frac{\beta_n^2}{L^2} \sqrt{\frac{EI}{\rho A}}, \tag{3.31}$$

where β_n is the root of an equation obtained through the boundary conditions. The equation for a beam clamped only at one end is

$$\cos\beta_n \cosh\beta_n + 1 = 0\,. \tag{3.32}$$

Form equation (3.29) the relationship between c_n and the young's modulus Y is given by

$$c_n = \frac{\pi\beta_n^4 Y\left(r_o^4 - r_i^4\right)}{16L^3}, \tag{3.33}$$

where the values β_n are solution to the equation (3.32).

By fitting L to equation (3.33) for various nanotubes, the estimated results for Y are found to be in the range of ~ 1000 GPa **[51]**.

The extreme resistance and the high flexibility make nanotubes ideal as reinforcement fibres in composite materials to substitute normal carbon fibres, in spite of their complicate technological creation.

For these properties and for their small dimensions nanotubes could be employed as probe for tunnelling effect microscope (Scannering tunneling) or in the construction of nano-machine. Moreover a group of physicians of Berkley University has obtained a telescopic nanotube taking out MWCNT walls many times and this type of structure could be utilized as "nano-spring" or "nano-shock-absorber" in a car of nanometric dimensions (fig. 3.19).

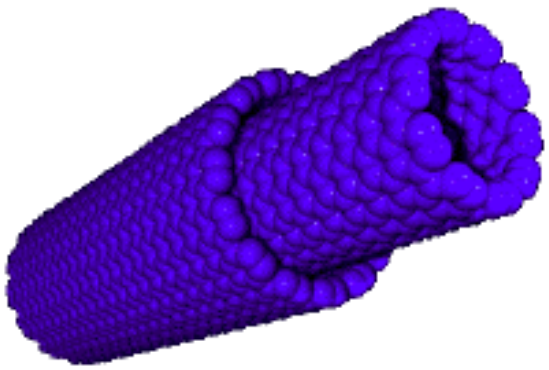

Fig.3.19. "telescopic nanotube"

- **Sensitivity to electric fields**

A further characteristic of these innovative materials is the extreme sensitivity in proximity of intense electric fields.

Many scientists demonstrated that electric field can effectively change the structure and the electronic properties of nanotubes. For example an increase of a transverse electric field can lead the band gap of pristine and defective semiconducting SWCNT to zero.

Recent studies investigated the deformation of armchair single-walled carbon nanotube under transverse electric field, using the density functional theory. An effective change in SWCNTs structure happens when electric fields is high on strength. The results showed that the circular cross-section of SWCNt is changed in an elliptic one; the length of the diameter along field direction increases, while the diameter perpendicular to field direction is reduced. The ratio of the major diameter to the minor diameter of the elliptic cross-section increases with increasing of field strength and nanotube diameter; it gives indication about the deformation degree of structure **[55]**.

Moreover nanotubes react to electric fields flexing themselves to 90^{o} to return in their primal form when the fields is reset to zero. Moreover if the electric fields are oscillating the nanotubes vibrate and monitoring ripple frequency it is possible to take nanotube in resonance. In fact several experimentations have demonstrated that each nanotube is characterized by a specific resonance frequency depending on its length, diameter and morphology. This property could be used for creating "nano-balances".

- **Field emission**

The small dimensions of carbon nanotube diameter play an important role in the field emission: according with this process, a device emits electrons following the application of an electric field.

In the last years several measurements of field emission were effectuated on different nanotube types maintaining both close and open extremity. Closed nanotubes can be "open" applying a strong electric field or treating them with oxygen at high temperatures.

Among the different techniques utilized for this analysis the Bonard's methods consists in the application of MWNT on a gold point , fixing them on a support only by Van der Waal forces.

It is possible to observe field emission applying a potential of about hundred of volts to the gold point; particularly it has been observed that both opened and closed nanotubes can be emit high currents in the order of tenth mA, which correspond to a considerable current density for nanometric objects. Moreover it has been verified that closed nanotubes are more efficient than opened.

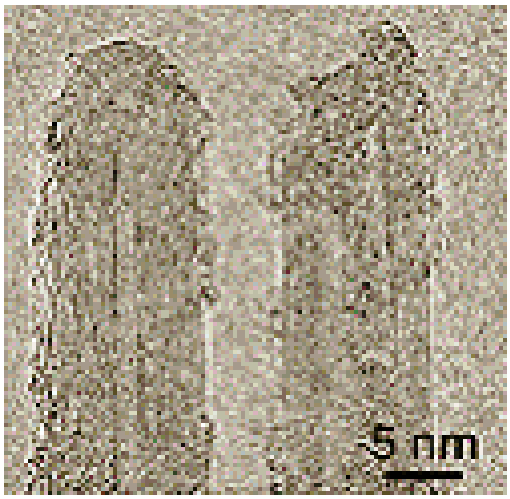

Fig. 3.20. Field emission, respectively, in closed and opened nanotubes.

- **Fluorescence**

When matter is electronically excited by thermal, optical and electrical source, it commonly reacts emitting light. The wavelengths and the strengths of optical transitions reflect the sample's electronic properties. So the luminescence process gives important information about sample's electronic structure through spectral position and intensities and it also permits the qualitative and quantitative analysis of specific substances in complex mixtures.

A team of Rice University, leaded by Richard Smalley (Nobel for the discover of fullerene molecule in 1985) and by the chemist R. Bruce Weisman, discovered that

nanotubes absorb and emit light in near infrared; this property can be useful in biomedical application and in nano-electronics.

This fluorescence was first discovered in aqueous suspensions of SWCNT to investigate the behaviour of an individual nanotube. Measures of intensity emission as function of wavelength and excitation showed a pattern of several peaks representing a specific semiconducting species (*n*,*m*). The spectral distribution provided an important connection between optical transition energies and tube diameter and chiarality. In fact the result showed that optical transition energies are function of nanotube diameter for semiconducting species and that optical transition energies could depend on nanotube environment **[56]**.

The optical spectrum of such a mixture does not present separated transitions for the various species to specific wavelength; it is widely observed, in fact, that SWCNTs spectra are relatively diffuse and uninformative. It happens because of the nanotubes strong tendency to aggregate into bundles bound by Van der Waals interactions.

Nanotube separation from bundles is effectuated by intense ultrasonic agitation and the remaining denser bundled nanotubes were separated by intense ultracentrifugation. These samples show a sharpened absorption spectra and photoluminescence in the near-infrared. The remaining concentration of nanotube bundles in the sample may undergo to two types of electronic perturbations:

- the environment has a polarizability that increases and it varies with position within the bundle; the effect will be a red-shift and a widening of the observed electronic transitions;

- electronic coupling within the bundles may permit the energy transfer from an optically excited nanotube to a neighbour having a smaller band gap; if the accepting species is a metallic nanotube, the fluorescence emission in quenched, while if the acceptor is a semiconducting nanotube with a smaller band gap, the fluorescence emission will be shifted to a long wavelength, that may overcome the limit of detector and may be undetected.

Optical biosensor based on nanotube could be used to detect specific targets in the human body as cancer cells or inflamed tissues. Nanotubes could be covered with a protein able to bind itself only with target cells; since nanotubes are fluorescent only in correspondence of a specific wavelength and nanotubes with different diameters emit different wavelengths, it could be possible to define several typologies of nanotubes to individuate specific targets and to diagnose several diseases in an unique test using a nanotube cocktail.

3.6 Synthesis of Carbon Nanotubes

The first experimental identification of carbon nanotubes was on multi-wall nanotubes in 1991; this discovery stimulated a large number of studies on the single-wall carbon nanotubes, subsequently discovered in 1993. These materials are generally characterized by a very much larger concentration of amorphous carbon, carbon nanoparticles and other carbon-based materials.

Two relatively efficient methods to synthesize single-wall carbon nanotubes are: laser vaporization and carbon arc synthesis an both methods depend on the use of catalitsts.

- **Laser Vaporization Synthesis Method**

The Laser Vaporization of a graphite target is largely used for bundles of single-wall carbon nanotubes with a narrow diameter distribution.

Two sequenced laser pulses were used to evaporate a target containing carbon mixed with a small amount of transition metal from the target (Fig. 3.21).

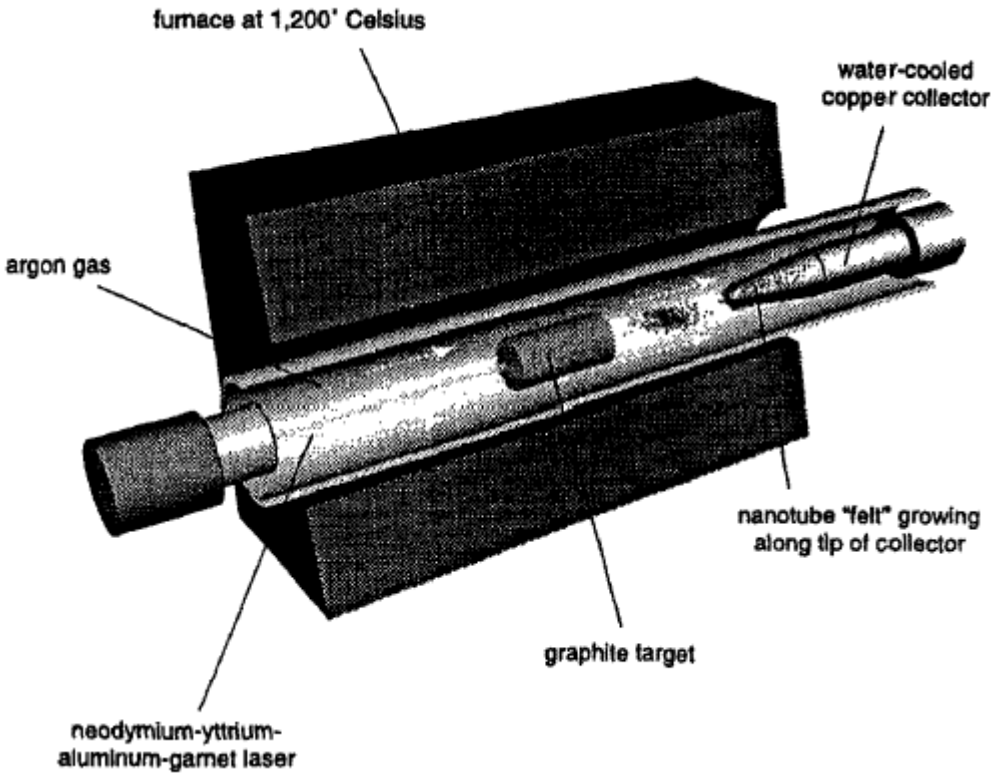

Fig.3.21. Single-walled nanotubes produced in a quartz tube heated to 1200°C by the laser vaporization method, using a graphite target and a cooled collector for nanotubes

Flowing argon gas sweeps the entrained nanotubes from the high temperature zone to the water-cooled Cu collector downstream, just outside the furnace. The material thus produced can be analyzed by scanning electron microscopy (SEM) and transmission electron microscopy (TEM) experiments and X-ray diffraction. So a detailed Transmission Electron Microscopy study **[59]** shows that the diameters of the single-wall nanotubes have a distribution peaked at (1.38±0.02) nm, very close to the diameter of an ideal (10,10) nanotube (see Eq. (3.2)). Moreover the carbon nanotube chiral indices (n,m) are for 44% (10,10) and for 20% (9,9).

The average nanotube diameter and the diameter distribution can be varied by varying the growth temperature and the catalysis composition.

- **Carbon Arc Synthesis Method**

With the carbon arc it is possible to generate the high temperatures needed for the vaporization of carbon atoms into a plasma.

The tools required to use this technique are carbon rod electrodes of (5-20)mm diameter, separated by 1 mm with a voltage of (20-25) V and a dc electric current of (50-120) A flowing through the electrodes; the He pressure is about 500 torr with a flow rate of (5-15) ml/s to cool the system (Fig. 3.22).

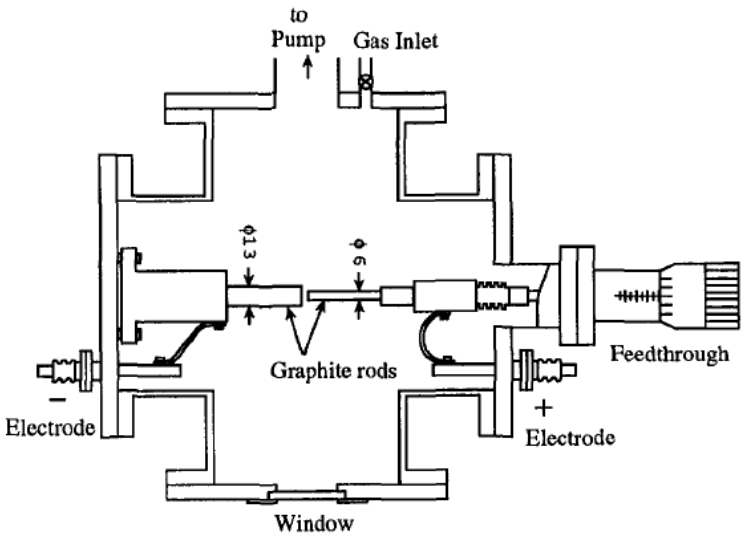

Fig.3.22. Cross-sectional view of a carbon arc generator that can be used to synthesize carbon nanotubes

Once the arc is in operation, a carbon deposit forms on the negative electrode, while the MWCNTs are found in bundles on the inner region of the cathode deposit, where the temperature is maximum ((2500-3000) ^{o}C).

In a vacuum condition, as a consequence of the electric discharge, the temperature considerably increases producing the sublimation of carbon present on the anode, that settles on the reactor walls.

During arc synthesis fullerenes are predominantly found in the soot produced by the arc, while the nanotubes are deposited on the cathode.

The length of a carbon nanotube is typically on the order of 1 μm and the growth rate of a 1 μm carbon nanotube is estimated to be less than 0.1 second, so the time for the growth of a single circumferential carbon ring is about 10^{-5} seconds.

To maximize the nanotube yield in the arc process is important to cool the growth chamber. The principal catalysts used to prepare single-wall carbon nanotubes are transition metals as Co, Ni, and Fe. The iron or cobalt catalysts in the arc process form both single-wall carbon nanotube and nanometer-size carbide particles surrounded by graphene layers, as well as metal clusters encapsulated within graphene layers**[60]**.

Thus purification is necessary to obtain pure single-wall nanotube sample.

- **Other synthesis method**

Another method of nanotube synthesis consists into carbon ion bombardment to make carbon whisker, which is a graphite material with high crystallinity, a diameter in the range of (0.1-1) μm and a length in the order of mm. In this synthesis method, carbon is vaporized in vacuum through ions or electron irradiation; the deposit achieved containing carbon nanotubes is collected on a cold surface.

Some studies reported the use of solar energy for the synthesis of single-wall carbon nanotubes, using an experimental chamber to focuse solar energy to achieve a temperature of 3000 K **[61]**.

Further research is necessary to optimize the synthesis process, increasing the yield of ropes of single-wall carbon nanotubes and minimizing the concentration of residual particles.

3.7 Purification of Carbon Nanotubes

In many of synthesis methods, carbon nanotubes are obtained together with other materials such as amorphous carbon and carbon particles. The purification techniques consist in the isolation of carbon nanotubes from other products of synthesis.

The three main methods used for the purification of nanotubes are: gas phase, liquid phase and intercalation method. Heating may be useful for purification, but it produces an increase in nanotube diameter due to the accretion of epitaxial carbon layers from the carbon in vapour phase, resulting from heating.

The gas phase method removes nanoparticles and amorphous carbon in the presence of nanotubes by an oxidation or oxygen-burn process. The oxidation reaction for carbon nanotubes has an activation energy of 225kJ/mol in air **[62]**, but this process tends to burn off also many nanotubes.

In this process the cap of the nanotubes is burned off first, so the gas phase technique can be a method for tube opening.

The carbon nanotubes obtained through the gas phase purification have diameters in the range of (20-200) Å and a length in the range of 10 nm-1 μm, since the smaller diameter tubes tend to be oxidized with the nanoparticles.

In the liquid phase a potassium permanganate $KMnO_4$ treatment is used which gives yields higher than the gas phase methods, but nanotubes of shorter length.

Chapter 4

Results and discussion

4.1 Thermal Desorption experimental apparatus

The thermal desorption spectroscopy takes place in an ultrahigh vacuum system, equipped with a Quadrupole Mass Spectrometer (QMS), a thermocouple, a close cycled He cold finger, an heater and the gas cylinders.

The ultrahigh vacuum system consists of the pumping system and of the vacuum vessel. Vacuum is maintained through a turbo-molecular pump backed by a rotary dry pump and pressure is about $5x\ 10^{-10}$ torr.

The sample, mounted on the steel head of cold finger ($\approx 30cm^2$), is subjected to gas exposition; gases are introduced in the chamber through a leak valve. The final pressure(p_f) measured during the exposition is due to the base pressure (p_b) and the partial pressure (p_p) of the gas flowing into the system, from which:

$$p_p = p_f - p_b.,$$

where the partial pressure p_p is proportional to the particle numbers (n).

The amount of gas introduced into the UHV system is measured in Langmuir units (1 Langmuir corresponds to a pressure of 10^{-6} torr for 1 s); so different doses are obtained fixing pressure and modifying the time of exposition.

The sample exposition to gas happens at very low temperature (12K-30K), monitored with a Au/0.7%Fe-Chromel thermo couple. Low temperatures of the sample are obtained through a close cycled He cold finger. Thermal desorption is achieved by heating the head of the cold finger with a linear ramp, described by the heating rate β, and the desorbed gas is measured with a quadruple mass analyzer. The heater is formed by a power generator connected to a resistance capsulate in a steel cylinder. The latter warms up for Joule Effect transferring heat to the head of the cold finger and then to the sample previously deposited on its surface. So it is possible to regulate with accuracy the temperature moving away or bringing the cylinder near the sample. In some experiments described in this chapters natural heating is used, obtained turning off the close cycled He cold finger. Using the natural heating temperature increases slower than in the case of heating obtained with a linear ramp.

Temperature is automatically monitored by a computer program. Through a multimeter interfaced to a pc we acquire the voltage at both ends of a thermocouple positioned on the head of the cold finger; the voltage is then converted in the appropriate temperature value by (interpolating the characteristic curve V-T of the thermocouple).

It is possible to choose between the acquisition of a single file ("scanning on" mode) or of many files ("scanning off" mode); in the latter case it is necessary to select the masses to analyze and the total acquisition time. It is important to control that no appreciable contamination gas signals are detected neither in the adsorption nor in the desorption processes.

Each file acquired from the quadrupole during desorption gives the intensity of emission (expressed in arbitrary units) as a function of the atomic number (fig.4.1) (expressed in unit of atomic mass) and the time passed from the begin of acquisition.

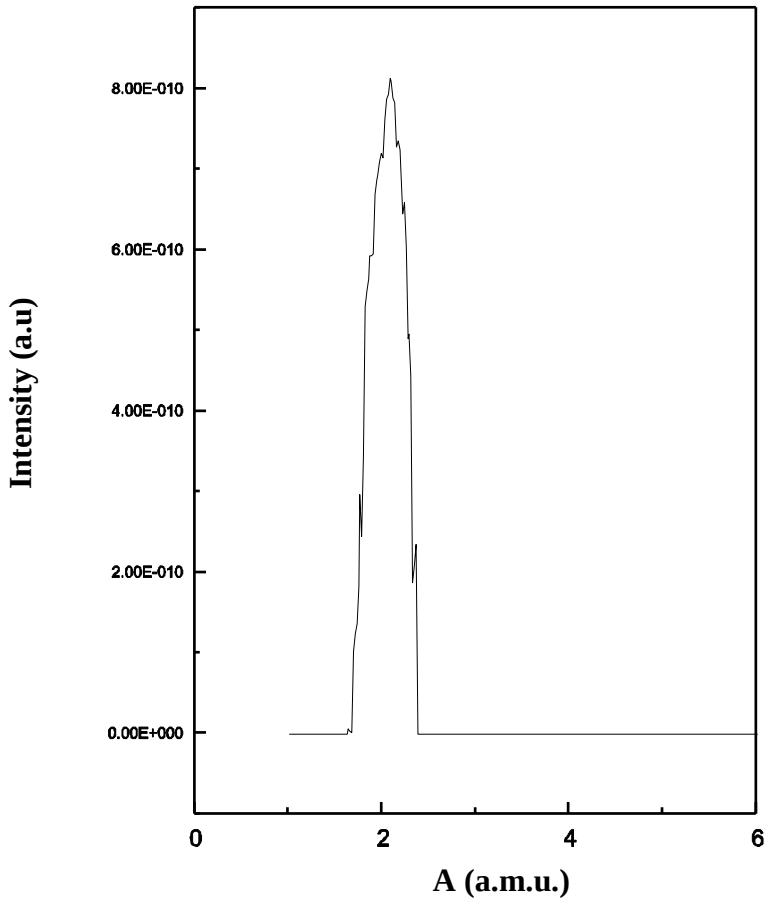

Figure 4.1. Plot of emitted intensity as a function of atomic number A, for the specific case of H_2.

A Gaussian fit gives the area of the curve, that is the value of total emission. This process can be repeated for each file acquired during desorption; then it is possible to create a graph describing the total intensity of emission as function of time for a specific dose.

By a comparison with a temperature file it is possible to obtain a graph of the total emission versus temperature. Calculating areas of these curves for each dose given to system it is possible to build a graph of intensity of emission as function of dose and then to analyze the saturation curve of the system.

For Thermal Desorption Spectroscopy on ammonia and methane, the solid samples are subjected to electron bombardment using an electron gun, with current in the order of μA and the spot size on the sample is about 50 mm^2. The average incident electron energy was chosen in the range 200-3000 eV and the bombardment time ranged between 15 min and 4 h.

4.2 Thermal Desorption Spectroscopy on Carbon Nanotubes

4.2.1 Molecular Hydrogen Desorption on MWCNT

1) Experimental

MWNTs were synthesized by chemical vapor deposition using C_2H_4 and subsequently purified by Prof. Nagy's group of Chemical Engineering Department of Calabria University. As illustrated in Fig.4.15, Transmission Electron Microscopy (TEM) shows that our MWNT sample was made of individual nanotubes with an outer (inner) diameter of 10-15 (3-6) nm and that many of them were open ended. Micro porosity measurements yielded a N_2 BET specific surface of 174 m^2/g. 10 mg of MWNTs were dispersed in ortho-dichlorobenzene and sonicated in a glass container. The sample then was deposited directly onto the steel head (6 cm^2) of a cold finger with closed He cycling and dried. A quite uniform thin film was obtained and its adhesion to the copper surface remained stable during all the measurements. The experiments were conducted in a UHV chamber (base pressure in the low 10^{-9} Torr range) evacuated with a dry turbo pump. H_2 gas (purity of 99.999%) was introduced in the chamber through a precision leak valve while keeping the sample at a desired adsorption temperature T_{ad} and a fixed pressure of $2x10^{-5}$ Torr (corrected for the ion gauge sensitivity factor) for a chosen time interval, then the gas was pumped out. The sample temperature was monitored with a Au/0.7%Fe-Chromel thermo couple. Thermal desorption was achieved by heating the head of the cold finger with a linear ramp and the desorbed H_2 was measured with a quadruple mass analyzer. No appreciable contamination gas signals were detected neither in the adsorption nor in the desorption processes. Complete reversibility of charging and discharging cycles was routinely verified and a total reproducibility was observed.

The vacuum system pumping speed was calibrated by admitting a known quantity of hydrogen into the chamber at desired quadruple reading pressures and monitoring the time needed for evacuation. A linear dependence on the pressure was observed. The desorption rate was obtained by multiplying the detected hydrogen partial pressure (the integral intensity of a quadruple mass spectrum centered at $m = 2\ a.u.$ composed of some 50 data points) by the system pumping speed and the total amount of desorbed hydrogen then could be evaluated from the integration of the desorption rate-time curves with an estimated error of about 20%. It was devaluated the dependence of emission intensity on several experimental parameters:

1) exposed mass sample:

The experiment was effectuated deposing every time a different mass amount of the same sample on the cryostat head to show emission dependence on the mass subjected to exposition. It was also determined for each mass the dose corresponding to saturation and the consequent emitted intensity to choose the correct mass range to analyze.

2) H_2 dose:

The sample was subjected to gaseous hydrogen in different doses. From the analysis of intensity as function of dose it was possible to observe the saturation curve to choose H_2 dose distant from saturation levels.

3)Exposure temperature:

Exposure temperature was controlled using a power generator connected with a heating steel small cylinder in contact with cryostat. Varying the heater power it was possible to vary the system temperature.

4) amount of covered surface:

The exposure was made in two ways: the sample was deposed on the cryostat head (with an occupied surface of 6,28 mm^2) or on the lateral walls of cylinder. So it was possible to evaluate the existence of the desorption dependence on the amount of covered surface.

5) heating rate, β:

Different heating rates were obtained controlling the power generator. From determination of the temperature corresponding to maximum peak it was possible to verify if H_2 desorption is characterized by a first kinetic order, described by a linear dependence of $\ln\left(\frac{T_m^2}{\beta}\right)$ on $\frac{1}{T_m}$.

2) Results and Discussion

Below the experimental results obtained from analysis of several parameter are shown.

a) Study in function of sample mass

Increasing the mass subjected to exposure the number of available sites increases, so the adsorption probability. To this phenomenon corresponds a greater amount of accumulated gas and increasing re-emission values (fig. 4.2).

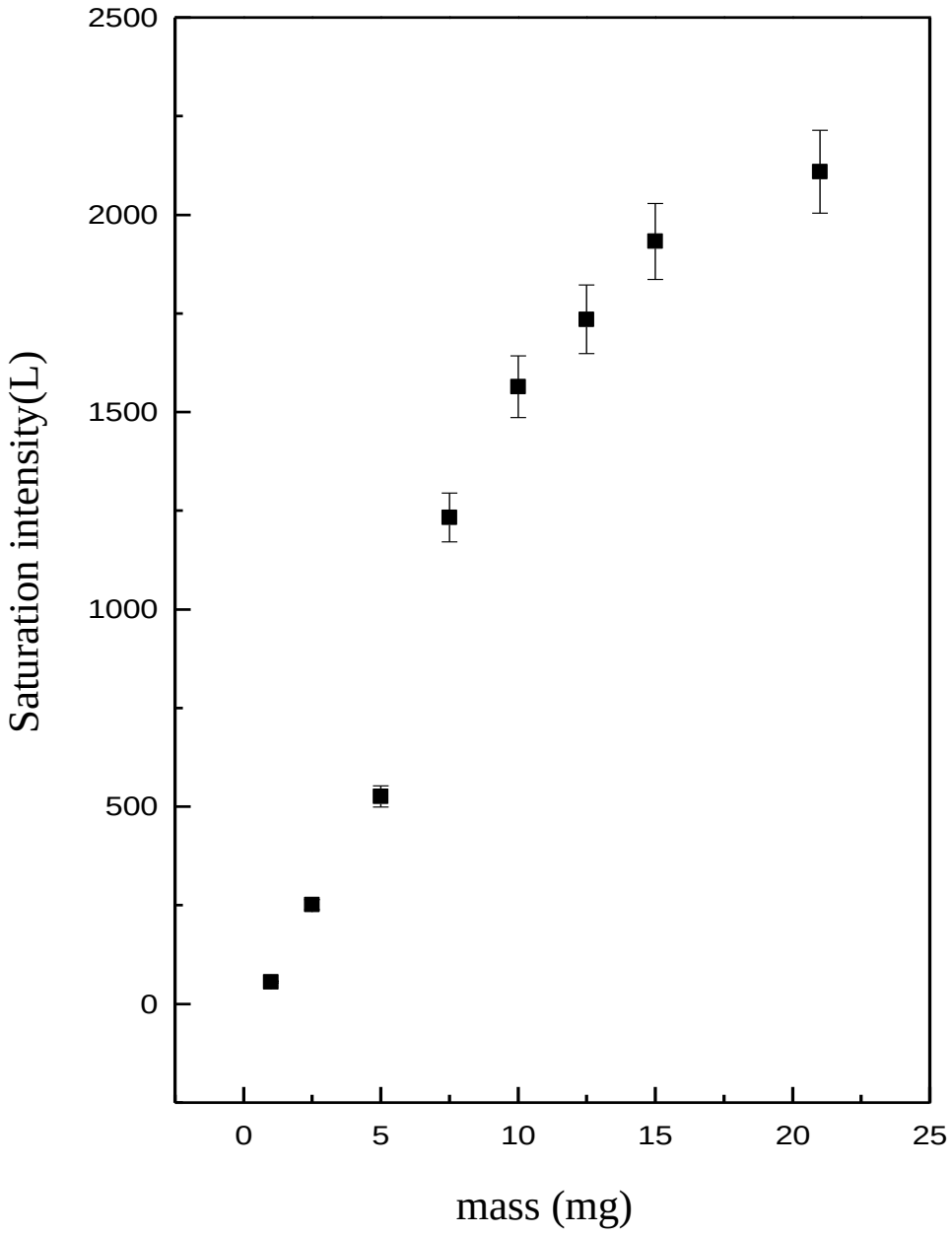

Fig. 4.2. Saturation intensity as a function of sample mass

To great masses corresponds an increase of the gas storing capacity of sample, so greater molecular hydrogen amounts are adsorbed by the sample (fig.4.3).

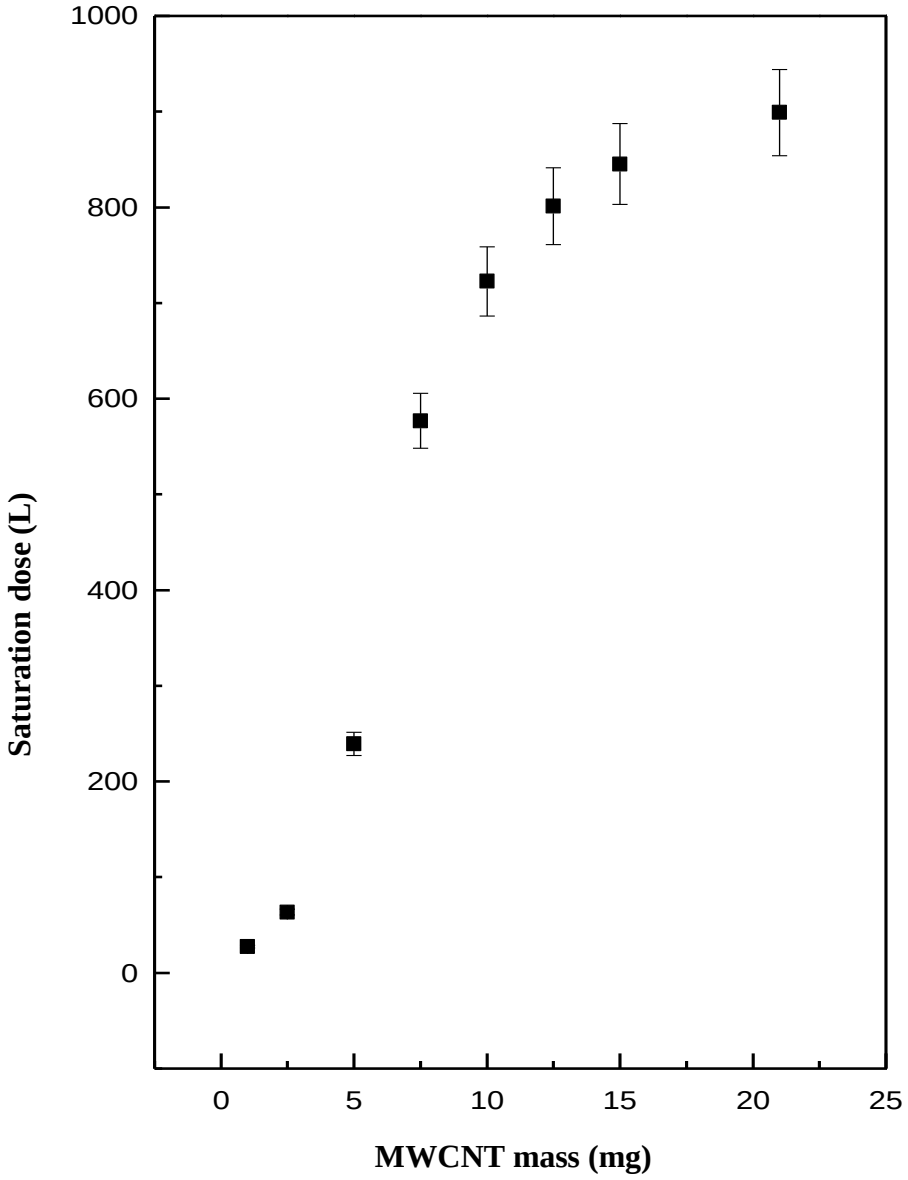

Fig. 4.3. Saturation doses as a function of several masses of the same sample

b) Study in function of the covered surface

Figure 4.4 shows the trend of emission as a function of gas dose. Data in black correspond to the MWCNT dusts deposition on the entire cryostat head (with a surface of 6,28 mm^2), while for red data the sample was deposited also on lateral walls of cylinder. The two trends are

almost identical and it confirms that the emission intensity does not depend on the sample deposition modality and that desorption is not a surface phenomenon.

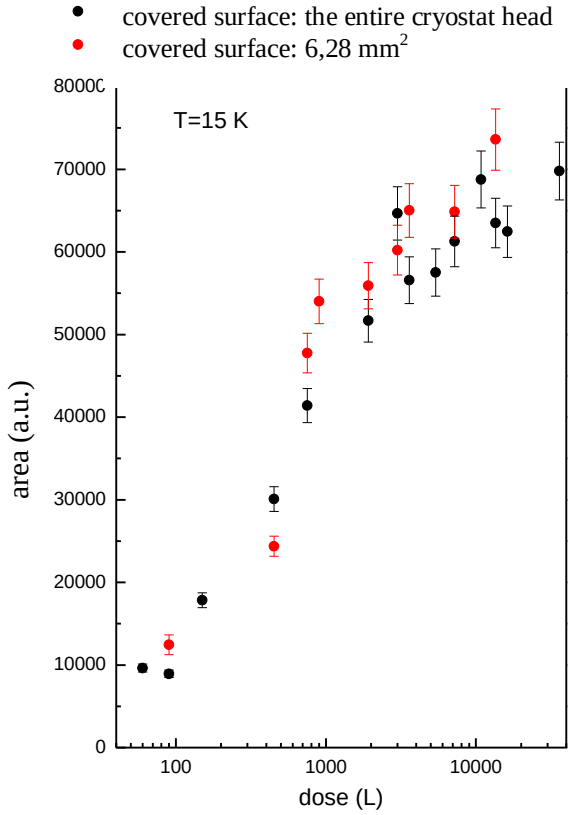

Fig. 4.4. Emission intensity as a function of H_2 dose for two different deposition modalities at $T_{ads=}$15 K.

c) Comparison with charcoal

The same experimental procedure was repeated for charcoal. Figure 4.5 shows a comparison between the emission intensity as a function of H_2 dose for the two different samples, with fixed heating rate, covered surface and deposition temperature. It was also analysed the emission by experimental setup, before any sample deposition.

In figure 4.5 it is presented the total H_2 adsorption amount of 10 mg activated charcoal powders (N_2 BET specific surface area 23 m^2/g) under exactly the same experimental conditions. It exhibits very similar characteristics as that of MWNTs but is about five times smaller. It is possible to note that the experimental setup contribute is negligible.

So carbon nanotubes have an adsorption efficiency much greater than other carbon-based materials so they may be good candidates as cryosorbers in future accelerators.

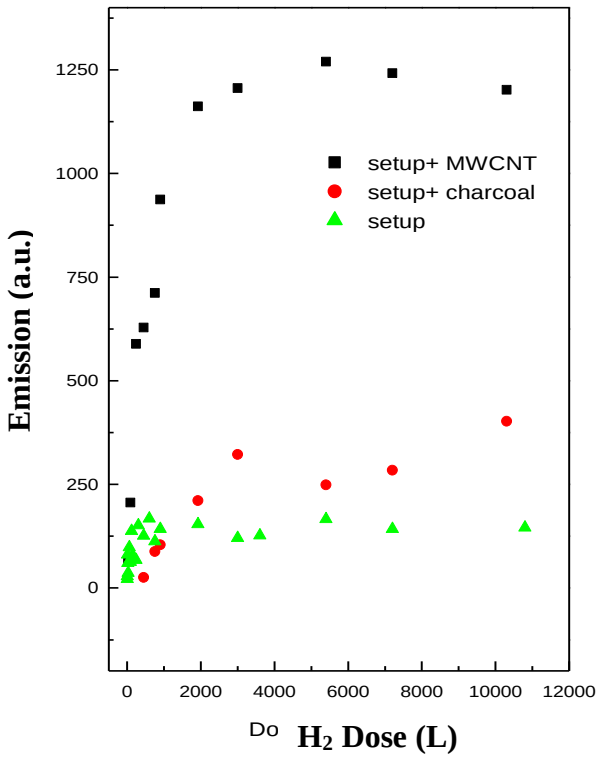

Fig.4.5. Trend of emission as a function of H_2 exposed dose for two different samples: black, MWCNT; red,charcoal; green, experimental setup with no sample (background)

d) <u>Study in function of exposure time</u>

In Fig 4.6 we illustrate some representative H_2 TPD traces taken at a constant adsorption temperature of $T_{ad} = 15K$ and varying exposure time. The H_2 dose Φ was expressed in units of Langmuir (1 L = 10^{-6} Torr sec) and the sample heating rate was fixed at $\beta = 5K/min$.

These spectra are substantially narrower than those previously reported in literature for H_2 dosing at higher temperatures and pressures **[58]**,**[63]** .

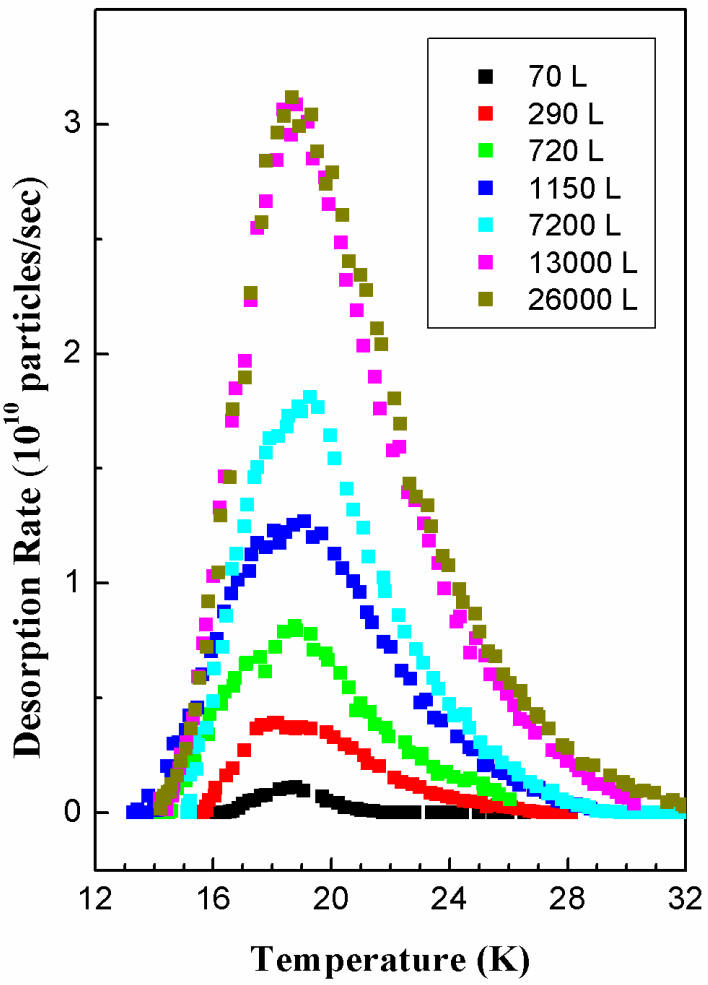

Fig.4.6. Temperature Programmed Desorption traces of molecular hydrogen adsorbed at $T_{ad} = 15\ K$ and P_{ad}=2x10^{-5} Torr. The dose is expressed in Langmuir (1L =10^{6} Torr sec).

It is possible to note that each curve is peaked around 20 K; increasing the coverage, so the gas dose, the maximum peak temperature remains constant for curves with the same exposure temperature.

These TPD traces are quite similar to each other and the spectrum maxima remain unchanged as the hydrogen adsorption increases clearly indicating a first order desorption mechanism (see chapter 1). In fact a first kinetic -order is described by the following characteristics:

- Desorption rate is directly proportional to coverage.
- When coverage increases the temperature of maximum peak does not vary .
- The peak is asymmetrical.

Our result reflect all these characteristics, so H_2 adsorption on MWCNT is described by a first kinetic -order.

Through a comparison between curves obtained for several doses (fig. 4.7), it is clear that the curves area increases with the increase of hydrogen dose because of adsorbed gas and so re-emitted gas increase.

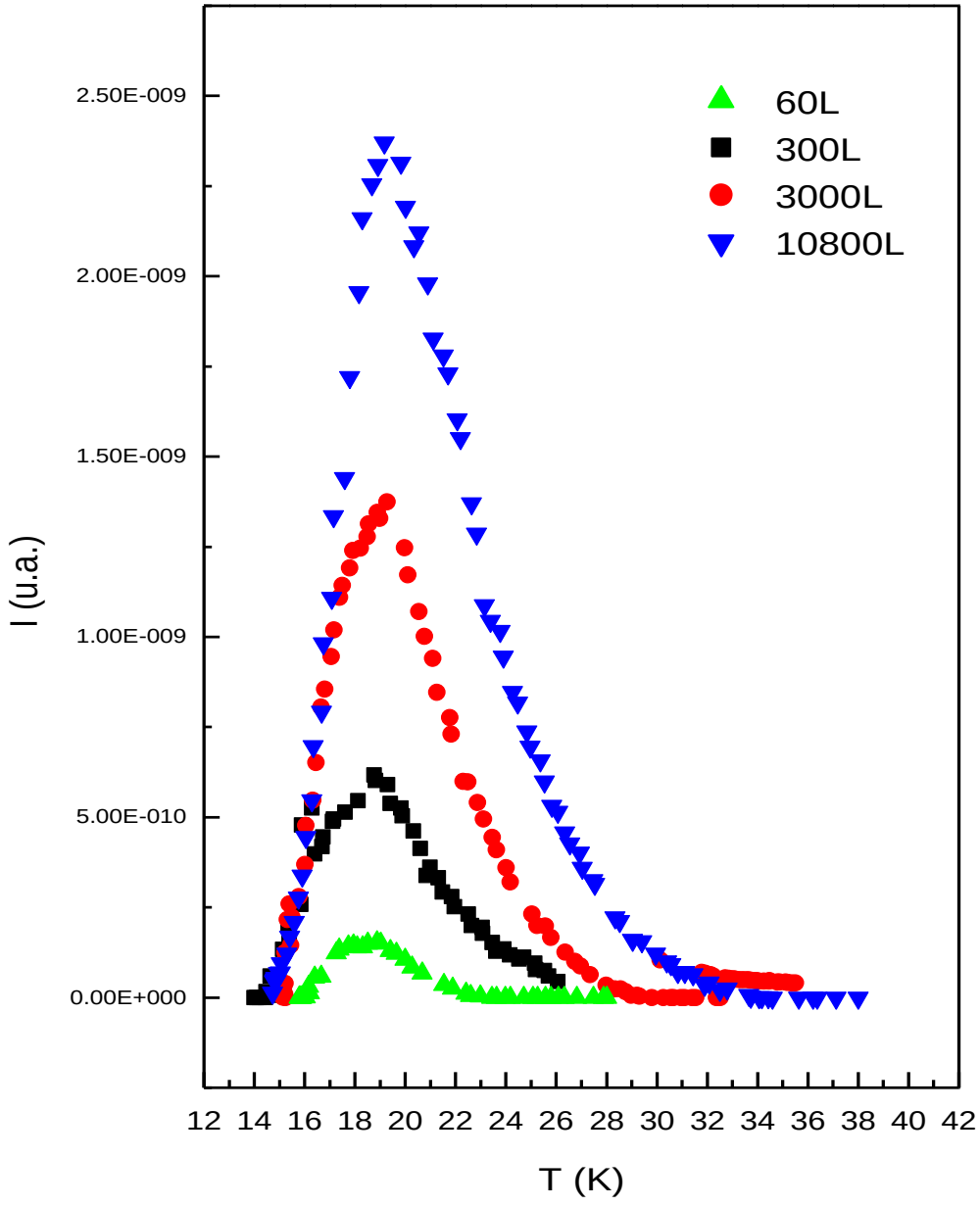

Fig. 4.7. Detail of emission trend as a function of temperature for different gas doses

Beyond a dose specific value the system cannot be able to adsorb further gas amount, because the adsorption sites are totally occupied; the system cannot adsorb any more molecular hydrogen and it saturates, as it is possible to note from constant emission trend for H_2 doses higher than 1000 L (Fig. 4.8).

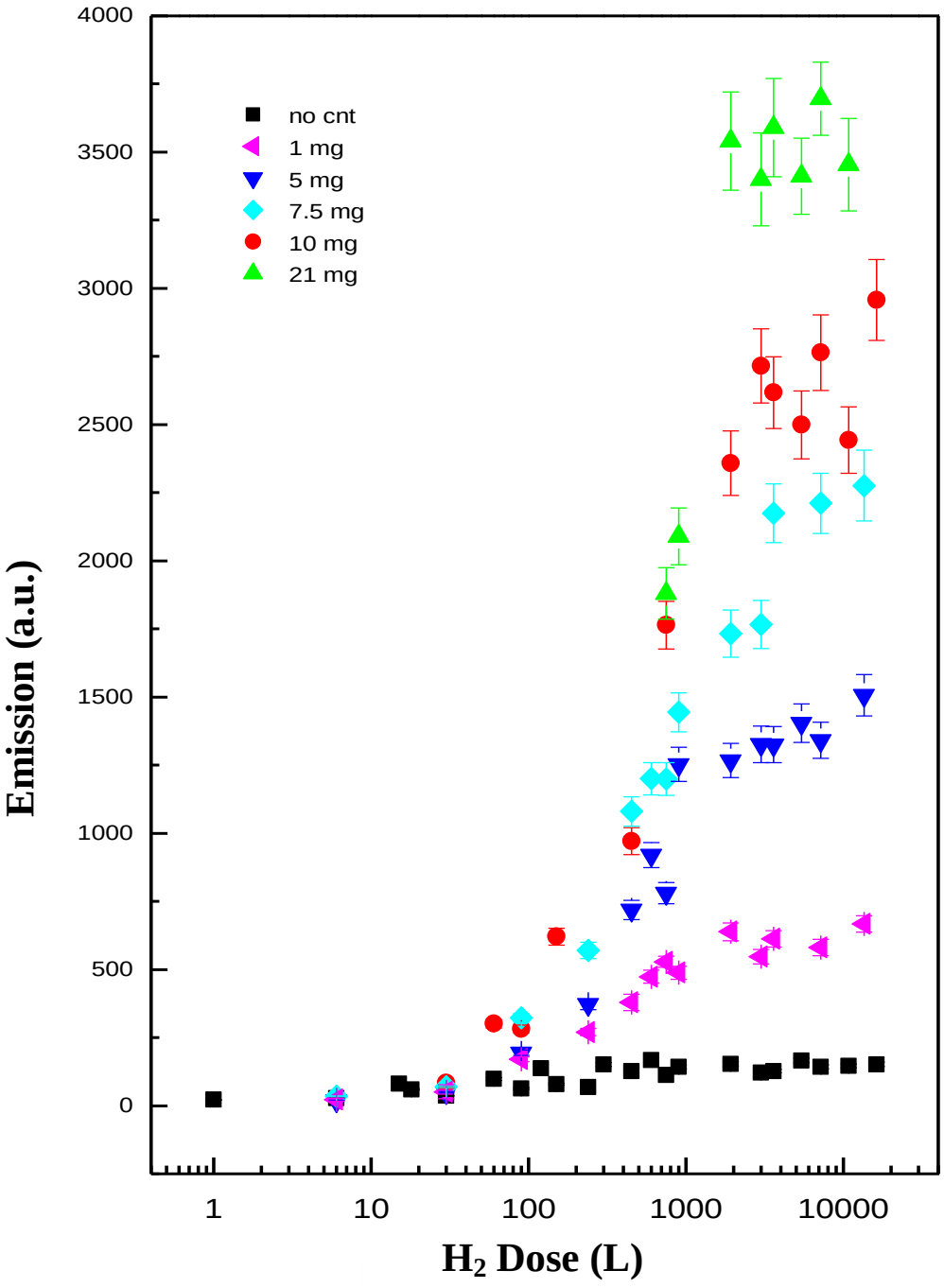

Fig. 4.8. Trend of emitted H_2 as a function of exposure dose for different masses

The total molecular hydrogen content, as determined from the integral of the desorbed H_2 TPD trace curves, is plotted in Fig. 4.9 as a function of Φ for $T_{ad} = 15K$. It is interesting to note that it increases linearly with Φ at low doses and saturates at about $8x10^{-8}$ wt.% for $\Phi \geq 10^4\ L$. The saturation at a very low value and the relatively narrow line shape would suggest that hydrogen adsorbs only on a limited number of sites. Beyond a specific value of dose the system cannot be able to adsorb further gas amount, because the adsorption sites are totally occupied.

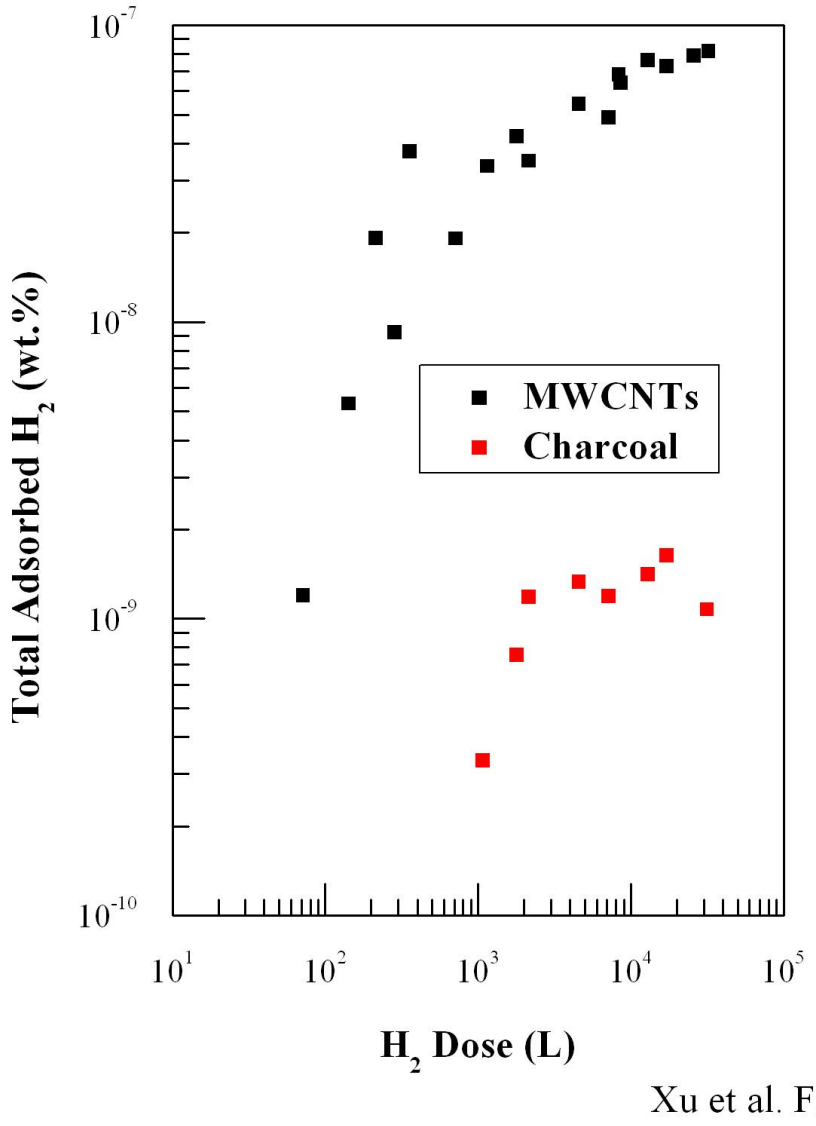

Fig.4.9. Molecular hydrogen adsorbed on MWCNTs as a function of H_2 dose for adsorption temperature of $T_{ad} = 15\ K$. Also shown are the results for a charcoal sample. The active surfaces are 174 m^2/g and 23 m^2/g for MWCNTs and charcoal, respectively

e) Study on function of heating rate

To analyze the desorption phenomenon in function of the heating rate a power generator was used to modify the sample temperature. The temperature obtained was analyzed as a function of time to verify a temperature linear dependence on time, obtained through our experimental instruments. So the heating rate β is represented by the slope of the straight line, as showed in figure 4.10, where β have the specific value of 0.08 K/sec.

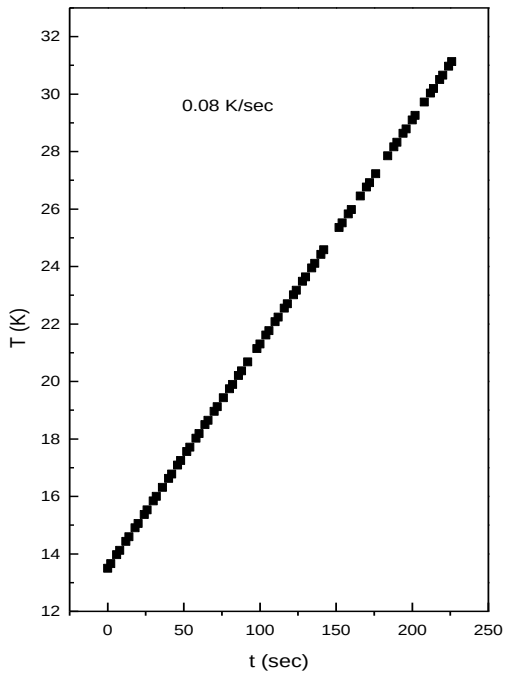

Fig. 4.10. Temperature as a function of time: the heating rate is the slope of straight line

We also verified if the Polanyi-Wigner equation for first kinetic-order (eq.(1.52)), obtained rearranging Polanyi-Wigner equation

$$\ln\frac{T_{\max}^2}{\beta} = \frac{\Delta E_{des}}{RT_{\max}} + \ln\frac{\Delta E_{des}}{\nu_1 \cdot R},$$

is confirmed by our experimental results.

In fact plotting $\ln(T_{max}^2/\beta)$ versus ${T_{max}}^{-1}$ it is possible to note a linear trend which reflects the equation for first kinetic-order

To gain some information on the hydrogen binding energy the sample heating rate β has been varied for constant coverage $\Phi = 2100\ L$ and $T_{ad} = 19\ K$.

Plotting $T_{\max}^2/\beta$ as a function of $1/T_{\max}$ the binding energy may be determined from the slope of the straight line ($\Delta E_{des}/R$).

In table 4.1 the values of the heating rate used and the temperatures of maximum peak are reported:

β (K/min)	T_{max}
1.512	21.2
2.262	21.89
3	22.45
4.62	22.71
5.16	22.87
7.14	23.1
7.5	23.3
10.74	23.9
12.6	24.1
14.94	24.42

Table 4.1

In Fig. 4.11 we plotted $\ln(T_{max}^2/\beta)$ versus ${T_{max}}^{-1}$ where T_{max} is the temperature corresponding to the desorption rate maximum

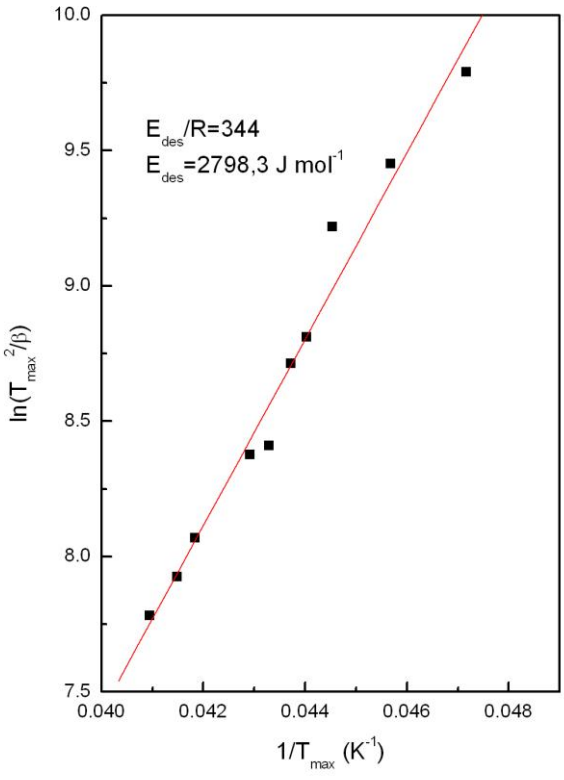

Fig.4.11. Plot of $\ln(T_{max}^2/\beta)$ versus ${T_{max}}^{-1}$ for a series of TPD spectra taken at fixed $T_{ad} = 19\ K, \Phi = 2160\ L$ and varying heating rate β. T_{max} is the temperature corresponding to the desorption rate maximum.

The slope of the linear fit yields a desorption energy of $E_{des} = 340 \pm 20K$ (or $E_{des} = 2.82 \pm 0.16\ KJ/mol$). The theoretic desorption energy for nanotubes is in the range 1kJ/mol ÷9 kJ/mol .

It is interesting to note that though there is a large body of experimental studies on hydrogen adsorption on carbon nanotubes because of its potential application as a storage material, very few measurements were undertaken below 77 K **[64],[65]**. To the best of our knowledge, no experimental data are available in literature for adsorption at very low pressures. The binding energy value found in this study is lower than that for H_2 on graphite (480 K) **[66]** in accord with the isothermal adsorption measurements reported by Wilson *et al.* (3.3 kJ/mol) **[64]**. This suggests that hydrogen molecules mostly adsorb on the outer surfaces and the reduction in binding energy value is generally attributed to the surface curvature **[67]**, **[68]**.

f) Study in function of exposure temperature

Figure 4.12 shows that H_2 intensity emitted by the sample varies with temperature, for several exposure temperatures.

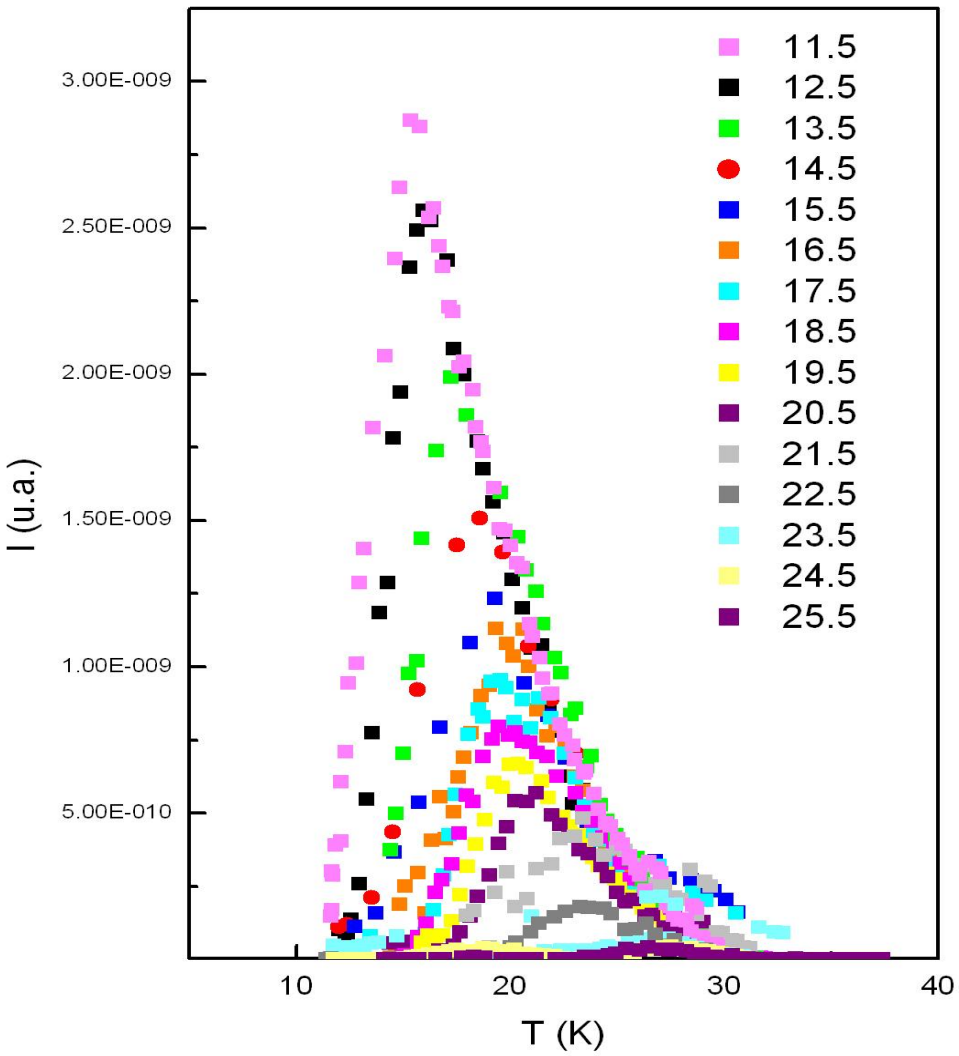

Fig.4.12. H_2 emitted as a function of temperature for exposure temperatures in the range (12.5 K÷25.5K)

Low intensity corresponds to exposure temperatures higher than 25 K. There is a specific energetic distribution of sites and when exposure temperature increases the number of sites

with low dissociation energies decreases. For low exposure temperatures there is a low dissociation energy and a great number of sites characterized by low dissociation energies. As showed by fig. 4.12 each curve has a temperature of maximum peak similar to its exposure temperature.

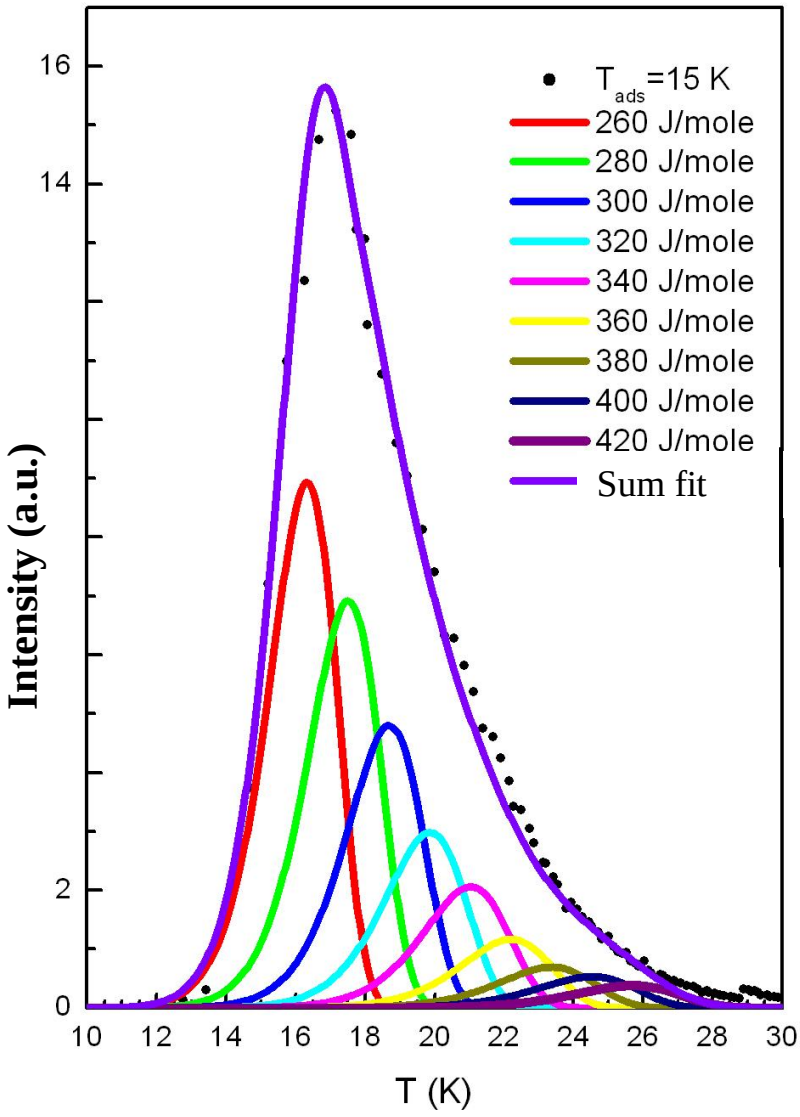

Fig.4.13. Emission intensity as a function of temperature; comparison between plots obtained by Polanyi-Wigner equation and experimental results for several desorption energies, with β fixed.

Figure 4.13 shows a comparison between plots obtained by Polanyi-Wigner equation, calculated for several energies (to each energy corresponds a particular portion of sites and the energetic distribution is continuous) and experimental results for a specific exposure temperature and for all sites characterized by higher energies, with β fixed. In fact, to each exposure temperature corresponds an activation energy so a specific number of adsorption sites. For low energies the number of adsorption sites is bigger than for high energies, therefore emission intensity is great for low temperature.

Plot in figure 4.13 (violet line) corresponds to the superimposition of curves with several desorption energies calculated regarding portion of sites characteristic of each energy. The trend is asymmetric and the resulting curve shows a broadening of the shape at right of the peak, contrary to the single curves. The plot peak is translated of some Kelvin respect to exposure temperature. From a comparison between plot and experimental data it is clear that the two trends are completely coherent, with a net superimposition of tails. Also the experimental curve presents an asymmetric trend and a peak shift respect to exposure temperature.

Then the theoretic method used in this work has a good experimental verify.

Finally, in Fig. 4.14 we illustrate the saturated total amount of adsorbed hydrogen as a function of adsorption temperature T_{ad}.

This figure confirms the inverse proportionality between emission intensity and adsorption temperature. As expected, the total hydrogen adsorption capacity decreases with the adsorption temperature. For $T_{ad} \geq 27\ K$, no H_2 adsorption is observed.

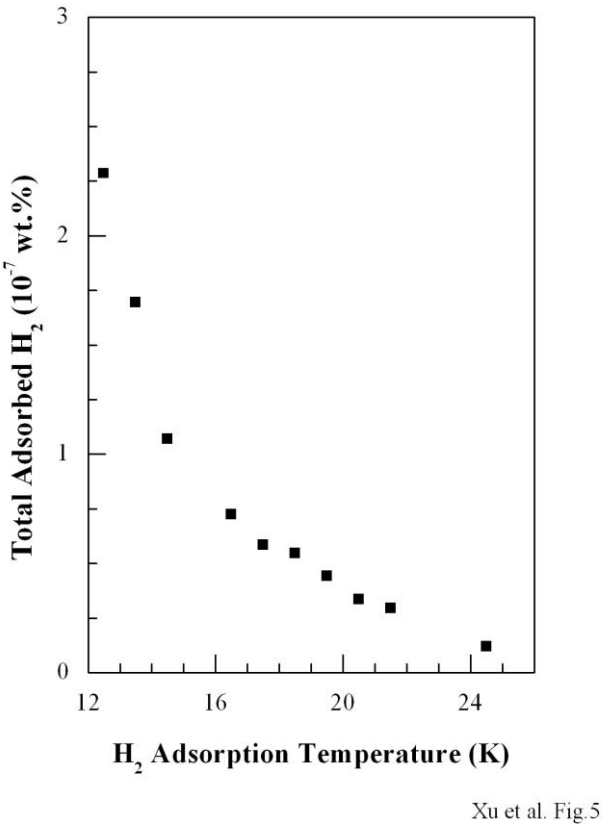

Fig.4.14. Saturated molecular hydrogen content adsorbed on MWCNTs as a function of adsorption temperature of T_{ad}.

This site assignment is in accord with the TEM observation that our sample was essentially made of individual nanotubes (Fig. 4.15). On the other hand, adsorption on inner walls would imply a much stronger bonding **[64], [69]** and diffusion into those open ended nanotubes. Quasi elastic neutron scattering measurements performed by Narehood *et al.* also indicate the absence of H_2 mobility in SWNTs at temperatures below 30 K **[70]**.

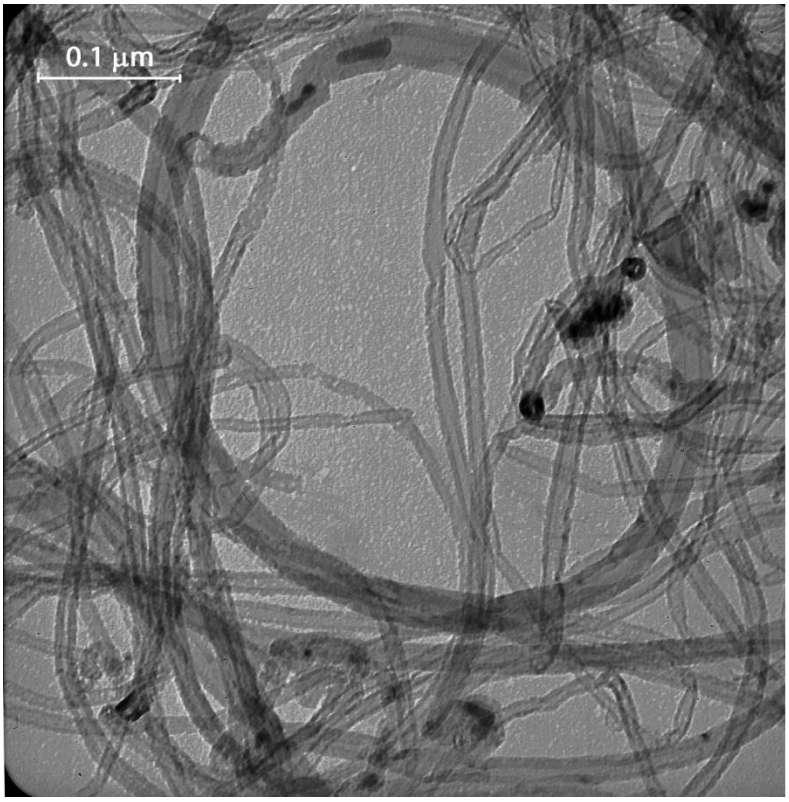

Fig. 4.15. Transmission electron micrograph of multi-walled carbon nanotubes sample used in this study.

3) Conclusions

Our results contrast sharply with those reported for hydrogen storage measurements at higher temperatures and pressures and strongly indicate that, under high vacuum conditions, hydrogen do not adsorb on the nanotube surface beyond the sublimation temperature and the diffusion is essentially inhibited, as already confirmed by previous works. More quantitative works are currently being undertaken to determine the realistic possibility of using nanotubes as cryosorbers in UHV systems.

In conclusion, we presented first experimental measurements of molecular hydrogen adsorption on MWNTs in real cryopumping conditions of accelerators at low pressures (10^{-5} Torr) and low temperatures (12-30 K). We showed that the adsorption capacity decreases sharply with temperature and is in the order of 10^{-7} wt. % at 12 K. This behaviour is about an order of magnitude higher than that obtained for commercial active carbon making MWNTs a potential candidate as cryosorbent materials for accelerators.

4.2.2 Krypton adsorption on SWCNT

1) Experimental

In this work we present some primary results of a TPD study about Kr adsorption on single walled carbon nanotubes (SWNT) at very low pressure and temperatures as a function of coverage. Different doses of Kr gas were introduced into the vacuum chamber through a leak valve keeping pressure value about 10^{-8} Torr and varying exposure time. We used the same procedure of the TPD experiment on H_2 described in the previous paragraph. Recently, experimental studies of krypton adsorption on single walled carbon nanotubes (SWNT) have appeared in literature **[71]**.

2) Results and Discussion

Fig. 4.16 shows a typical TPD spectra for Kr dose about 45 L at an adsorption temperature of 30 K.

Varying the heating rate (from 3K/min to 27 K/min) the peak temperature at maximum is about 47 K for each curve, because exposure temperature is constant. This result confirms that this process is described by a zero order kinetic.

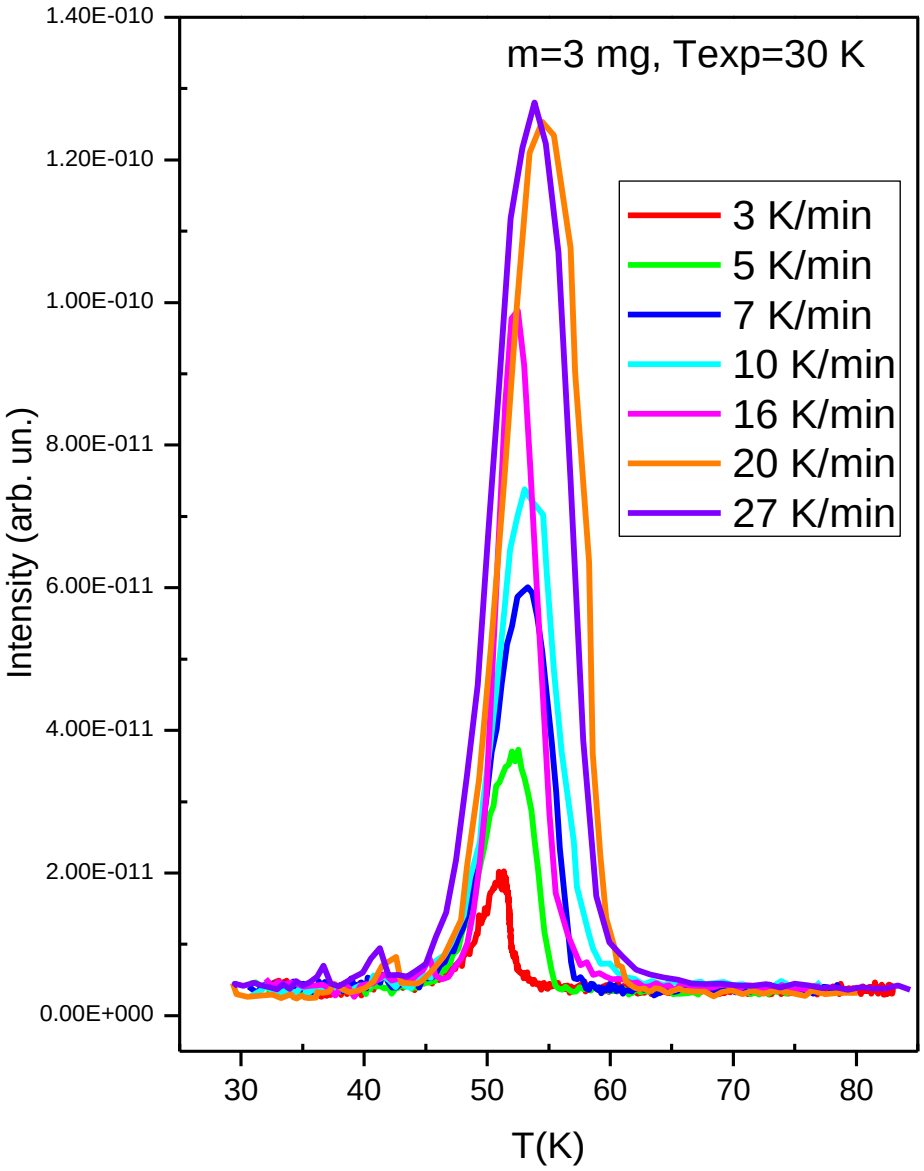

Fig. 4.16. A typical TPD spectra for Kr dose about 45 L at an adsorption temperature of 30 K.

In Fig. 4.17 we illustrate typical TPD spectra for Kr gas on SWCNT, obtained varying the exposure time from 10 s to 3000s at an adsorption temperature of 34 K.

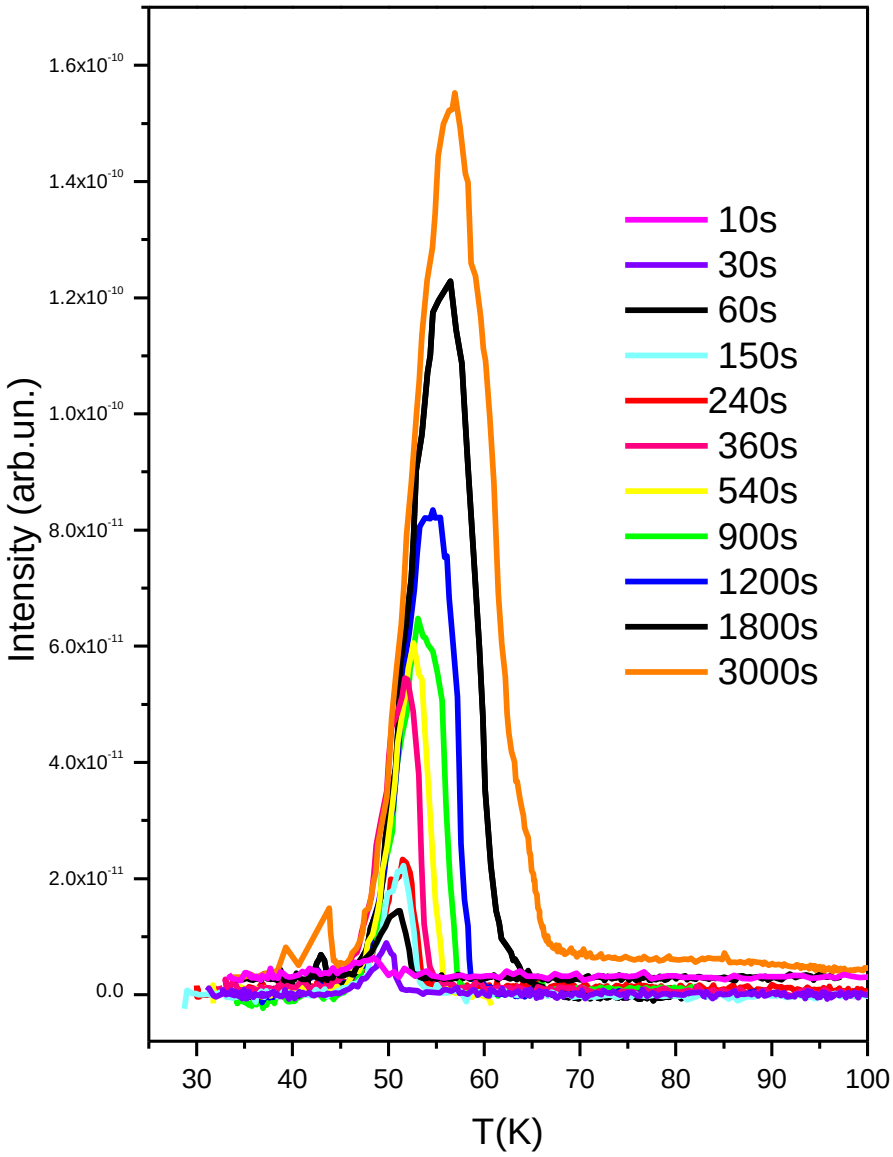

Fig.4.17. A typical TPD spectra for Kr, obtained varying the exposure time from 10 s to 3000s at an adsorption temperature of 34 K.

Each data point in the figure actually is an integral QMS intensity at atomic mass units 85 and is proportional to the desorption rate. The intensity of gas emitted is proportional to Krypton uptake and the peak temperature at maximum move to high temperature increasing gas dose. It shows that krypton adsorption is described by zero order kinetics (see chapter 1).

3)Conclusions

Our results confirm that carbon nanotubes are good gas absorber according with works in literature, but the originality is that our measures were effectuated under high vacuum conditions and for T_{ad} below the liquid nitrogen temperature (77K). So we confirmed the realistic possibility of using carbon nanotubes as cryosorbers, also for noble gases.

4.3Thermal Desorption Spectroscopy in Astrophysics

4.3.1 Thermal Desorption Spectroscopy of solid ammonia

Volatile species which can freeze out from the gas phase at temperatures below 273 K are usually referred in astrophysics as "ices". Ices are present in the Solar Systems, on the comets and in the interstellar medium (here ISM for brevity), where they form, in regions where the temperatures are ≈10 K for both the gas phase and the solid component, the so-called "mantle" of the dust grains **[20]**. In these environments ices are subject to chemical and physical processes, specifically they are subject to bombardment of photons and cosmic rays. As a consequence some species evaporate, bonds breaking and radical formation occurs, new species can form; in a word a rich radiation astrochemistry occurs. The effects of ice bombardment were intensively studied experimentally, mainly ion irradiation **[34]** and photon irradiation **[35]**, but also electron bombardment is important **[51]**. For this reason we started an experimental research program at the Surface Physics Laboratory of the University of Calabria with the aim to study the effects of electron bombardment on ices of astrophysical interests. Here we report specifically on the effects induced by electrons, with energy ranging from a few hundreds eV up to 2000 eV, on a bulk of ammonia adsorbed on a cold substrate. Interstellar ices are mainly composed of H_2O, CO, CO_2, CH_3OH, CH_4, NH_3 **[72.]**. Ammonia is present with an abundance of 1%-10% with respect to water **[73]**. It is also present in the atmosphere of the external planets of the Solar System and on the surface of their icy satellites **[51]**. In order to "isolate" the effects on a pure ice we decided to use a pure ammonia ice in our experiments, irradiation of ice mixtures is planned as a future improvement of our study.

Let's now briefly discuss what should be expected from the interaction between ammonia and electrons. Let's start discussing of the effects of the electrons on gas phase ammonia; effects on condensed ammonia will be discussed later, preliminarily in this introduction and more in depth in the following pages. Frost et al. **[97]** report ionization potentials 10.35 eV and 14.95 eV. Then few tents eV electrons should at least ionize ammonia molecules. As a matter of fact ammonia is dissociated by the electrons of a quadrupole mass spectrometer (in our case the energy of electrons is about 60 eV); the AVS Reference Guide (on the web **[74]**) reports the following mass spectra due to the cracking fraction of NH_3 (in parentheses the relative abundance): mass 17, NH_3 (100), mass 16, NH_2 (80), mass 15, NH (8), mass 14, N (2).

One of the oldest experimental works on the ionization and dissociation of ammonia by electron impact is reported by Mann et al. **[96]**. Dissociation of ammonia by electron impact

has been reported by Bubert and Froben (1970) **[75]**. Tokue and Iwai (1980) **[76]** report formation of NH(A $^3\Pi$) and NH(c 1Π) by electron impact dissociation of ammonia. Fragmentation of NH_3 dimers and of size selected NH_3 clusters by electron impact ionization has been reported by Buck and coworkers (**[77]**,**[78]**). The electron impact dissociation of the NH_3 molecule has also been experimentally investigated by Muller and Schulz (**[79]-[81]**)**.** Sato et al. **[82]** measured absolute emission cross sections of fragments produced by impact on NH_3 by electron with energy below 100 eV. Absolute partial and total cross sections for electron impact ionization of ammonia are reported by Rejoub et al. **[83]**, up to 1 keV. The translational energy distributions of H^* (n=3,4) produced in collisions between electrons and ammonia were determined experimentally by Kurawaki and Ogawa **[84]**. Experiments on solid ammonia are reported by Zheng et al. **[37]**.

1) Experimental

Our experiments were performed in a Ultra High Vacuum (UHV) Chamber equipped with an electron gun, a quadrupole mass spectrometer and a closed cycle liquid helium refrigeration system. The base pressure in the chamber was in the low 10^{-10} Torr range and it was obtained using a dry turbo pump. At the steel head of the cold finger we were able to reach temperatures around 20 K. The sample temperature was monitored with a Chromel-AuFe (0.07%) thermocouple. Heating was obtained by simply turning off the refrigeration system. NH_3 gas (purity of 99.999%) was introduced in the UHV chamber through a precision leak valve and dosed through a 2 mm diameter Cu tube, the end of which was reproducibly positioned 1 mm away from the steel surface. With this technique we were able to condense most of ammonia on the surface of the cold finger. We checked accurately the reproducibility of the deposition. Different doses of ammonia were obtained varying the time interval during which we kept open the leak valve. No appreciable contamination of NH_3 was detected. The UHV chamber was outgassed and the tube, used to deposit ammonia, accurately purged before each set of experiments. The beam current of our electron gun was of the order of 1 μA, the spot size on the sample was of about 50 mm^2. In our experiments we used different incident electron energies, ranging from 200 eV to 3 keV, and irradiation times of several minutes. We checked the content of the NH_3 bottle by simply pumping in the chamber the gas and analyzing the partial pressure by using the quadrupole; in this way we also obtained the cracking fraction of ammonia. The results of the interaction of electrons with the condensed

ice were investigated by using the Thermal Desorption Spectroscopy (TDS): the bulk obtained by deposition is irradiated with an electron beam, then the processed ice is left to desorb by increasing naturally the temperature of the cold finger and the gas content of the chamber is monitored as a function of the temperature by means of mass spectrometry. As a reference we acquired a TDS spectrum of an ammonia bulk not irradiated with electrons (we called this a "no irradiation experiment"). A TDS spectrum was also acquired in which we didn't neither deposit NH_3 nor irradiate with electrons and simply we raised the temperature of the cold finger (we called this a "blank experiment").

2)Results and Discussion

In figure 4.18 we show a typical mass spectrum obtained raising the temperature after deposition of the sample with NH_3 and irradiation for 1 hour with electrons at 2 keV. We clearly observe that desorption of mass 17 occurs at two different temperatures, around 100K and around 140K. Several other masses are detected during the TPD, i.e. mass 2, 14, 15, 16, 18, 28, 30. Desorption of these masses produces different peaks in the spectrum.

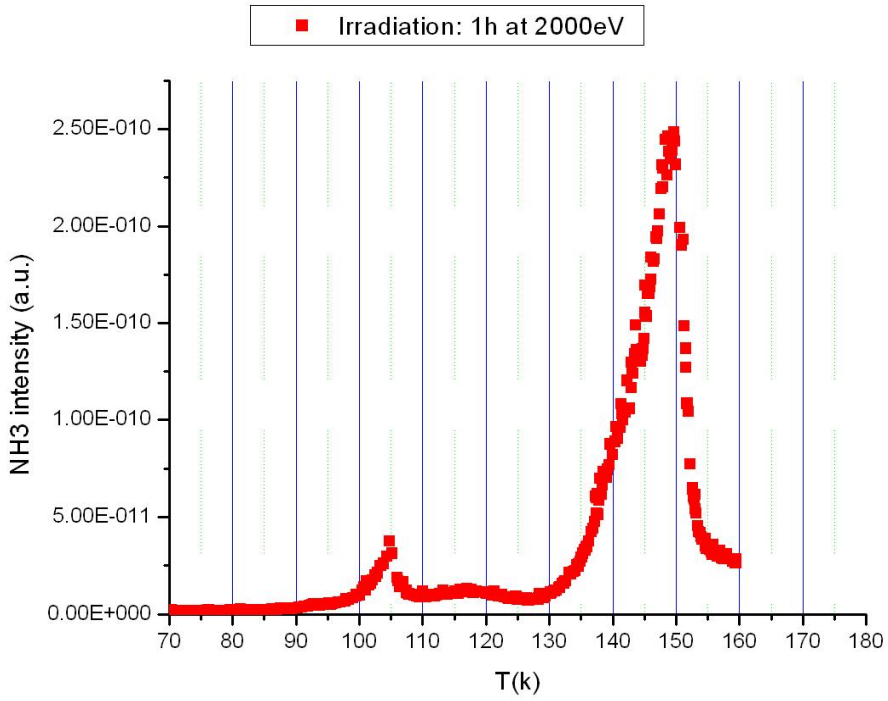

Fig.4.18. A typical TPD spectrum of NH_3 with dose, irradiation time (1h) and energy (2 keV) fixed.

In order to detect the effect of electron irradiation we detected TPD spectra in the following experimental conditions:

a) "Vacuum", TPD acquired in absence of both NH_3 deposition and electron irradiation;

b) "Irradiation only", TPD acquired by irradiating with electrons the steel sample;

c) "Deposition and irradiation", TPD acquired by irradiating with electrons a bulk of previously deposited NH_3 ice. Different times of gas deposition and electron irradiation were taken into account in order to detect a dependence of TPD from them.

A TPD spectrum acquired in the experimental conditions a) is shown in figure 4.19. We mainly detected mass 18, a residual signal related to mass 17 and 16 is also detected.

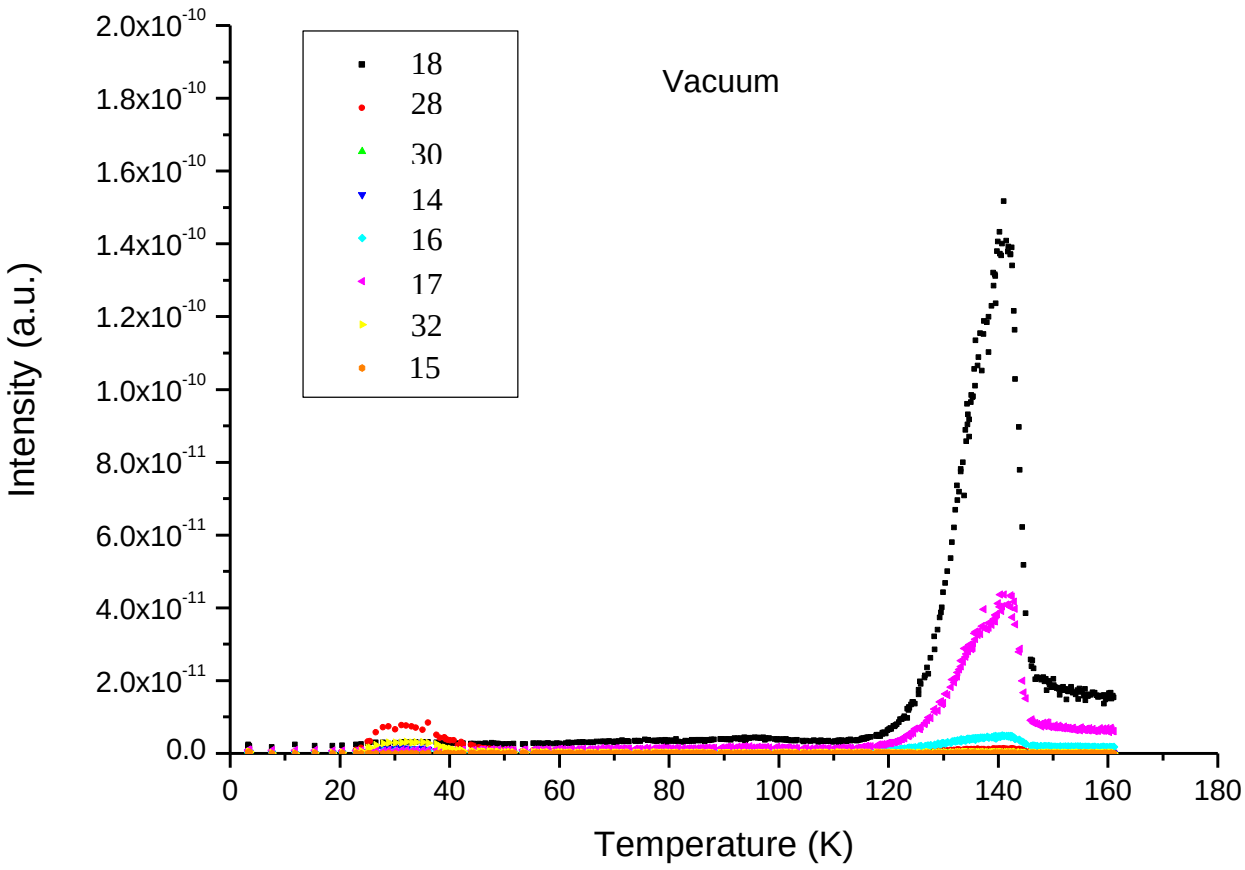

Fig. 4.19. A TPD spectrum in absence of both NH_3 deposition and electron irradiation

Peaks arise around 140K, we attributed this desorption temperature to the release of water ice from the sample. A typical TPD spectrum at conditions b) is shown in figure 4.20. Here we observe mainly desorption of adsorbed mass 17, i.e. NH_3. Desorption occurs around 100-110K, we attributed this desorption temperature to the release of NH_3 molecules from the adsorbed bulk.

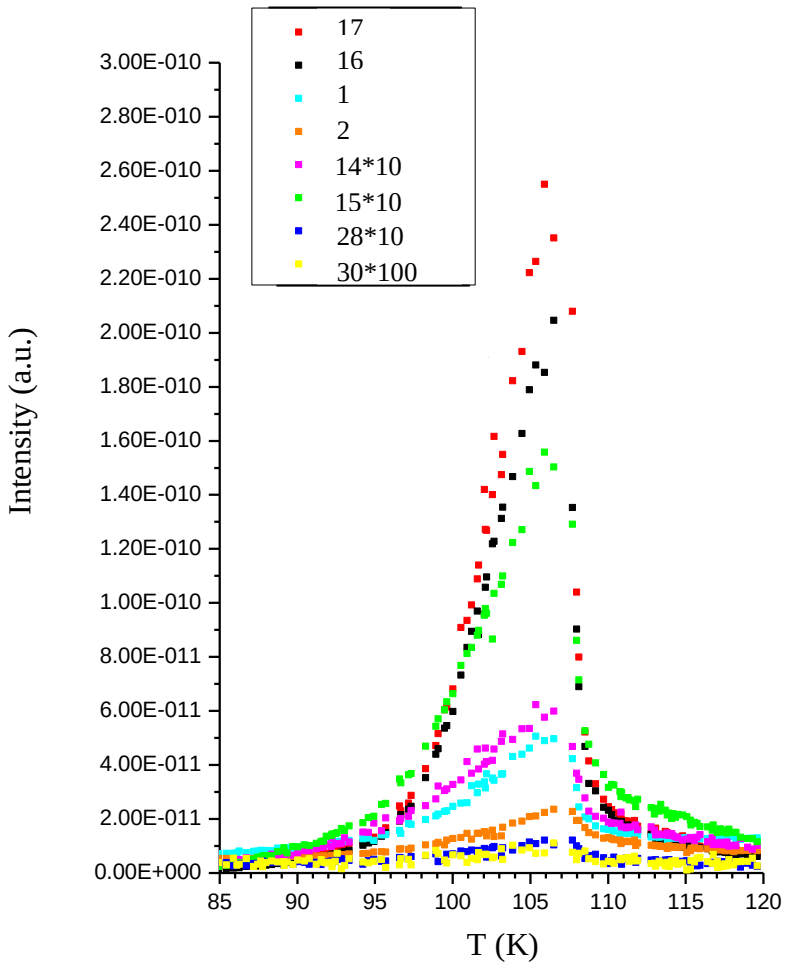

Fig.4.20. TPD spectra after electron bombardment without exposure

A TPD spectrum for case c) is shown in figure 4.21. Desorption of species around 100K and around 140K is still present. Desorption of some species produces peaks at temperatures different from the previous ones. In the experiments a), b) and c) we distinguished in total four peaks, not all present for any species.

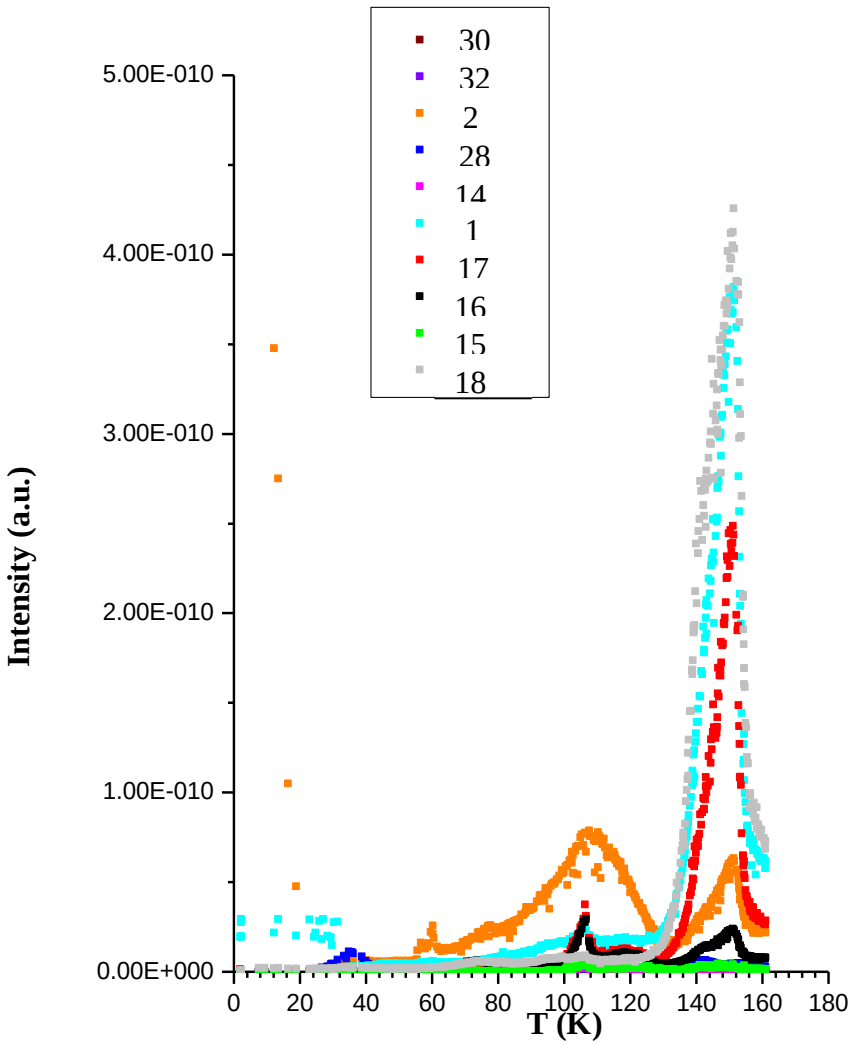

Fig. 4.21. TPD spectra acquired after electron bombardment on solid ammonia

We summarized in table 4.2 desorption temperatures of each mass in the different experimental conditions we performed. In the table assignment between mass and species is also shown.

Mass	Peak 1 (K)	Peak 2 (K)	Peak 3 (K)	Peak 4 (K)
1 hour 2 keV				
14 (N)	10-50		80-110	120-140
15 (NH)	10-40		75-110	120-140
16 (NH_2)	20-40	40-65	75-110	120-140
17 (NH_3)			75-110	120-140
18 (H_2O)				120-140
28 (N_2)	10-40	50-70	80-100	120-140
30 (N_2H_2)	20-40	60-70	85-120	130-160
32	10-40			120-140
Vacuum				
14 (N)	20-40		90-110	120-140
15 (NH)			90-110	120-140
16 (NH_2)	20-40	60-90	90-110	120-140
17 (NH_3)			80-110	120-140
18 (H_2O)				120-140
28 (N_2)	20-50			120-140
30 (N_2H_2)				
32	10-60			120-140
No irradiation				
14 (N)	10-40		80-120	130-140
15 (NH)	20-60		70-120	
16 (NH_2)	20-40		80-110	130-150
17 (NH_3)			80-120	130-140
18 (H_2O)				120-140
28 (N_2)	10-50			120-140
30 (N_2H_2)				
32	20-50			120-140

Table 4.2.

As we can see from table 4.2 a lot of species are present even in the "vacuum only" experiment, case a). The most abundant species in this case is water, which desorbs at peak position 4 (figure 4.19). As no deposition of NH_3 was performed residual gases inside the

vacuum chamber adsorb on the steel sample. We assume reasonably true that desorption at peak position 4 is due to water bonded to steel, during desorption other species trapped in water come out. In the experiments without irradiation, case b), we mainly observe mass 17 (NH_3) desorbing at peak position 3. Other masses coming out may be assigned to 1) cracking fraction of NH_3 inside the mass spectrometer and 2) species trapped inside the bulk of NH_3. At peak position 1 some species desorb. We attributed this desorption to molecules able to escape from the NH_3 bulk. Even if this desorption occurs in all the three kind of experiments, i.e. case a, b and c, we will show here that irradiation of NH_3 with electrons is able to produce new molecules. Let us consider mass 16 (NH_2) first. Differently from mass 17, which desorbs only at temperatures corresponding to peak positions 3 and 4, mass 16 desorbs also at peak position 1 and 2 (in these last case only in the experiments with irradiation of electrons). This suggests that mass 16, which we attribute to NH_2, cannot be produced exclusively by cracking fraction of NH_3. We exclude that mass 16 could be attributed to O^+ because in this case it should be produced by cracking fraction of O_2 and the detected intensity of this last is much lower than the intensity detected for mass 16. Furthermore the intensity of mass 16 doesn't change with dose of adsorbed NH_3, while it increases by increasing the energy of the electrons, strongly suggesting that the peak is related to the effects due to electron irradiation. More difficult is to deduce that mass 15, that we attributed to NH, is produced by electron irradiation. Desorption at peak position 1 is not present in the "vacuum only" experiments, while it is arising both in the experiments with and without electron irradiation. Thus mass 15 is related to mass 17 but we were not able to distinguish the signal arising from cracking fraction (both mass 17 and 16) from the signal (if existing) due to electron irradiation. In the light of the previous considerations we can then get the following first conclusions on the effects of electron irradiation of adsorbed NH_3:

1. Some nitrogen bearing species are detected also in absence of irradiation with electrons.
2. Mainly we can attribute the presence of this species to the cracking fraction of NH_3.
3. We can assume without any doubt that a certain amount of NH_2 is produced by electron irradiation, more difficult it is to assess the production of NH.

Let us now discuss on the production of the remaining species detected. We attributed mass 28 to N_2. In figure 4.22 we show mass 28 spectra after irradiation with electrons.

We observe the presence of peak 2 which is absent in the spectra taken under the conditions "vacuum only" and "deposition only". Besides peak 1 has a higher area than in the absence of electron irradiation. So we can assume that N_2 is not entirely due to NH_3 cracking fraction and some of it is produced by electron bombardment.

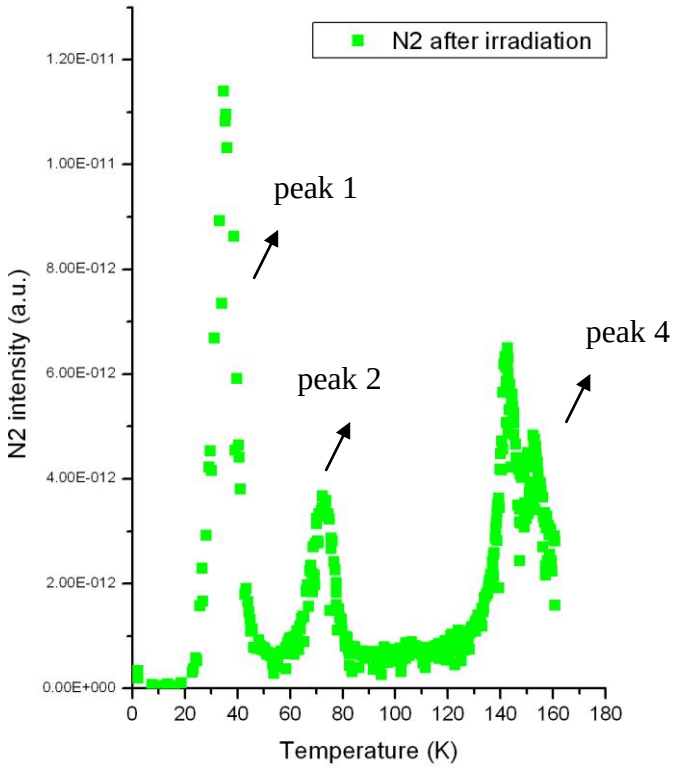

Fig.4.22. N_2 TPD spectrum after electron bombardment

By the way peak 1 of N_2 mass spectrum is also present in the experiments we did to calibrate the thermocouple. In that case desorption of several pure gases was studied and among those also N_2. In the experiments with electron irradiation, mass 2, which we attributed to H_2 and which is not included in figure 4.18, has intensity comparable with the signal of N_2. This experimental result suggests that electrons dissociate NH_3 molecules and that recombination of the fragments produces N_2 and H_2. Finally let us consider formation of N_2H_2 and N_2H_4. Zheng et al. (**[37]**) reported the synthesis of hydrazine and diazene by irradiating solid

ammonia at low temperature (10-60 K) with high energy electrons (5 keV). Our experiments suggest that also at lower energy of irradiation some chemistry occurs but we did not have confirmation about formation of N_2H_4. Hydrazine has mass 32, the same as O_2. We detected a low signal related to mass 32 but, as this signal is ever present in our experiments and we did not observe any increase in the intensity when NH_3 is irradiated with electrons, we assigned mass 32 to molecular oxygen. A different case is that of diazene (mass 30). In figure 4.23 we show mass 30 spectrum after electron irradiation. Mass 30 is not present in absence of irradiation while it appears clearly when NH_3 is irradiated with electrons.

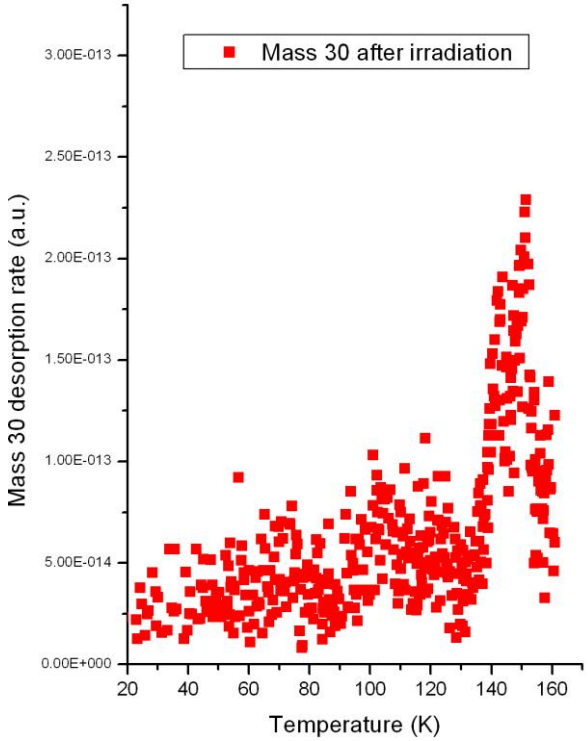

Fig. 4.23. Mass 30 (N_2H_2) TPD spectrum after electron bombardment

In conclusion we showed that, by irradiating solid ammonia with low energy electrons, the following species are certainly produced: NH_2, N_2, H_2, N_2H_2. Nothing we can say about formation of NH and N_2H_4, reported instead in the work of Zheng et al. (**[37]**) which irradiated solid ammonia with higher energy electrons. Let us now look to the chemical pathways which brings to the formation of the detected species. We simply attribute formation of NH_2 to the breaking of NH_3 into NH_2 + H. The unimolecular decomposition of ammonia via the two possible reactions:

$$NH_3 \rightarrow NH + H_2 \quad (1)$$
$$NH_3 \rightarrow N + H + H_2 \quad (2)$$

has a lower probability to occur (**[51]**). Two nitrogen atoms, produced by reaction 2, can recombine to form N_2. Both reactions 1 and 2 provide a mechanism for formation of molecular hydrogen. More difficult is to argue formation of N_2H_2. Zheng et al. (**[37]**) propose that two neighboring amino radicals can recombine to form internally excited hydrazine, which can stabilize to hydrazine or undergo unimolecular decomposition forming, among others, N_2H_2. The reaction mechanisms proposed are the following:

$$2\ NH_2 \rightarrow [N_2H_4]^* \quad (3)$$
$$[N_2H_4]^* \rightarrow N_2H_4 \quad (4)$$
$$[N_2H_4]^* \rightarrow N_2H_3 + H \quad (5)$$
$$[N_2H_4]^* \rightarrow N_2H_2/NNH_2 + H_2 \quad (6)$$

In our experiments it seems that internally excited hydrazine, produced through reaction 3, decays preferentially through reaction 6, producing N_2H_2 and H_2, which are both observed by us. We were not able to detect desorption of hydrazine during the warm up of our irradiated or not irradiated solid ammonia sample.

3) Conclusions

In order to detect the effects of electron irradiation we detected TPD spectra in the following experimental conditions:

a)“Vacuum”, TPD acquired in absence of both NH_3 deposition and electron irradiation;

b)“Irradiation only”, TPD acquired by irradiating with electrons the steel sample;

c)“Deposition and irradiation”, TPD acquired by irradiating with electrons a bulk of previously deposited NH_3 ice. Different gas exposures and electron irradiation times were taken into account in order to detect a dependence of TPD from them.

We deduce the following consideration.

The peaks 4 arise at about 140 K and this desorption temperature corresponds to the release of water ice bonded to steel; during desorption other species trapped in water come out.

- **17 a.m.u. (NH_3)**

Mass 17 desorbs at 110 K and 140 K (fig. 4.18). We can assume that desorption in the range of 110 K is due to the release in gas phase of the NH_3 bulk. Desorption at 140 K takes place when species bonded to the steel head of the cold finger desorb as a whole and mass 17 is among them.

- **16 a.m.u (NH_2)**

Mass 16 desorbs also at peak positions 1 and 2 and in the latter case the peak appears only after bombardment (fig. 4.21). This suggests that mass 16 cannot be produced exclusively by cracking fraction of NH_3. We exclude that mass 16 corresponds to O^+ because in this case it should be produced by cracking fraction of O_2, but the intensity of this last is much lower than the intensity detected for mass 16. Moreover the intensity of mass 16 does not change with NH_3 dose, but increases by increasing the energy of electrons. This suggest that the peak of NH_2 is strongly related to the effects of electron bombardment.
We simply attribute formation of NH_2 to the reaction:

$$NH_3 \rightarrow NH_2 + H.$$

So NH_2 is a product of NH_3 electron bombardment.

- **15 a.m.u. (NH)**

It is very difficult to evaluate the main mechanism of NH production.
NH peak at position 1 is present both in experiments with and without electron bombardment, but not in the case of ”vacuum only” experiment. Mass 15 is obviously related to mass 17, but we are not able to distinguish between a signal due to cracking fraction and a possible signal due to electron irradiation.

- **28 a.m.u. (N_2)**

In the “ vacuum only” and of “ irradiation only” experiments peaks 2 and 3 are absent, while peak at position 1 is more intense after bombardment. So it is reasonable to think that N_2 is not entirely due to NH_3 cracking fraction operated by the quadrupole filament, but some of it is produced by electron bombardment.
Molecular nitrogen is related to reaction (2); two nitrogen atoms, produced by reaction (2) can recombine to form N_2:

$$NH_3 \rightarrow N+H+H_2 .$$

- **2 a.m.u. (H_2)**

In the experiments with electron bombardment signals of N_2 and H_2 are comparable, so we suppose that electrons dissociate NH_3 molecules and that recombination of the fragments produces N_2 and H_2. Molecolar hydrogen is produced by both reaction (1) and (2). In our experiments it seems that internally excited hydrazine (N_2H_4), produced through reaction (3), decays preferentially through reaction (6), producing N_2H_2 and H_2:

$$2\ NH_2 \rightarrow [N_2H_4]^* \quad (3)$$
$$[N_2H_4]^* \rightarrow N_2H_2/NNH_2 + H_2 \quad (6)$$

- **32 a.m.u. (N_2H_4 or O_2)**

Zheng et al. (**[37]**) reported the synthesis of hydrazine (N_2H_4) and diazene (N_2H_2) by irradiating solid ammonia at low temperature (10-60 K) with high energy electrons (5 keV). Our experiments suggest that also at lower energy of irradiation some chemistry occurs but we did not have confirmation about formation of N_2H_4. We detected a low signal related to mass 32, but the signal is ever present and its intensity does not increase when NH_3 is irradiated with electrons. So we attribute mass 32 to molecular oxygen.
Internally excited hydrazine is produced by reaction (3), but it is possible that it decays through reaction (6) producing diazene and molecular hydrogen:

$$2\ NH_2 \rightarrow [N_2H_4]^* \quad (3)$$
$$[N_2H_4]^* \rightarrow N_2H_2/NNH_2 + H_2 \quad (6)$$

- **30 a.m.u. (N_2H_2)**

We analyzed diazene spectra in the three experimental conditions. Mass 30 is not present in the case of exposure only, while it appears clearly when NH_3 is irradiated with electrons (fig. 4,23).
The reaction which describes diazene formation mechanism is (6), during hydrazine decay.

$$[N_2H_4]^* \rightarrow N_2H_2/NNH_2 + H_2 \quad (6)$$

In conclusion we showed that, by irradiating solid ammonia with low energy electrons, the following species are produced: NH_2, N_2, H_2, N_2H_2. Nothing we can say about formation of NH and N_2H_4, reported instead in the work of Zheng et al. (**[37]**) which irradiated solid ammonia with higher energy electrons.

4.3.2 Thermal Desorption Spectroscopy of solid methane

The interstellar medium (ISM) is composed of gas for 99% and contains about 10% of the mass of our Galaxy. Hydrogen and helium represent respectively 93.38% and 6.49% of ISM chemical composition, while oxygen, carbon and nitrogen contribute only with 0.11% (O:C:N = 6:3:1, **[85]**). To this elementary composition correspond 106 identified species, that aren't homogeneously diffused in the interstellar medium, but localized in large-scale structures as dense interstellar clouds. Molecules, atoms and radicals at gas state condense on dust grains surface of molecular clouds (at 10 K) creating an icy mantle with a thickness of 0.1 μm .The presence of ices is confirmed by IR spectroscopy of obscured stellar sources and in interstellar grains are localized solid mixture containing H_2O, CO, CH_4 and NH_3 (**[86]**).

Ices of molecular clouds and solar system bodies are subjected to the action of comic rays, UV photons and energetic particles of the Galactic cosmic radiation fields.

Interstellar dust represents only 1% of IMS mass, but grains nuclei are mainly composed by carbon; this composition is fundamental in the formation of new molecules (**[87]**) .Several studies show that in energetic processing of carbon-containing ices subjected to UV, to energetic ions or to simple warm new complex organic species are formed (**[88]**). The most important process caused by cosmic ray interaction with matter is ionization.

Though the icy mantels are rarely under energetic electron bombardment, the electrons emitted in ionization processes can be energetic enough to further ionize or excite surrounding molecules creating photons, electrons, ions, radicals and roto-vibronically excited species **[89]**. A dependence of the yields of reaction products from temperature also exists: reactions appear more efficient if temperature is about 25K (**[90]**).

To better understand the cosmic radiation induced formation of new organic species, thus the chemical evolution of cold molecular clouds of our solar system, it is essential to understand the effects of electron bombardment on the chemical reactions in the ices (**[51]**).

In this work we present an experimental investigation on (500eV-3000eV) electron induced chemical reaction in solid methane at 20 K

We use Thermal Desorption Spectroscopy (TDS) to study the electron gun effects on solid methane and through a quadruple mass spectrometer we also analyze the formation of new molecules after bombardment.

1)Experimental

The experiments were conducted in a UHV chamber (base pressure in the low 10-10 Torr range) evacuated with a dry turbo pump. The UHV system is equipped for TDS with a steel cool head which work in the range of 20-300 K, with an electron source and with a computer controlled quadrupole mass spectrometer to monitor various gas species released during the thermal desorption processes.

For each of them, a mass scan of about 40 data points was taken and the integrated area was used as the signal intensity. To better detect all desorbed gases, an automatically adjusted and differently set sensibility scale was used for each mass.

Methane ice was formed by condensing CH_4 onto the stainless steel cold head surface (7 cm^2) of a close cycled He refrigerator. CH_4 gas (purity of 99.999%) was introduced in the chamber through a precision leak valve and dosed through a 2 mm diameter Cu tube, with its end reproducibly positioned at <1 mm away from the cold surface (with a linear motion device) enabled to growth of a column-like bulk film. The pressure of gas in Cu tube is fixed and while keeping the sample at a desiderate adsorption temperature (about 20 K) for a 10 minutes the gas was pumped out. The sample temperature was monitored with an Au/0.7 Fe%-chromel thermocouple and the adsorption temperatures was (20±2)K.

Sample heating was achieved by simply turning off the refrigerator compressor. In the temperature range of our interest (40K-120K) the heating rate was nearly constant (3K/min).

Thermal desorption (TDS) was achieved by heating naturally the head of cold finger and desorbed molecules were measured with a quadrupole mass analyzer. Quadrupole mass spectra and the sample temperature recording were synchronized.

To study electron-induced surface chemistry an electron beam was produced by the electron gun with a beam current in the order of μA; the electron beam was totally de-focalized with a spot size similar to the sample surface area to avoid the local heating. The average incident electron energy was chosen in the range 200-3000 eV and the bombardment time ranged between 15 min and 4 h.

No appreciable contamination gas signals were detected neither in the adsorption nor in the desorption processes. A total reproducibility of gas line cleanness was observed.

The most interesting variables we considered were the electron beam energy and the electron doses (fixed by bombardment time). In effect we conduct the experiments varying the electron energy in the range 200-3000 eV and the bombardment time in the range 15 min-4h. The CH_4 dose was fixed to 3000 Langmuir in all experiments.

In absence of electron irradiation TDS results show the presence of molecules with an atomic mass (a.m.u.) of: 1-2-12-13-14-15-16-17-18-26-28-29-32, as clearly shown in fig. 4.24.

The 16 a.m.u. mass is certainly associated with $^{12}CH_4$ specie. In both blank and irradiated TDS experiments we note a massive presence of CH_4. This clearly indicate that only a fraction of CH_4 is interested from electron irradiation or quadrupole effects.

Considering the purity of gas, the unimportant system contamination and the carbon isotopic abundance (98.9% for ^{12}C and 1.1% for ^{13}C **[91]**) we can attribute these masses to the following molecules: H, H_2, ^{12}C, CH, ^{13}C, CH_2, CH_3, $^{13}CH_4$, C_2, C_2H_2, C_2H_5.

We can associate the molecules obtained in irradiation absence to CH_4 cracking fraction in gaseous phase caused by the quadrupole mass spectrometer filament (the average energy of quadruple filament electrons is about 60 eV **[92]**).

We mention that, for background dosing, two distinct desorption peaks were observed for as deposited CH_4 thin films with a temperature difference of 10K and their intensity ratio remained constant as the amount of the adsorbed CH_4 varied. This was due to adsorption on two different portions of the cold head, as checked with a set of thermocouples positioned on various parts of the second stage of the refrigerator. the desorption features reported in this paper are relative to those coming from the coldest area which could be subjected to electron irradiation.

2)Results and Discussions

In Fig. 4.24 we present four typical mass spectra taken at temperatures of $T = 47K$ and $T = 62\,K$ during thermal desorption of a thin solid methane film deposited with $350\,L$ background dosing ($1L = 1x10^{-6} Torr \cdot sec$). Spectra *a* and *b* are for the sample irradiated with 2000 eV electrons while spectra *c* and *d* are relative to an as deposited film. For the purpose of comparison we also shown the mass spectra taken by filling the chamber at $1x10^{-6} mbar$ and room temperature with CH_4, C_2H_6, and H_2 gases (curves *e*, *f*, and *g*, respectively).

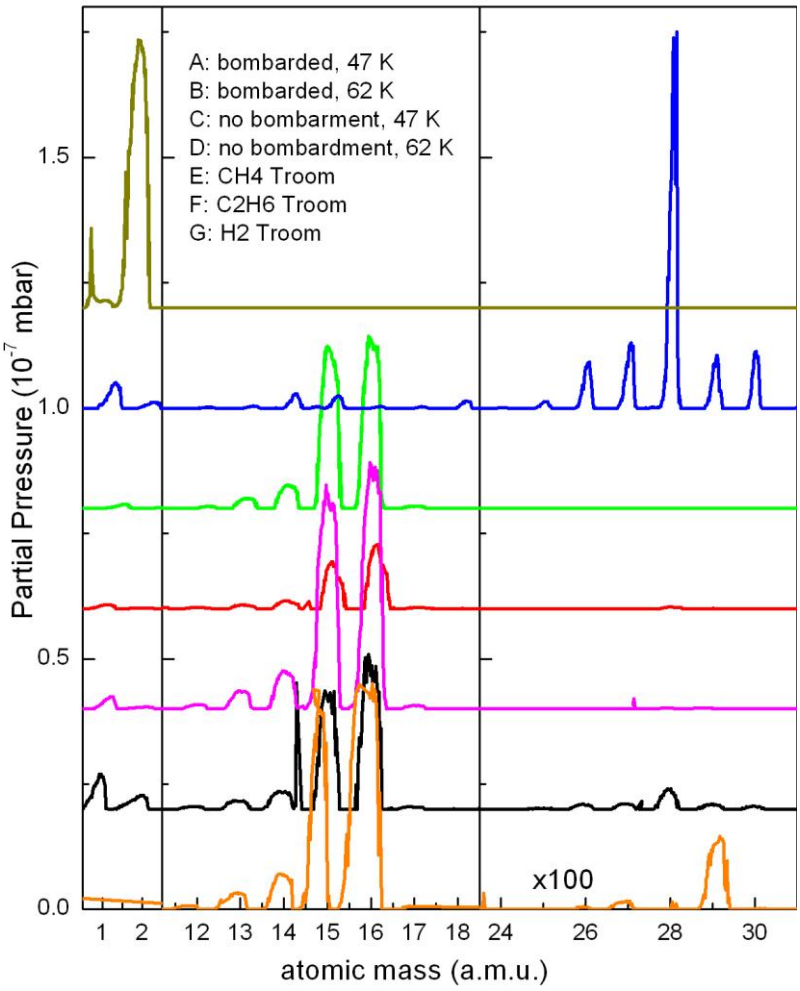

Fig.4.24(1). Quadrupole mass spectra taken during thermal desorption of a 2 keV electron bombarded thin CH_4 film at 47 K (curve *a*) and 62 K (curve *b*) and for an as-deposited film (curves *c* and *d*). Also shown are the scans for background filled methane, ethane and hydrogen gases at $1x10^{-6}$ mbar (curves *e*, *f*, and *g*, respectively). For the sake of clarity, all curves have been shifted.

We first note that the quadrupole filament (operating at 60V) produced a great amount and variety of fragments for methane and ethane. This certainly overshadowed the effects of electron irradiation on solid CH_4. Indeed, the intensity ratios of CH_x to CH_4 and C_2H_x to C_2H_6 are very similar for curves *a*), *c*), and *e*) and for curves *b*), *d*) and *f*), respectively, clearly indicating that the quadrupole filament cracking is the far most dominant mechanism for the observed dissociation of methane and ethane.

Thermal desorption curves of the relevant species for an electron bombarded sample are illustrated in Fig.4.25. The film was obtained by background dosing and its thickness was

approximately 1350 Å (or 350 layers) allowing the primary electrons of 2000 eV to penetrate through. The electron flux was $\Phi = 2x10^{16}\ electrons/cm^2$. The spectra can be gathered into three groups which appear separately in different temperature ranges.

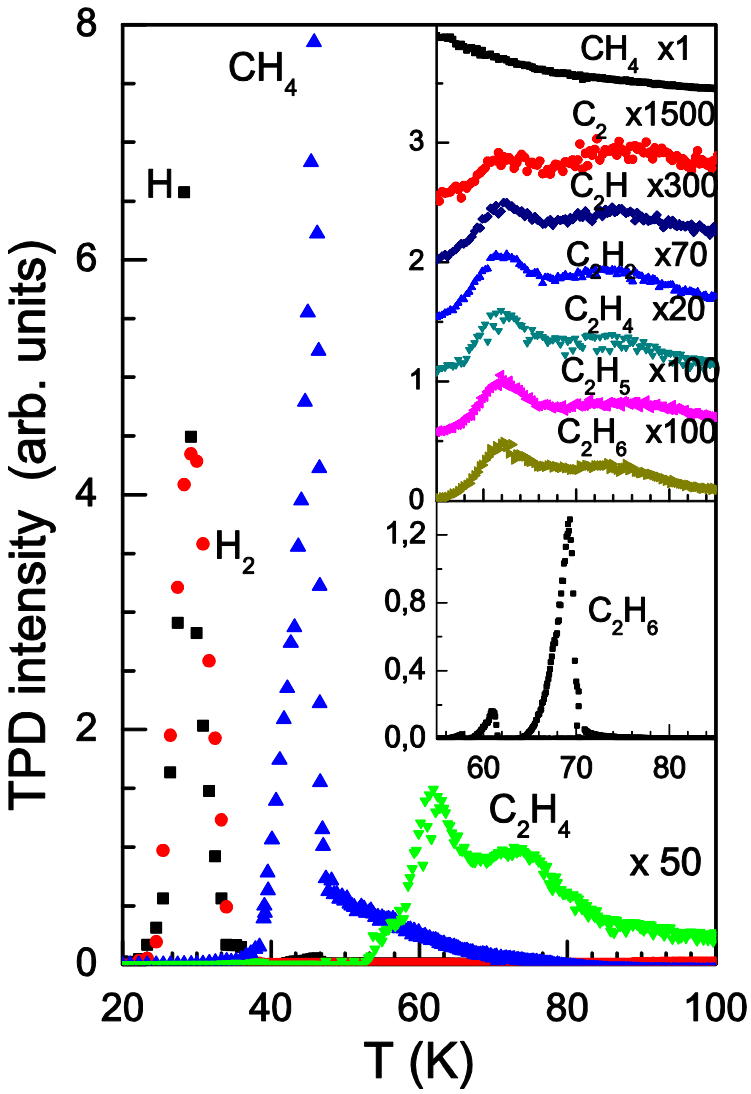

Fig.4.25. Thermal desorption traces of some relevant species for a background dosed methane film of 450 L after 60 min of 2keV electron bombardment at a current density of 880 μA/cm^2. In the upper panel of the inset are shown the traces of C_2H_x while that illustrated in the lower panel is for an as deposited ethane film.

Methane and its derivates CH_x are released at about 47 K, atomic and molecular hydrogen signals are seen at 29 K and together with CH_x at 47 K, whereas the C_2H_x species desorb at higher temperatures with two wider features centered at 62 and 75 K. We notice that for

T>50K, the TPD curve for CH_4 is structureless though its intensity is much higher than those of C_2H_x species.

To further study the irradiation effects, we condensed a column-like bulk CH_4 with relatively small quantity of methane gas avoiding the over pressure during desorption. The thickness was estimated to be a few tens of μm and quite reproducible as judged by the total desorbed CH_4 signal. The monotonous increase of the amount of desorbed C_2H_6 and C_2H_2 plotted in Fig. 4.26 as a function of the electron irradiation time clearly demonstrates the effects of electron stimulated reactions.

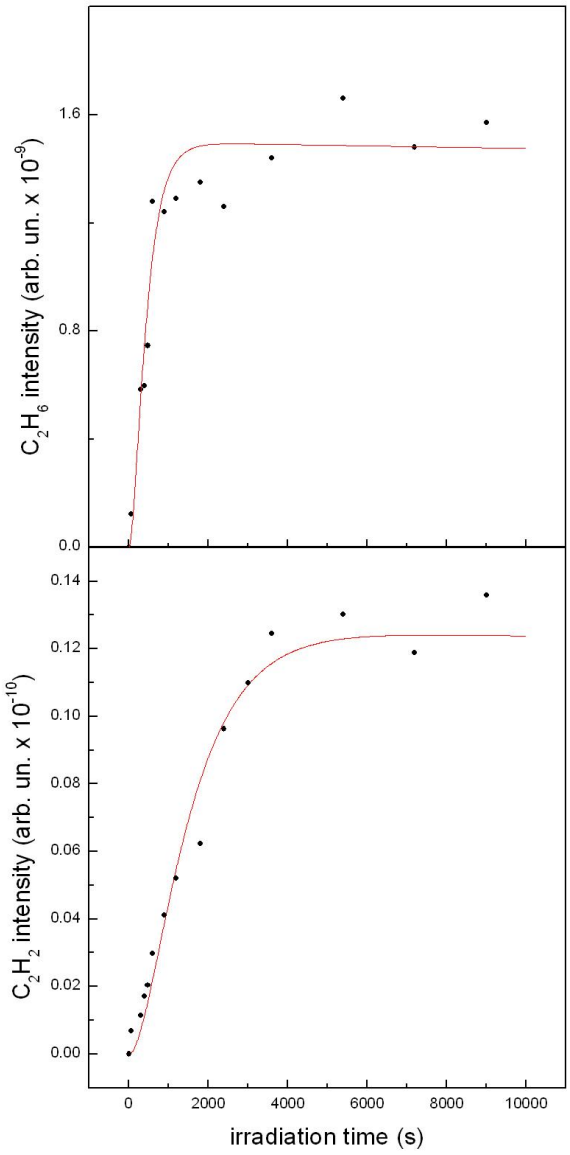

Fig. 4.26 (3). Total C_2H_6 intensity produced by 2keV electron bombardment on a thick solid CH_4 film as a function of irradiation time. The continuous curve is a best fit by using a simple rate-equation based recombination model (see text).

In discussing the electron induced dehydrogenation occurring in the solid methane matrix, we mention that the energy required for CH_4 dissociation is only a few eV so that the impinging primary electrons and also secondary electrons generated in the cascade could produce CH_x fragments with CH_3 being the most important ones (see Tab. 4.3) **[93]**. Because of the dominant quadrupole cracking effects of desorbing methane molecules from a large portion of cold surfaces which were not subjected to electron bombardment, a direct detection of these CH_x reaction products through thermal desorption spectra was difficult.

	20 eV (secondary electrons)	60 eV (quadrupole filament electrons)	2000 eV (electron beam energy)
CH_3	5×10^{-18}	2×10^{-16}	9×10^{-17}
CH_2	1×10^{-18}	2×10^{-17}	3×10^{-18}
CH	3.01×10^{-19}	2.2×10^{-17}	2.2×10^{-18}
C	1.03×10^{-19}	3.4×10^{-18}	3.34×10^{-19}
H	1.23×10^{-19}	2.437×10^{-17}	3.267×10^{-18}

Tab. 4.3. Cross section (cm^2) vs electron Energy for emission of product from CH_4 electron irradiation

However, these reactions could still be inferred from the observation of molecular hydrogen during electron irradiation (Fig. 4.27 and fig. 4.28). Indeed, turning on and off the electron beam with use of a mechanical shuttle resulted in a quite reproducible on-off behavior of the H_2 signals.

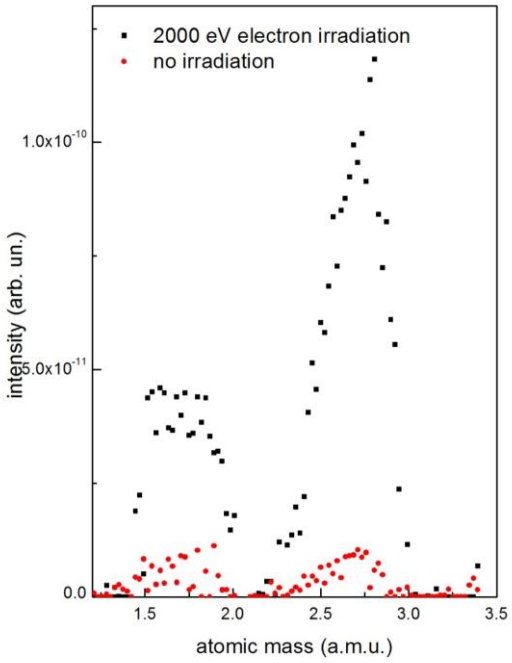

Fig. 4.27. H and H_2 TPS spectra during bombardment and turning off the electron beam, with an energy of 2 keV.

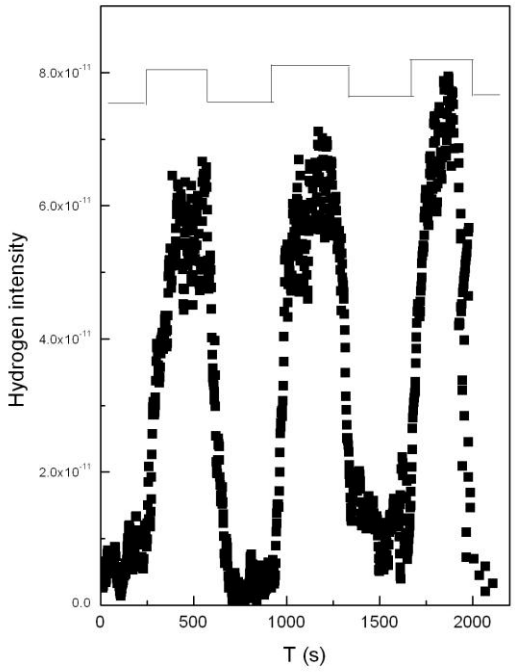

Fig. 4.28. H_2 TPS spectra during bombardment and turning off the electron beam as a function of irradiation time, with an energy of 2 keV.

In the solid, to the molecular dissociation may follow a recombination process, which is negligible in gas phase because of the large intermolecular distance. The most favored recombination reactions are those with very low binding enthalpies, as the formation of hydrogen molecules, acetylene, ethylene, and ethane. A simple recombination reaction between two adjacent CH_x (x=1, 2, 3) molecules may form HC≡CH, $H_2C{=}CH_2$, and $H_3C\text{-}CH_3$ with a triple, double, and single carbon-carbon bond, respectively.

The fact that all C_2H_x TPD curves have nearly the same line shape (upper panel of the inset of Fig.4.25) would strongly suggest an essentially common origin of these species. A comparison of the intensity ratios seen in the TPD curves between C_2H_x and C_2H_6 with those recorded for ethane gas (curve *g* of Fig. 4.24) reveals that virtually all observed dicarbonic species could be attributed to the quadrupole filament cracking of desorbed ethane molecules except for acetylene. Indeed, in this later case, the detected intensity ratio is much higher than the cracking faction. This observation leads us to conclude that a substantial portion of C_2H_2 must have formed in the CH_4 matrix upon electron irradiation.

We point out that the difference in the desorption temperatures for CH_3 (CH) and C_2H_6 (C_2H_2) species unambiguously indicates that ethane (acetylene) molecules are formed in the solid during electron irradiation or during thermal annealing, but certainly not in gas phase during desorption.

To get some estimates on the process of CH_4 dehydrogenation into CH_3 and the subsequent CH_3 recombination into C_2H_6, we first note that the probability that a molecule within the reaction depth l gets hit by a 2keV electron in a second is $P_1 = \frac{I}{1.6\text{x}10^{-19}\rho l}$ where $I = 8.8\text{x}10^{-3}\ Am^{-2}$ is the electron beam density and $\rho = 1.694\text{x}10^{28}\ m^{-3}$ the site number density. The probability a methane molecule undergoes a collision with a primary electron is $P_1 \cdot \theta_{CH_4}$ with θ_{CH_4} denoting the CH_4 concentration: $\theta_{CH_4}(t=0) = 1$ and $\theta_{CH_4}(t=\infty) = 0$. In the case of background dosing as that shown in Fig. 4.25, the film thickness $d = 135\ nm$ was smaller than the primary electron penetration length λ so that chemical reaction took place through the whole sample thickness: $l = d$, $P_1 = 2.45\text{x}10^{-5}$. The dissociation probability for CH_4 is $P_2 = \frac{\sigma}{\pi r^2} = 8.05\text{x}10^{-2}$ with $\sigma = 9.5\text{x}10^{-17}\ cm^2$ being the cross section at 2keV and $r = 1.95\ A$ the molecular mean radius. Therefore, the probability that a CH_4 molecule to be dissociated in a second is $P_1 \cdot \theta_{CH_4} \cdot P_2 = 1.97\text{x}10^{-6}\ \theta_{CH_4}$. Considering that a 2keV electron produces many secondary electrons, we may reasonable assume the total number of hits to be at least 50 with a similar σ, then the real probability of dissociating a

CH_4 molecule in a second can be as high as $1x10^{-4}\theta_{CH_4}$. For $\theta_{CH_4} = 1$ the total probability of dehydrogenation in an hour is $P = 36\%$, thus as a first approximation we may take a simple average value of $\theta_{CH_4} = \frac{1+(1-0.36)}{2} = 0.82$ so that $P = 30\%$.

Experimentally, the intensity ratio between C_2H_6 (including its cracking fragments) and CH_4 originating from electron bombarded region is about $1.8x10^{-2}$, thus that between CH_3 involved in the recombination and CH_4 is $3.6x10^{-2}$. This later value indicates that only about 10% of produced CH_3 recombine to form C_2H_6.

To somehow quantitatively describe the kinetics of electron induced reactions occurring in the solid matrix (case of column-like thick film), we assume that the film thickness to be much larger than the electron penetration length and denote with θ_{CH_4} the concentration of CH_4 molecules. The rate equation for methane can be written as:

$$\frac{d\theta_{CH_4}}{dt} = -c_1\theta_{CH_4} + c_2\theta_{CH_3} \cdot \theta_H \qquad (4.1)$$

where c_1 is the rate constant for reduction of CH_4 into CH_x (x=0,1,2,3) and c_2 that for reformation from CH_3 and H. The greatest formation probability is for x = 3, so c_1 is the time corresponding to a total reduction of CH_4 in CH_3, so to the complete formation of a CH_3 ice. Because of the preferential formation of H_2 and its instant release from the solid (see Fig. 4.27), we can reasonably assume $c_2 = 0$. Eq. (4.1) then has a simple solution

$$\theta_{CH_4}(t) = \theta^0_{CH_4} e^{-c_1 t} \quad , \qquad (4.2)$$

where $\theta^0_{CH_4}$ denotes the initial density of CH_4.

The rate equation for CH_3 molecules is given by:

$$\frac{d\theta_{CH_3}}{dt} = c_3\theta_{CH_4} - c_4\theta_{CH_3} = \theta^0_{CH_4} c_3 e^{-c_1 t} - c_4\theta_{CH_3}, \qquad (4.3)$$

where c_3 is the rate constant for dissociation of CH_4 into CH_3 and c_4 that for fragmentation of CH_3 into smaller ones. The solution of (4.3) satisfying the initial condition $\theta_{CH_3}(t = 0) = 0$ is:

$$\theta_{CH_3}(t) = \frac{c_3}{c_4 - c_1}\theta^0_{CH_4}(e^{-c_1 t} - e^{-c_4 t}) \qquad (4.4)$$

As the CH_3+CH_3→C_2H_6 recombination is concerned, if it occurs at low temperature during electron irradiation, then its rate equation is given as:

$$\frac{d\theta_{C_2H_6}}{dt} = c_5\theta_{CH_3}\cdot\theta_{CH_3} - c_6\theta_{C_2H_6} = \alpha(e^{-2c_1 t} + e^{-2c_4 t} - 2e^{-(c_1+c_4)t}) - c_6\theta_{C_2H_6}\,, \qquad (4.5)$$

with c_5 denoting the recombination rate and c_6 the dissociation rate. The solution for (4.5) is

$$\theta_{C_2H_6}(t) = \alpha[(\frac{2}{c_6-(c_1+c_4)} - \frac{1}{c_6-2c_1} - \frac{1}{c_6-2c_4})e^{-c_6 t} + \\ + \frac{1}{c_6-2c_1}e^{-2c_1 t} + \frac{1}{c_6-2c_4}e^{-2c_4 t} - \frac{2}{c_6-(c_1+c_4)}e^{-(c_1+c_4)t}\,] \qquad (4.6)$$

However, if the recombination process occurs during thermal heating (in the solid and before desorption) then the probability of formation of C_2H_6, *P*, is simply proportional to the square of $\theta_{CH_3}(T)$ with *T* indicating the irradiation time:

$$P_{C_2H_6}(T) = \alpha(e^{-2c_1 T} + e^{-2c_4 T} - 2e^{-(c_1+c_4)T}) \qquad (4.7)$$

As shown in Fig. 4.26, fitting to the total intensity of C_2H_6 produced in the solid, sum of all its detected fragments, as a function of electron irradiation time *T* yields $1/c_1 = A = 1\text{x}10^3 s$ and $1/c_4 = C = 1\text{x}10^6$.

An independent evaluation of the rate of electron induced dehydrogenation of a methane molecule in a solid matrix *A* can be made as follows: the reaction depth $d = \lambda = 300\ nA$; $P_1 = 1.13\text{x}10^{-5}$, the probability that a CH_4 molecule to be dissociated in a second is $P_1 \cdot P_2 \cdot c_{CH_4} = 9.1\text{x}10^{-7} c_{CH_4}$. We may reasonable assume the total number of hits to be at least 100 with a similar σ, $c_{CH_4} = 0.8$ then the real probability of dissociating a CH_4 molecule can be $7.3\text{x}10^{-5}$ or more or a constant rate of $1.4\text{x}10^4$ s.

This estimate is just about a factor of 14 off the experimental value of $A = 1/c_1 = 1\text{x}10^3$ s. Considering the roughness of this simple model with large uncertainties in the parameters

used such as λ and the average hits per incident electron, and of the assumption of a uniform distribution of electron-CH_4 collision probability over the depth, we may certainly regard the experimentally determined value of *A* reasonable. We also point out that in 100 hits only 8% will produce dissociation with a total energy loss of only 40 eV or something more.

Further, by assuming that all CH is produced in the solid via dissociation of CH_4 just as in the case of CH_3, we fitted the intensity of C_2H_2 after subtracting the cracking fraction of C_2H_6 with use of eq. (4.5) to (lower panel of Fig.4.25). The so determined time constant $A= 1/c_1= 2x10^3$ s is quite similar to the value obtained for C_2H_6, though the assumed hypothesis is quite rough.

A comparison with the TPD curve of a solid C_2H_6 film (lower panel of the inset in Fig.4.25) show that the binding environments of electron irradiation produced ethane are much more complex with two broad structures centered at about 62 and 73K, in contrast to the sharp desorption peak of bulk ethane at 69K.

3) Conclusions

For little bombardment times there is an increase of the formation probability of C_2H_6, while for high bombardment times C_2H_6 concentration is constant (fig. 4.26); in fact, at high bombardment times CH_4 is completely reduced into CH_x, with a great probability for CH_3 because CH_3 cross section is bigger than CH and CH_2 ones and the last ones processes at two or three electrons are so more energetic.

For $A=1/c_1=1*10^3$ seconds on the cold surface there is a CH_3 ice; CH_3 molecules have a reduced mobility at low temperature, so the probability of the CH_3 molecules recombination into C_2H_6 is very negligible during bombardment; at $A=1/c_1=1*10^3$ corresponds a value of $c_4=1/C=1*10^{-6}$ which confirms the negligible formation rate for ethane (C_2H_6) during bombardment. During TPD, indeed, the kinetic energy of CH_3 molecules increases with temperature, so also their mobility, with the consequent formation of C_2H_6 ($CH_3+CH_3 \rightarrow C_2H_6$). Ethane is considerable as a bombardment product at the second order.

Theoretically during bombardment also formation of CH and CH_2 takes place with the following dehydrogenation of CH_3, but these processes are more energetic and CH and CH_2 cross sections are very small; therefore the formation probability of these two species during bombardment is negligible compared to CH_3 one. CH and CH_2 amounts showed during TPD are due mainly to cracking fraction of CH_4 operated by quadrupole filament. The ratios CH_x/CH are, in fact, constant and independent on bombardment times and energies.

In the same way, C_2H_x species are not generated by bombardment; in fact their formation mechanisms

$$CH+CH \rightarrow C_2H_2$$

$$CH_2+CH_2 \rightarrow C_2H_4$$

are negligible because of the very small concentration of CH and CH_2 during bombardment.

The CH_x spectra showed in TPD are due to cracking fraction of C_2H_6 by the quadrupole filament; in fact the ratios C_2H_x/C_2H_6 do not vary with bombardment energies or time and are constant, also in absence of bombardment. This ratios are also verified by TPD of simple C_2H_6, so it is confirmed that the formation mechanism of C_2H_x is only cracking faction of ethane.

A comparison of the intensity ratios seen in the TPD curves between C_2H_x and C_2H_6 with those recorded for ethane gas (curve *g* of Fig. 4.24) reveals that virtually all observed dicarbonic species could be attributed to the quadrupole filament cracking of desorbed ethane molecules except for acetylene. In fact the ratio C_2H_2/C_2H_6 is higher in the case of bombardment and it increases with electron energy. So acetylene is considerable as a bombardment product at the second order.

The only direct product of methane bombardment is CH_3; C_2H_6 molecules are due to CH_3 molecules recombination during TPD.

4.4 Thermal Desorption Spectroscopy in Geophysics

4.4.1 Thermal Desorption Spectroscopy of zoisite

Zoisite is a calcium aluminium hydroxy sorosilicate belonging to the epidote group of minerals. Its chemical formula is $Ca_2Al_3(SiO_4)(Si_2O_7)O(OH)$. Zoisite chemical composition (in %) is mainly described in the following table **[38]**:

Calcium (Ca)	17.64%	CaO	24.68
Aluminum (Al)	17.82%	Al_2O_3	33.66
Silicon (Si)	18.52%	SiO_2	39.67
Hydrogen (H)	0.22%	H_2O	1.98
Oxygen (O)	45.78%		

Table 4.3

Among the typical impurities of zoisite the most common is water (see table 4.4) **[94]**.

Chemical Properties of Zoisite	
Formula:	$\{Ca_2\}\{Al_3\}[O\|OH\|SiO_4\|Si_2O_7]$
Essential elements:	Al, Ca, H, O, Si
All elements listed in formula:	Al, Ca, H, O, Si
Common Impurities:	Fe,Mn,Mg,Cr,Ti,Ca,Na,V,Sr,H_2O

Table 4.4

When yellow zoisite is heated between (370-650)°C, it becomes an intense violet-blue colour (variety tanzanite); this behaviour was explained in terms of change of the transition metal ions oxidation state **[39]-[41]**.

Rodeghero et al. **[42]** studied the dependence of the colour changes in yellow and blue zoisite after heating not only on the concentration of metal ions and their oxidation states, but also on possible changes in bond lengths and bond angles or distorsion of coordination polyhedra.

In this work we analyze zoisite after an heating from room temperature to 650°C to verify if the change in colour and in structure are due to the loss of a primary element as H or to a dehydration.

1) Experimental

The thermal desorption spectroscopy on zoisite took place in an ultrahigh vacuum system with a base pressure in the chamber in the low 10^{-10} Torr range, obtained using a dry turbo pump.

The zoisite sample was mounted on a molybdenum boat, connected to a power generator stabilized in current; sample was heated from room temperature to 650°C by a generator able to increase linearly the temperature. Temperature was measured by a thermocouple of type J and it was registered by a program which captures the values of temperature and time. Through a multimeter interfaced to a pc voltage is acquired at both ends of a thermocouple, then transformed in the correspondent value of temperature (interpolating the characteristic curve V-T of the thermocouple). Each acquisition of the temperature was effectuated in regular intervals established by the operator.

The setup was equipped with a Quadrupole Mass Spectrometer (QMS) to analyze elements in the chamber during thermal desorption investigation.

The sample investigated was furnished by prof. Ajò from "Institute of Inorganic Chemistry and Surfaces" of CNR, in Padova. Measures were repeated for several portion of the same sample.

2) Results and Discussion

Figure 4.29 shows a spectra of the elements released by zoisite during heating.

How it is possible to note, the desorption products of zoisite are H, O, OH and H_2O. It is reasonable to think that the structural change in zoisite after heating are due to the loss of primary elements as H or OH, but peak intensity and shape for all these elements are similar.

So it is probable that H, O and OH are not products of zoisite structural changes during heating, but the result of cracking fraction of H_2O molecules (released by zoisite during heating) operated by the quadrupole filament, as confirmed by the fact that the ratios H/H_2O, O/H_2O and OH/H_2O are similar.

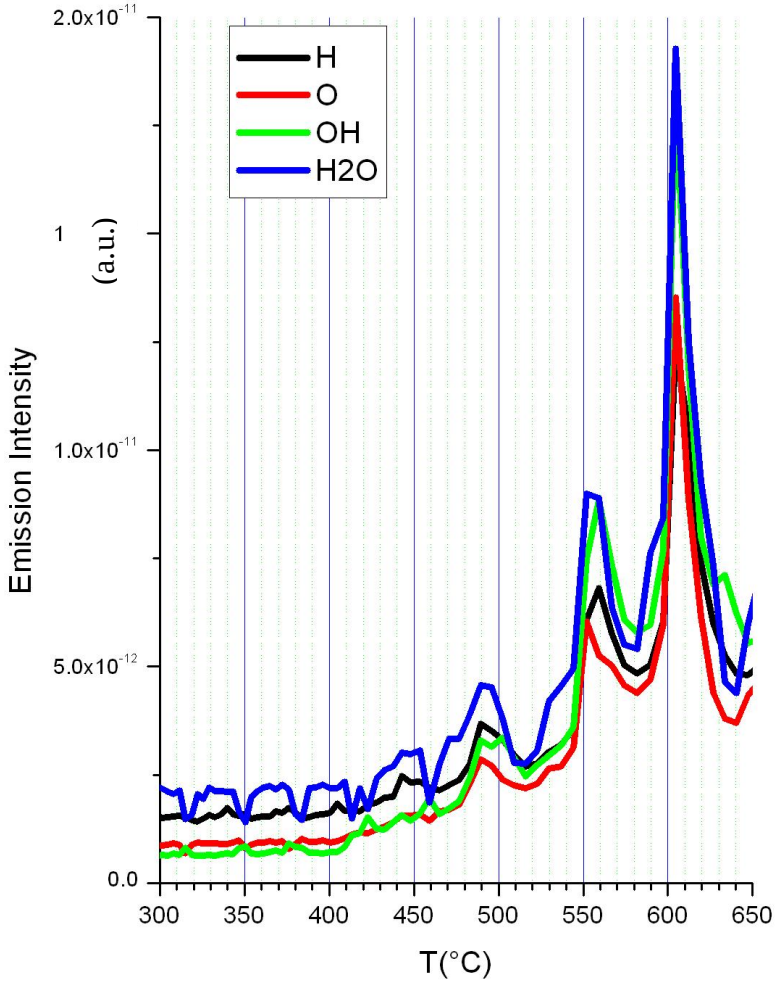

Fig. 4.29. Zoesite spectra after heating from 300K to 650 K.

3) Conclusions

It is reasonable to think that the structural change in zoisite after heating is due to the loss of primary elements as H or OH. The spectra analyzed for O, H, OH and H_2O show comparable

intensities and similar shapes. So it is probable that H, O and OH are not due to zoisite structural changes during heating, but they are the result of cracking fraction of H_2O molecules (contained in zoisite and released during heating) operated by the quadrupole filament. In fact it breaks H_2O molecules forming H, O and OH products in the same proportions, as confirmed by the fact that the ratios H/H_2O, O/H_2O and OH/H_2O are similar.

Conclusions

The purpose of this work was the analysis of Thermal Desorption Spectroscopy (TPD) applications to several Physics branches as Physics of surface, High-Energies Physics, Astrophysics and Geophysics. In fact we use TPD , respectively, to investigate the gas adsorption property of carbon nanotubes, the effects of electron bombardment on ammonia and methane ices and the change in zoisite colour after heating.

Pores of molecular dimensions can adsorb large quantities of gases owing to the enhanced density of the adsorbed materials inside the pores, as consequence of the attractive potential of the pore walls. Carbon nanotubes, which typically have diameters of a few nanometres, should be able to store gas up gases, particularly when they are in the form of disordered aggregates as bundles.

Our attention was focused on molecular hydrogen adsorption on multi-walled carbon nanotubes, to find a possible solution to vacuum problems in Large Hadron Collider. In fact, the synchrotron radiation produced by photons in circular path desorbs molecules from chamber walls (operating at 5-20 K), which deteriorate vacuum. Among the desorbed species the most problematic to pump out is H_2 and a possible solution to LHC vacuum problem is the installation of cryosorbent materials on chamber wall. We studied adsorption property to candidate carbon nanotubes as possible cryosorbers in future accelerators. Our sample was synthesized by chemical vapor deposition using C_2H_4 and subsequently purified by Prof. Nagy's group of Chemical Engineering Department of Calabria University.

More quantitative works are currently being undertaken to determine the realistic possibility of using nanotubes as cryosorbers in UHV systems, but we presented first experimental measurements of molecular hydrogen adsorption on MWNTs in real cryopumping conditions of accelerators at low pressures (10^{-5} Torr) and low temperatures (12-30 K).

We evaluated the dependence of emission intensity on several experimental parameters as exposed mass sample, H_2 dose, exposure temperature, amount of covered surface and heating rate, β. We concluded that:

- At low temperatures MWCNTs adsorb H_2 much more efficaciously than charcoal, with a difference of adsorption capacity of about an order of magnitude

- Adsorption depends only on sample mass and on exposure temperature. The adsorption capacity sharply decreases with exposure temperature and is in the order of 10-7 wt. % at 12 K.

- To each exposure temperature corresponds a specific energetic distribution of sites. Emission intensity curve, for a particular exposure temperature, is obtainable from the superimposition of all emission curves characterized by lower activation energies.

- Studies about desorption kinetics show a first order kinetics for H_2 desoprtion, so a desorption directly proportional to exposed dose. The desorption energy obtained by TDS is about 3 kJ/mol, according with theoretic value.

The same measurements were conducted for Kr adsorption on single walled carbon nanotubes (SWNT) at very low pressure to verify that noble gas adsorption is characterized by a first kinetic-order. We observed that intensity of gas emitted is proportional to Krypton uptake and the peak of maximum temperature moves to high temperature increasing gas dose. It shows that krypton adsorption is described by zero order kinetics.
Our results confirm that carbon nanotubes are good gas absorber according with works in literature, but the originality is that our measures were effectuated under high vacuum conditions and for T_{ad} below the liquid nitrogen temperature (77K). So we confirmed the realistic possibility of using carbon nanotubes as cryosorbers, also for noble gases.
The Thermal Desorption Spectroscopy application to Astrophysics consists in the study of electron bombardment effects on ammonia and methane ices.
In the interstellar medium, composed for 99% by gas, molecules, atoms and radicals at gas state condense on dust grains surface of molecular clouds (at 10 K) creating an icy mantle with a thickness of 0.1 μm. Presence of this icy mantle, containing mainly H_2O, CO, CH_4 and NH_3, was confirmed by IR spectroscopy of obscured stellar sources**.** Interstellar ices are subjected to bombardment of photons and cosmic rays, with the consequent synthesis of new organic species.
This work investigate the effects of electron bombardment (with energies in the range 500-3000eV) on ammonia and methane ices (in conditions reproducing interstellar ices) to

confirm the synthesis of new organic specie as diazene (N_2H_2), ethane (C_2H_6) and acetylene (C_2H_2).

Zheng et al. **[37]**) reported the synthesis of hydrazine (N_2H_4) and diazene (N_2H_2) by irradiating solid ammonia at low temperature (10-60 K) with high energy electrons (5 keV). Our experiments suggest that also at lower energy of irradiation some chemistry occurs

Finally, for TPD application Geophysics, we analyzed a sample zoisite furnished by prof. Ajò from "Institute of Inorganic Chemistry and Surfaces" of CNR, in Padova.

We investigated zoisite behaviour during heating from room temperature to 650^{o}C to understand if its modification into a violet-blue variety (tanzanite) after heating is due to structural changes or to a dehydration mechanism. Through Thermal Desorption Spectroscopy were analyzed products of zoisite heating (H, O, OH and H_2O) and, by a comparison between desorption spectra intensities and shapes, we noted that the main effect of zoisite heating is not the loss of primary elements as H or OH, but the dehydration. All species desorbed during TPD (H, O, OH) are the result of cracking fraction of water (released by zoisite during heating) operated by the quadrupole filament; in fact all spectra have similar intensities and shapes and this suggests that cracking faction mechanism produces these elements in the same proportion.

Bibliography

[1] J. Yates, The thermal desorption of adsorbed species, Methods of Experimental Physics, vol. 22

[2] Schroeder S. & Gottfried M., *Temperature –Programmed Desorption & Thermal desorption spectroscopy*, Advanced Physical Chemistry Laboratory, FU Berlin (2002)

[3] D.A.King, Surface Science 64,43(1977)]

[4] R.Gorte and L.D. Schnidt, Surface Science 76, 559 (1978)3]

[5] S.Glasstone, K.J.Laidler and H.Eyring, "The Theory of Rate Process, McGraw-Hill, New York, 1941

[6] P.A.Redhead, Vacuum 12,203. (1962)]

[7] P.A.Redhead, Trans. Faraday Soc. 57,641 (1961)]

[8] H.Pfnur, P.Feulner,H.A.Engelhardt and D. Menzel, Chem. Phys. Letters 59,481 (1978)

[9] Hollenbach and Salpeter 1971, Astroph. J. 163, 155

[10] Cazaux and Tielens 2004, Astroph. J. 604, 222

[11] Perets and Biham 2006, MNRAS 365, 801

[12] Pirronello et al. 1997, Astroph. J. 483, L131

[13] Manicò et al. 2001, Astroph. J. 548, L253

[14] Hornekaer et al. 2003, Science 302, 1943.

[15] Sofia and Meyer 2001, Astroph. J. 554, L221

[16] Snow and Witt 1996, Astroph. J. 468, L65

[17] Williams and Herbst 2002, Surface Science 500, 823

[18] Pontoppidan et al. 2004, Astron. Astroph. 426, 925.

[19] Boonman et al. 2000, in ISO Beyond the Peaks: The Second ISO Workshop on Analytical Spectroscopy (Salama et al. eds), p.67.

[20] Palumbo et al. 2008., Journal of Physics: Conference Series 101, 2002.

[21] Sandford, S.A., Allamandola, L.J., and Bernstein, M.P. 1997, In From Star Dust to Planetesimals, Astron. Soc. Pac. Conf. Ser., Vol. 122, Y.J. Pendleton and A.G.G.M. Tielens (eds.), ASP, pp. 201-213

[22] Tielens et al. 1991, Astroph. J. 381, 181

[23] Pontoppidan et al. 2003, Astron. Astroph. 408, 981

[24] Tielens and Hagen 1982, Astron. Astroph. 114, 245

[25] Cuppen and Herbst 2007, Astroph. J. 668, 294.

[26] Ceccarelli et al. 2007, in Protostars and Planets (Reipurth et al. eds.), p.47.

[27] Smith et al. 1989, Astroph. J. 344, 413

[28] Kouchi et al. 1994, Astron. Astroph. 290, 1009

[29] Roser et al. 2002, Astroph. J. 581, 276

[30] Hornekaer et al. 2003, Science 302, 1943

[31] Ayotte et al. 2001, J. Geophys. Res. 106, 33387]

[32] Rowland et al. 1991, J. Chem. Phys. 95, 1378

[33] Keane et al. 2001, Astron. Astroph. 375, L43

[34] Briggs et al. 1992, Origins Life Evol. Biosphere 22, 287]

[35] Jenniskens et al. 1993, Astron. Astroph. 273, 583

[36] Greenberg et al. 1995, Astroph. J. 455, L177

[37] Zheng et al. 2008, Astroph. J. 674, 1242

[38] http://webmineral.com/data/Zoisite.shtml

[39] R.G.Burns,Cambridge University Press, 114-115, 1970

[40] D.R.Hutton,Phys. C: Solid St. Phys, 4, 1251-1257, 1971;

[41] G.H.Faye and E.H. Nickel, Can. Mineral. 10, 812-821, 1971.

[42] E.Rodeghero,A. Martucci,M.Sacerdoti,F.DeZuane and D.Ajò, *Structural and optical characterization of blue and yellow zoisite from Merelani Arusha (Tanzania):a study of the changes induced by heating*, poster at SIMP-AIC Joint Meeting"Learn from and for the Planet Earth" (2008)

[43] B. Angerth et al., *The Cold vacuum System of the Large Hadron Collider*, CERN, At Division 1211 Geneva 23, 2467

[44] Gröbner, *Technological Problems related to the Cold vacuum System of the LHC*, CERN, Vacuum/volume 47 (1996)

[45] Gröbner, *The LHC Vacuum System*, Particle Accelerator Conference**,** vol.3 (1999).

[46] Gröbner, *Vacuum system for LHC*, CERN, Vacuum/vol 46 (1995)

[47] N. Mahne, Tesi di laurea: Properties of LHC vacuum chamber as studied by synchrotron radiation related techniques

[48] V. Anashin e al., Summary *of resent studies of cryosorbers for LHC long straight sections*, Proceedings of 2005 Particle Accelerator Conference, Knoxville, Tennesee.

[49] R.Attanasi, Tesi di laurea: *Nanotubi di carbonio*, Università degli studi di Lecce (2003)

[50] http://mavimo.netsons.org

[51] Dong Qian, Gregory J Wagner, and Wing Kam Liu, Min-Feng Yu, Rodney S Ruoff, Appl Mech Rev vol 55, no 6, November 2002]

[52] R. Saito, G. Dresselhaus, M. S. Dresselhaus, Physical properties of carbon nanotubes

[53] S. V. Rotkin & S. Subramoney, *Applied Physics of Carbon Nanotubes*, cap.2-7 (2005)

[54] M.S. Dresselhaus et al., *Physics of carbob nanotubes*, Carbon, vol. 33 (1995).

[55] Biao Kan , Jianning Ding, Ningyi Yuan, Junxiong Wang, • Zhigang Chen, • Xiaoshuang Chen, Nanoscale Res Lett (2010) 5:1144–1149

[56] S. Rotkin, S. Subramoney, Applied Physics of Carbon Nanotubes, Springer.

[57] E. Dujardin, T.W. Ebbesen, H. Hiura and K. Tanigaki, Capillarity and wetting of Carbon Nanotubes, Science 265, 1850-1852 (1994)

[58] A.C.Dillon, K.M.Jones,T.A.Bekkadahl, C.H. Kiang, D.S. Bethune & M.J. Heben, Storage of hydrogen in single-walled carbon nanotubes, Nature, vol. 386, 377-379 (1997)

[59] A. Thess, R. Lee, P. Nikolaev, H. Dai, P. Petit, J . Robert, C. **Xu,Y.** H. Lee, S. G. Kim, A. G. Rinzler, D. T. Colbert, G. E. Scuseria,D. Tomrinek, J . E. Fischer, and R. E. Smalley, Science **273,** 483-487(1996).

[60] S. Iijima and T. Ichihashi, Nature (London) **363, 603** (1993)

[61] D. Laplaee, P. Bernier, W. K. Maser, G. Flamant, T. Guillard, andA. Loiseau, Carbon (1997)

[62] P. M. Ajayan, T. W, Ebbesen, T. Ichihashi, S. Iijima, K. Tanigaki, andH. Hiura, Nature (London) 362, 522 (1993)

[63] P. Sudan, A. Zűttel, Ph. Mauron, Ch. Emmenegger, P. Wenger, L. Schlapbach, Carbon 41, 2377 (2003)

[64] T. Wilson, A. Tyburski, M.R. De Pies, O.E. Vilches, D. Becquet, M. Bienfait, J. Low Temp. Phys. 126, 403 (2002);

[65] B. Panella, M. Hirscher, B. Ludescher, Microp. and Mes. Mat. 103, 230 (2007)

[66] G. Vidali, G. Ihm, H.Y. Kim, M.W. Cole, Surf. Sci. Rep. 12, 133 (1991)

[67] K. Masenelli-Varlot, E. Mcrae, N. Dupont-Pavlovsky, Appl. Surf. Sci. 196, 209 (2002).

[68] M. Muris, N. Dufau, M. Binfait, N. Duponi-Pavlovsky, Y. Grillet, and J.P. Palmari, Langmuir 16, 7019 (2000)

[69] S. Talapatra and A.D. Migone, Phys. Rev. B 65, 045416 (2002).

[70] D.G. Narehood, J.V. Pearce, P.C. Eklund, P.E. Sokol, R.E. Lechner, J. Pieper, J.R.D. Copley, and J.C. Cook, Phys. Rev. B 67, 205409 (2003)

[71] Hui-Ming Cheng, Quan-Hong Yang, Chang Liu, Carbon 39 (2001) 1447

[72] Gibb, E.L., Whittet, D.C.B., Boogert, A.C.A., and Tielens, A.G.G.M. 2004, ApJS 151, 35

[73] Maret, S., Bergin, E.A., Lada, C.J. 2006, Nature 442, 425

[74] http://www.avsbuyersguide.org/refguide/

[75] Bubert, H., and Froben, F.W. 1970, The Journal of Physical Chemistry 75, 769.

[76] Tokue, I., and Iwai, M. 1980, Chemical Physics 52, 47

[77] Buck, U., Meyer, H., Nelson, D. Jr, Fraser, G., and Klemperer, W. 1988, J. Chem. Phys. 88, 3028.;

[78] Buck, U., and Lauenstein, Ch. 1990, J. Chem. Phys. 92, 4250.

[79] Muller, U., and Schulz, G. 1987, Chemical Physics Letters 138, 385;

[80] Muller, U., and Schulz, G. 1990, Chemical Physics Letters 170, 401;

[81] Muller, U., and Schulz, G. 1992, J. Chem. Phys. 96, 5924

[82] Sato, T., Shibata, F., and Goto, T. 1986, Chemical Physics 108, 147.

[83] Rejoub, R., Lindsay, B.J., and Stebbings, R.F. 2001, Journal of Chemical Physics 115, 5053

[84] Kurawaki, J., and Ogawa, T. 1984, Chemical Physics 86, 295.

[85] Scheffler & Elsasser, Physics of the Galaxy and Interstellar Matter**,**1988

[86] Whittet D.C.B**.** 1993, in Dust and Chemistry in Astronomy, ed. T.J. & D.A. Williams

[87] Hollenbach & Thronson, Interstellar Processes, H. A. 1987

[88] Schutte, Adv. Space Res. Vol.30, No.6,p1409-1417,2002

[89] Kaiser and Roessler,The Astrophysical Journal, 503:959-975, 1998

[90] Wada,Mochizuki and Hiraoka, The Astrophysical Journal, 644:300-306, 2006

[91] http://www.sisweb.com/referenc/source/exactmas.htm

[92] Quadrupole technical data

[93] Shirai T. et al., Atomic Data and Nuclear Data Tables, Vol. 80, No. 2, 2002

[94] http://www.mindat.org/min-4430.html

[95] Strazzulla and Baratta 1992, Astron. Astroph. 266, 434

[96] Mann, M.M., Hustrulid, A., and Tate, J.T. Physical Review 58, 340.

[97] Frost, D.C., McDowell, C.A., and Vroom, D.A. 1967, Canadian Journal of Chemistry 45, 1343.

Acknowledgements-

-Ringraziamenti

A conclusione di questo lavoro è doveroso ringraziare: il prof. Janos Nagy, del Dipartimento di Ingegneria Chimica dell'Università della Calabria, per averci fornito i campioni di nanotubi di carbonio; il prof. Innocenti per le misure effettuate al TEM; il prof Ajò, dell' "Instituto di Chimica Inorganica e delle Superfici" del CNR di Padova, per averci dato la possibilità di analizzare il minerale della zoisite; il prof. Pirronello, del dipartimento di Metodologie Chimiche e Fisiche per Ingegneria di Catania, per l'attenta collaborazione nelle misure di bombardamento elettronico sui ghiacci interstellari; il prof. Roberto Cimino, dei laboratori I.N.F.N. di Frascati, per la collaborazione nel progetto riguardante la "criopompe".

Al termine di questi tre anni di dottorato vorrei porgere un sentito ringraziamento a tutti coloro che mi hanno accompagnato e sostenuto in questo lungo percorso.

Il primo pensiero va alla Prof.ssa Assunta Bonanno, al Prof. Antonino Oliva ed al Prof. Michele Camarca, per avermi accolto a braccia aperte nel loro gruppo, per avermi indirizzato nel percorso di ricerca, per avermi sostenuto e difeso e per avermi manifestato una stima incondizionata, peraltro assolutamente reciproca.

Un ringraziamento ai tecnici Vito Fabio ed Eugenio Lipreti perché, senza la loro competenza e professionalità, sarebbe stato tutto molto più difficile.

Un saluto ed un particolare ringraziamento al Prof. Fang Xu perché, in questi tre anni, ha "monitorato" e seguito, passo dopo passo, la mia attività di ricerca, dandomi sempre nuovi stimoli scientifici.

Un ringraziamento a Giulio, perché il suo aiuto in questo percorso di ricerca è stato davvero prezioso, oltre che fondamentale. Grazie per la pazienza e la gentilezza mostratemi, per le spiegazioni, i consigli (scientifici e non) e la disponibilità incondizionata. E' stato davvero un onore lavorare con te.

Un saluto a tutti i colleghi con cui ho condiviso, oltre a quello universitario, un percorso altrettanto impegnativo come il Dottorato. Melissa, Sandro, Gianfranco e Gabriele, grazie di cuore ed in bocca al lupo per tutto!

Non posso non menzionare Valentino e Pasquale, ringraziandoli per l'infinità disponibilità mostratami in questi anni, per le risate ed i momenti spensierati (ed anche qualche pettegolezzo!), che hanno reso ancora più piacevole questo percorso.

Un carissimo saluto a Davide e Giacomo, sin dall'inizio compagni di avventura. Grazie per il sostegno, l'affetto e l'empatia. Caro Davide, la condivisione delle nostre ansie è stata un'ottima valvola di sfogo, insieme ad altrettante risate.. Caro Giacomo, come dimenticare quei mesi trascorsi a studiare e penare per l'esame di ingresso al Dottorato; tanti esercizi e tanti dubbi, ma, soprattutto, confidenze, battute (quell'accoppiata non mi è mai piaciuta! ahahahahah) e risate a più non posso! Un'esperienza che porterò per sempre nel cuore.

Un pensiero particolare a Marianna…Il merito di tutto ciò che ho imparato in questi anni è solo tuo. Grazie per la pazienza, la dedizione, il sostegno incondizionato, gli stimoli scientifici, intellettuali e morali.. Grazie, ancor di più, per le chiacchierate interminabili, i pettegolezzi, le risate, i consigli fraterni.. Grazie perché sei una grande amica, oltre che la migliore collega che si possa desiderare. Sono convinta che le nostre strade si separeranno soltanto da un punto di vista scientifico, perché è davvero raro incontrare persone del tuo spessore. Grazie di cuore.

Un ringraziamento ad Adele che, come sempre ha fatto e sempre farà, ha seguito questo mio percorso passo dopo passo, sostenendomi, incoraggiandomi e nutrendo in me una fiducia smisurata.

Grazie ad Alessandra che, anche da lontano, ha condiviso il mio cammino, incoraggiandomi, "rimproverandomi" e spingendomi a credere in me stessa per ottenere sempre il meglio.

Non posso non dedicare un infinito ringraziamento ad Andrea e Francesca ed ai miei genitori, perché mi hanno permesso di raggiungere questo traguardo così importante, lasciandomi libera di decidere, infondendomi serenità e facendomi sentire protetta ed amata.

Grazie di cuore a Matteo…Senza il tuo sostegno, senza la tua costante presenza, senza te questo percorso di vita non sarebbe altrettanto bello…

Beh, giusto perché siamo alla fine, credo un ringraziamento spetti anche a me stessa… Affrontando le paure, credendo di più nei propri progetti e nelle proprie capacità, con coraggio, dedizione e sacrificio si può arrivare lontano.. "Per aspera ad astra"!

Appendix

PHYSICAL REVIEW SPECIAL TOPICS - ACCELERATORS AND BEAMS **11**, 113201 (2008)

H_2 adsorption on multiwalled carbon nanotubes at low temperatures and low pressures

F. Xu,[1] M. Barberio,[1] R. Vasta,[1] P. Barone,[1] A. Bonanno,[1] and V. Pirronello[2]

[1]*Dipartimento di Fisica, Università della Calabria and INFN, Gruppo Collegato di Cosenza, 87036 Arcavacata di Rende, Italy*
[2]*Dipartimento di Metodologie Fisiche e Chimiche, Università di Catania, 95131 Catania, Italy*

(Received 16 July 2008; published 18 November 2008)

We present an experimental study on H_2 adsorption on multiwalled carbon nanotubes (MWCNTs) at low temperatures (12–30 K) and low pressures (2×10^{-5} Torr) using the temperature programmed desorption technique. Our results show that the molecular hydrogen uptake increases nearly exponentially from 6×10^{-9} wt. % at 24.5 K to 2×10^{-7} wt. % at 12.5 K and that the desorption kinetics is of the first order. Comparative measurements indicate that MWCNTs have an adsorption capacity about two orders higher than that of activated carbon (charcoal) making them a possible candidate as hydrogen cryosorber for eventual applications in accelerators and synchrotrons.

DOI: 10.1103/PhysRevSTAB.11.113201 PACS numbers: 07.20.Mc, 07.30.Cy, 29.20.−c

I. INTRODUCTION

Pumping of molecular hydrogen in the Large Hadron Collider is designed by installation of cryosorbers on cryogenic elements operating at very low temperatures [1]. Among many specific requirements for the best choice of cryosorbent materials, the adsorption capacity is certainly a discriminating factor. Though many types of cryosorbers have been tested in the past [2,3], active porous carbon is still the far most important cryosorbent material due to its high specific surface area and large pore volume [4–6].

Usually, three different techniques are widely applied to study the H_2 adsorption rate, capacity, sticking and capture probability, and storage in solids: the volumetric method, which measures the pressure drop owing to hydrogen absorption after loading the specimen contained in a constant volume [7]; the gravimetric method, which measures the sample weight changes due to absorption or desorption [8,9]; and the temperature programmed desorption (TPD) technique [10]. This latest measures the hydrogen signal during desorption in high vacuum using mass spectrometry; it is highly sensitive allowing one to study samples with masses even below 1 mg and is especially suited for loading of small quantities at low pressures.

In an earliest work, Dillon *et al.* estimated the hydrogen uptake by single walled carbon nanotubes to be 5–10 wt. % for adsorption conditions of about 0.5 bar and 273 K, followed by cooling and pumping to 133 K and 10^{-6} Torr [10]. The heat of adsorption determined from the TPD measurements was close to 20 kJ/mol. Wilson *et al.* measured isotherms of H_2 and D_2 deposited on single walled, closed end carbon nanotube bundles and observed two well distinct steps corresponding to adsorption on grooves/interstitials and the graphene surface [11].

In this work we present a TPD study on H_2 adsorption on multiwalled carbon nanotubes (MWCNTs) and on charcoal at very low pressure and temperatures as a function of gas dose. We show that the molecular hydrogen uptake decreases with the adsorption temperature and is in the order of 10^{-7} wt. %, that the desorption kinetics is of the first order, and that the desorption energy is 2.82 ± 0.16 KJ/mol. Comparative measurements indicate that MWCNTs have an adsorption capacity about two orders higher than that of activated carbon (charcoal) making them a possible candidate as hydrogen cryosorber for eventual applications in accelerators and synchrotrons.

II. EXPERIMENTAL

MWCNTs were synthesized by chemical vapor deposition using C_2H_4 and subsequently purified. As illustrated in Fig. 1, transmission electron microscopy (TEM) shows that

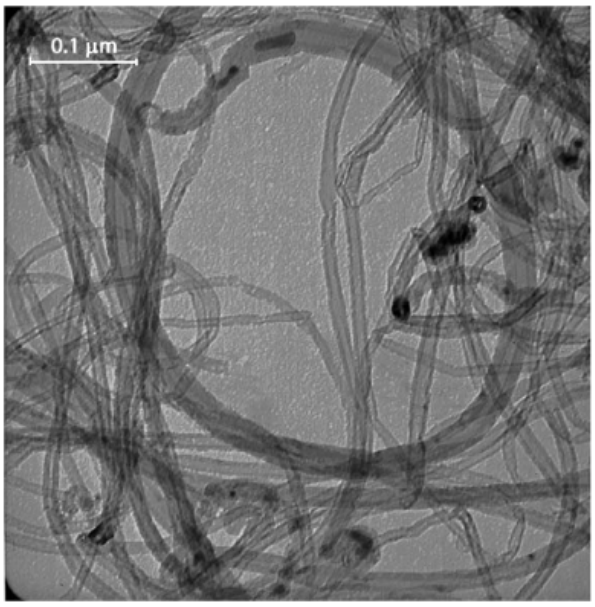

FIG. 1. Transmission electron micrograph of multiwalled carbon nanotube sample used in this study.

our MWCNT sample was made of individual nanotubes with an outer (inner) diameter of 10–15 (3–6) nm and that many of them were open ended. Microporosity measurements yielded a specific surface of 174 m^2/g. 10 mg of MWCNTs were dispersed in orthodichlorobenzene and sonicated in a glass container. The sample then was deposited directly onto the copper head (6 cm^2) of a cold finger with closed He cycling and dried. A quite uniform thin film was obtained and its adhesion to the copper surface remained stable during all the measurements.

The experiments were conducted in a UHV chamber (base pressure in the low 10^{-9} Torr range) evacuated with a dry turbo pump. H_2 gas (purity of 99.999%) was introduced in the chamber through a precision leak valve while keeping the sample at a desired adsorption temperature T_{ad} and a fixed pressure of 2×10^{-5} Torr (measured at room temperature and corrected for the ion gauge sensitivity factor) for a chosen time interval, then the gas was pumped out. The sample temperature was monitored with a Au/0.7%Fe-chromel thermocouple. Thermal desorption was achieved by heating the head of the cold finger with a linear ramp and the desorbed H_2 was measured with a quadruple mass analyzer. No appreciable contamination gas signals were detected neither in the adsorption nor in the desorption processes. Complete reversibility of charging and discharging cycles was routinely verified and a total reproducibility was observed.

The vacuum system pumping speed was calibrated by admitting a known quantity of hydrogen into the chamber at desired quadruple reading pressures and monitoring the time needed for evacuation. A linear dependence on the pressure was observed. The desorption rate was obtained by multiplying the detected hydrogen partial pressure (the integral intensity of a quadruple mass spectrum centered at $m = 2$ a.u. composed of some 50 data points) by the system pumping speed and the total amount of desorbed hydrogen then could be evaluated from the integration of the desorption rate-time curves with an estimated error of about 20%.

The density of MWCNTs should be close to 2 $g\,cm^{-2}$ once deposited on the cold finger in a compact form (not measured). For small quantities of our samples (up to

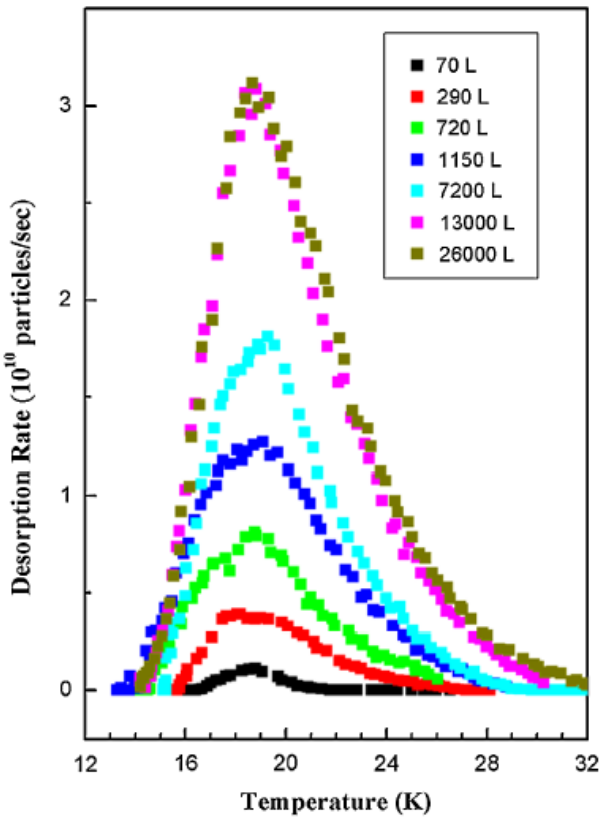

FIG. 2. (Color) Temperature programmed desorption traces of molecular hydrogen adsorbed at $T_{ad} = 15$ K and $P_{ad} = 2 \times 10^{-5}$ Torr. The dose is expressed in Langmuir (1 L = 10^6 Torr sec).

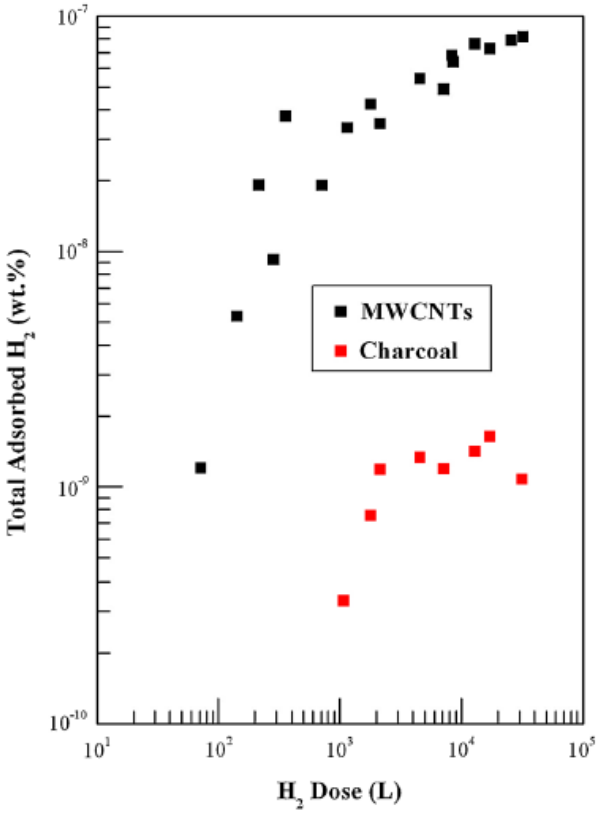

FIG. 3. (Color) Molecular hydrogen adsorbed on MWCNTs as a function of H_2 dose for adsorption temperature of $T_{ad} = 15$ K. Also shown are the results for a charcoal sample. The active surfaces are 174 m^2/g and 23 m^2/g for MWCNTs and charcoal, respectively.

10 mg on a surface of 6 cm^2), we found the sorption capacity is proportional to the sample mass.

III. RESULTS AND DISCUSSIONS

In Fig. 2 we illustrate some representative H_2 TPD traces taken at a constant adsorption temperature of $T_{ad} = 15$ K and varying exposure time. The H_2 dose Φ was expressed in units of Langmuir ($1\ L = 10^{-6}$ Torr sec) and the sample heating rate was fixed at $\beta = 5$ K/min. These spectra are substantially narrower than those previously reported in literature for H_2 dosing at higher temperatures and pressures [10,12]. These TPD traces are quite similar to each other and the spectrum maxima remain unchanged as the hydrogen adsorption increases clearly indicating a first order desorption mechanism.

The total molecular hydrogen content, as determined from the integral of the desorbed H_2 TPD trace curves, is plotted in Fig. 3 as a function of Φ for $T_{ad} = 15$ K. It is interesting to note that it increases linearly with Φ at low doses and saturates at about 8×10^{-8} wt.% for $\Phi \geq 10^4$ L. The saturation at a very low value and the relatively narrow line shape would suggest that hydrogen adsorbs only on a limited number of sites.

To gain some information on the hydrogen binding energy we varied the sample heating rate β for constant $\Phi = 2100$ L and $T_{ad} = 19$ K. In Fig. 4 we plot $\ln(T_{max}^2/\beta)$ versus T_{max}^{-1}, where T_{max} is the temperature corresponding to the desorption rate maximum. The slope of the linear fit yields a desorption energy of $E_{des} = 340 \pm 20$ K (or $E_{des} = 2.82 \pm 0.16$ KJ/mol).

It is interesting to note that, though there is a large body of experimental studies on hydrogen adsorption on carbon nanotubes because of its potential application as a storage material, very few measurements were undertaken below 77 K [11,13]. To the best of our knowledge, no experimental data are available in literature for adsorption at very low pressures. The binding energy value found in this study is lower than that for H_2 on graphite (480 K) [14] in accord with the isothermal adsorption measurements reported by Wilson *et al.* (3.3 kJ/mol) [11]. This suggests that hydrogen molecules mostly adsorb on the outer surfaces and the reduction in binding energy value is generally attributed to the surface curvature [11,15–17].

This site assignment is in accord with the TEM observation that our sample was essentially made of individual nanotubes (Fig. 1). On the other hand, adsorption on inner walls would imply a much stronger bonding [11,18] and

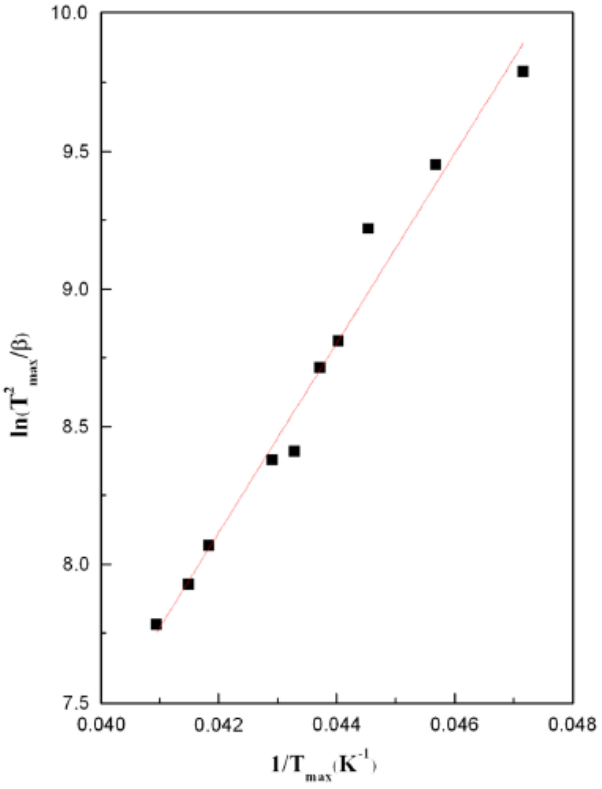

FIG. 4. (Color) Plot of $\ln(T_{max}^2/\beta)$ versus T_{max}^{-1} for a series of TPD spectra taken at fixed $T_{ad} = 19$ K, $\Phi = 2160$ L, and varying heating rate β. T_{max} is the temperature corresponding to the desorption rate maximum.

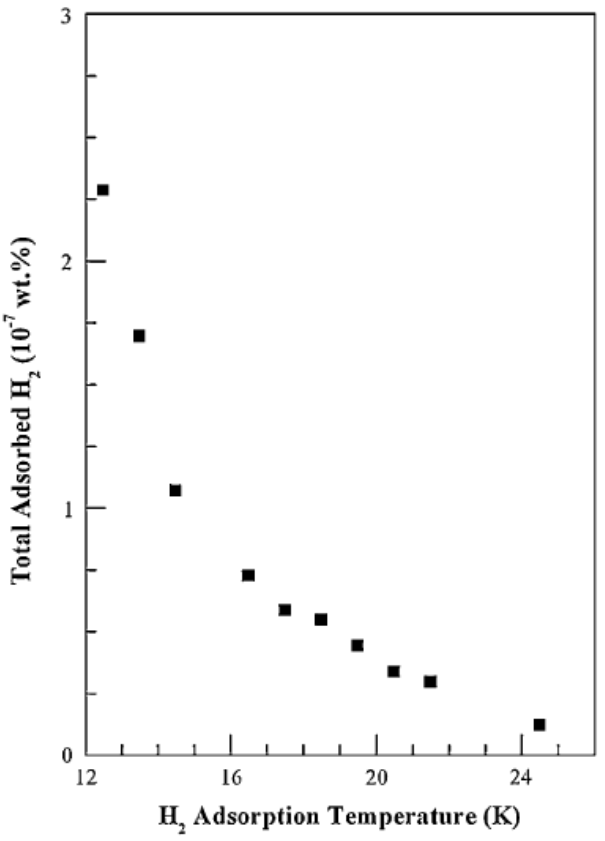

FIG. 5. Saturated molecular hydrogen content adsorbed on MWCNTs as a function of adsorption temperature of T_{ad}.

diffusion into those open ended nanotubes. Quasielastic neutron scattering measurements performed by Narehood *et al.* also indicated the absence of H_2 mobility in SWNTs at temperatures below 30 K [19].

For comparison, in Fig. 3 we also present the total H_2 adsorption amount of 10 mg activated charcoal powders (specific surface area 23 m^2/g) under exactly the same experimental conditions. It exhibits very similar characteristics as that of MWCNTs but is about two orders smaller.

Finally, in Fig. 5 we illustrate the saturated total amount of adsorbed hydrogen as a function of adsorption temperature T_{ad}. As expected, the total hydrogen adsorption capacity decreases with the cryosorber temperature. For $T_{ad} \geq 27$ K, no H_2 adsorption is observed.

Our results contrast sharply with those reported for hydrogen storage measurements at higher temperatures and pressures and strongly indicate that under high vacuum conditions, hydrogen does not adsorb on the nanotube surface beyond the sublimation temperature and the diffusion is essentially inhibited, as already confirmed by previous works. We mention that the testing measurements on carbon nanofibers actually used in the LHC were also taken at higher pressures and the so determined sorption capacity can be much higher than the real values in UHV conditions [5,6]. More quantitative works are currently being undertaken to determine the realistic possibility of using nanotubes as cryosorbers in UHV systems.

IV. CONCLUSIONS

In conclusion, we presented first experimental measurements of molecular hydrogen adsorption on MWCNTs at low pressures (10^{-5} Torr) and low temperatures (12–30 K). We showed that the adsorption capacity decreases sharply with temperature and is in the order of 10^{-7} wt. % at 12 K. This figure is about two orders higher than that obtained for commercial active carbon, making MWCNTs a potential candidate as cryosorbent materials for accelerators.

ACKNOWLEDGMENTS

We thank Professor Najy for providing us the MWCNT samples and Professor Innocenti for TEM measurements. This work is partly supported by INFN under the project of "NANOCS2."

[1] "*Vacuum system*," LHC Design Report V. 1 (12), CERN, 2005.
[2] T. Horiuchi and T. Ooi, Cryogenics **35**, 677 (1995).
[3] G. Moulard, B. Jenninger, and Y. Saito, Vacuum **60**, 43 (2001).
[4] C. Day, Colloids Surf. A **187**, 187 (2001).
[5] V. V. Anashin, R. V. Dostovalov, A. A. Krasnov, I. R. Collins, and O. B. Malyshev, Vacuum **72**, 379 (2004).
[6] V. V. Anashin, I. R. Collins, R. V. Dostovalov, Z. A. Korotaeva, A. A. Krasnov, O. B. Malyshev, and V. A. Poluboyarov, Vacuum **75**, 293 (2004).
[7] K. S. W. Sing, D. H. Everett, R. A. W. Haul, L. Moscou, R. A. Pierotti, J. Rouquerol, and T. Siemieniewska, Pure Appl. Chem. **57**, 603 (1985).
[8] E. Henneberg, B. Bernhardt, and K. Bohmhammel, Thermochim. Acta **415**, 43 (2004).
[9] M. Choi and R. Ryoo, J. Mater. Chem. **17**, 4204 (2007).
[10] A. C. Dillon, K. M. Jones, T. A. Bekkedahl, C. H. Klang, D. S. Bethune, and M. J. Heben, Nature (London) **386**, 377 (1997).
[11] T. Wilson, A. Tyburski, M. R. De Pies, O. E. Vilches, D. Becquet, and M. Bienfait, J. Low Temp. Phys. **126**, 403 (2002).
[12] P. Sudan, A. Zűttel, Ph. Mauron, Ch. Emmenegger, P. Wenger, and L. Schlapbach, Carbon **41**, 2377 (2003).
[13] B. Panella, M. Hirscher, and B. Ludescher, Microporous Mesoporous Mater. **103**, 230 (2007).
[14] G. Vidali, G. Ihm, H. Y. Kim, and M. W. Cole, Surf. Sci. Rep. **12**, 135 (1991).
[15] K. Masenelli-Varlot, E. Mcrae, and N. Dupont-Pavlovsky, Appl. Surf. Sci. **196**, 209 (2002).
[16] T. Wilson and O. E. Vilches, Physica B (Amsterdam) **329**, 278 (2003).
[17] M. Muris, N. Dufau, M. Binfait, N. Duponi-Pavlovsky, Y. Grillet, and J. P. Palmari, Langmuir **16**, 7019 (2000).
[18] S. Talapatra and A. D. Migone, Phys. Rev. B **65**, 045416 (2002).
[19] D. G. Narehood, J. V. Pearce, P. C. Eklund, P. E. Sokol, R. E. Lechner, J. Pieper, J. R. D. Copley, and J. C. Cook, Phys. Rev. B **67**, 205409 (2003).

HYDROGEN CRYOSORPTION ON MULTI WALLED CARBON NANOTUBES

F. Xu#, M. Barberio, R. Vasta, P. Barone, A. Oliva, L. Papagno, Dipatimento di Fisica, Universitàdella Calabria and INFN, Gruppo Collegato di Cosenza87036 Arcavacata di Rende, Italy.
V. Pirronello, Dipartimento di Metodologie Fisiche e Chimiche, Università di Catania 9513Catania, Italy

Abstract

We present a Temperature Programmed Desorption (TPD) study on H_2 adsorption on multiwalled carbon nanotubes (MWNT) at very low pressure (<10-6 Torr) and temperature (12-30 K). Our results show a hydrogen take up limit in the range of 10^{-8} mol per gram depending on the adsorption temperature. We compare the MWNT cryosorption capacity with that of commonly used activated carbon and discuss the possibility of employing MWNT as cryosorber in large particle accelerators.

INTRODUCTION

In the synchrotrons and colliders beams of charged particles circulate in a storage ring in circumference in cold bore vacuum chambers. The relativistic particles emit synchrotron radiations which deteriorate the vacuum by desorbing gases such as H_2, CO_2, CO, H_2O and CH_4 [1-2] from the walls. A solution of this problem is the installation of cryosorbers in the collider on cryogenic elements operating at very low temperatures. Several types of cryosorbers have been studied since a few years.

Due to its high specific surface area and large pore volume, porous carbon is considered as a good adsorbent [3]. A wide variety of commercial and speciality carbons has been tested so far as possible candidates for hydrogen sorption [4-6]. In particular, carbon nanotubes (CNTs) and carbon nanofibers show surprisingly high hydrogen storage capacity at either room temperature or liquid nitrogen temperature. Recently, a number of experimental studies of hydrogen adsorption on single walled carbon nanotubes (SWNT) has appeared in literature [4,7-11].

Usually, three different techniques are widely applied to study the hydrogen adsorption and storage in solids: the volumetric method, which measures the pressure drop owing to hydrogen absorption after loading the specimen contained in a constant volume [12]; the gravimetric method, which measures the sample weight changes due to absorption or desorption [13]; and the TPD technique. This latest measures the hydrogen signal during desorption in high vacuum using mass spectrometry, it is highly sensitive allowing to study samples with masses even below 1 mg and is especially suited for loading at low pressures. [3-10].

In an initial work, Dillon et al. [11] estimated the hydrogen uptake to be 5-10 wt.% for adsorption conditions of about 0.5 bar and 273 K, followed by cooling and pumping to 133 K and 10^{-6} Torr. The heat of adsorption determined from the temperature programmed desorption (TPD) measurements was close to 20 kJ/mol. This value should be compared to 4 kJ/mol for H_2 on graphite and with the theoretical 6.3 kJ/mol obtained for SWNT. [14-15] More recent work by the same group indicates that uptake of about 7-8 wt% is achievable on SWNT samples of high purity.[14-15]

Ye et al. [14] reported hydrogen adsorption on purified SWNT samples at 80 K over a pressure range from 0.5 to 160 bar. They observed very little adsorption at the lowest pressure. Similarly, Wilson et al. [15] measured isotherms of H_2 and D_2 deposited on single walled, closed end carbon nanotube bundles and observed two well distinct steps corresponding to adsorption on at least two different sites, grooves/interstitials and the graphene surface.

In this work we present some primary results of a TPD study on H_2 adsorption on multi walled carbon nanotubes (MWNT) and on activated graphite at very low pressure and temperatures as a function of coverage. We show that the hydrogen pumping efficiency can be greatly improved if carbon NTs are employed as cryosorbers.

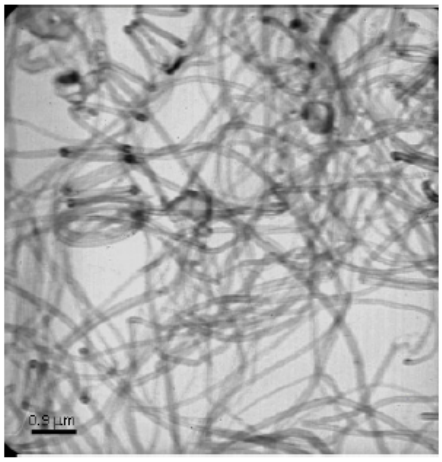

Figure 1: TEM image of the MWNT sample used in this study.

EXPERIMENTAL

The experiments were conducted in an ultra high vacuum chamber evacuated with a turbo pump. The camber base pressure was in the mid 10^{-9} Torr. Purified MWNT powder grown with CVD technique was dispersed in ortho dichrolobenzene, sonicated, and

#Corresponding author : xu@fis.unical.it

directly deposited on the head of a close cycled He cold finger. Sample temperature was monitored with a Au-0.7%Fe/Chromel thermo couple. H_2 gas (99.99% purity) was admitted to the chamber through a precision leak valve and the loading pressure was typically 10^{-6} Torr. During heating, the desorbed gases were analyzed by a quadrupole mass spectrometer (QMS), and the sample temperature was simultaneously recorded.

RESULTS AND DISCUSSION

In Fig. 1 we show a Transmission Electron Microscopy (TEM) image of our MWNT sample. It can be clearly seen that these purified nanotubes are caped and do not contain large amorphous carbonaceous particles and have quite similar diameters of 15 nm.

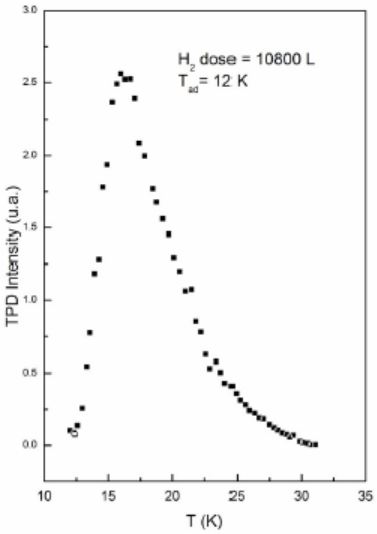

Figure 2: TPD spectrum for H2 dose of Φ=10800L on MWCT at an adsorption temperature of 12 K.

In Fig 2 we illustrate a typical TPD spectrum for H2 dose of Φ=10800L (1L=10^{-6} Torr s) on MWCT at an adsorption temperature of 12 K. Each data point in the figure actually is an integral QMS intensity at atomic mass units 2 and is proportional to the desorption rate. We mention that no water or other contamination signals were detected during either adsorption or desorption.

The total desorption intensity I_{tot}, area of the TPD curve as that shown in Fig.2, is directly proportional to the hydrogen uptake. In Fig. 3 we plot I_{tot} as a function of H_2 dose for 10 mg MWNTs at 16 K. It is interesting to note that I_{tot} increases linearly with Φ at low doses and saturates at about Φ=1000 L indicating that hydrogen adsorption does not go beyond one monolayer and the desorption kinetics is of the first order. We point out that the sorption process is completely reversible and the I_{tot} value remains unchanged within the experimental errors even after many sorption cycles.

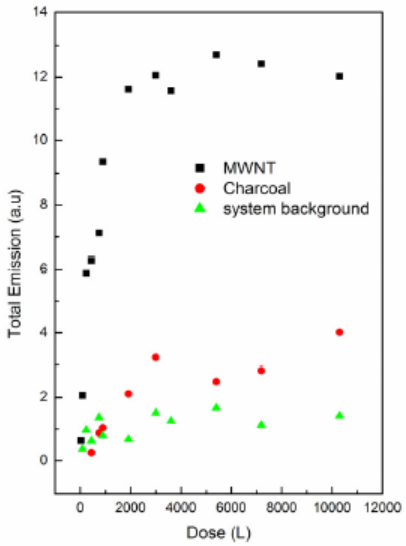

Figure 3: H_2 uptake as a function of adsorption dose at a constant condensation temperature of T=16 K. The data are obtained by integrating the total area of TPD spectra as those shown in Fig.2. Also shown are the results for the same amount of charcoal and for the system background without any cryosorber.

In Fig. 3 we also show the results for the system background adsorption without nanotube cryosorbers which clearly confirms that the H_2 uptake is entirely due to MWNTs. For comparison, the behaviour of 10 mg charcoal powders under exactly the same experimental conditions is also depicted. We see that it exhibits very similar characteristics as that of MWNTs but with a total hydrogen adsorbed amount about four fold smaller.

Finally, in Fig. 4 is plotted the saturated I_{tot} as a function of adsorption temperature T_{ad}. As expected, the total hydrogen pumping efficiency decreases with the cryosorber temperature. For T_{ad}>27 K, no H2 adsorption is observed.

Our results contrast sharply with those reported for hydrogen storage measurements at higher temperatures and pressures and strongly indicate that under high vacuum conditions, hydrogen do not adsorb on the nanotube surface beyond the sublimation temperature and the diffusion is essentially inhibited, as already suggested by some theoretical calculations. Unfortunately, to our knowledge, so far there is no work reported in literature concerning the molecular hydrogen adsorption on carbon nanotubes for Tad below the liquid nitrogen temperature (77K). More quantitative works are currently being undertaken to determine the realistic possibility of using nanotubes as cryosorbers in UHV systems.

We thank Prof. Najy for providing us the MWNT samples and Prof. Innocenti for TEM measurements.

REFERENCES

[1] V. Baglin, Vacuum Performances Estimation of the cryosorbers to be installed in the LHC LSS, Vacuum technical Note 04-06 EDMS N0: 478338, CERN – AT division (2004).

[2] B. Angerth, F. Bertinelli, J.-C. Brunet, R. Calder, J. Gomez-Goni, O. Grobner, A. Mathewson, A. Poncet, C. Reymermier and E. Wallen, the Cold vacuum System of the Large Hadron Collider, CERN, AT Division 1211 Geneva 23, 2467.

[3] Takefumi Horiuchi and Tsutomu Ooi, Cryogenic properties of composite materials, Cryogenics 35, 677 (1995).

[4] V.V. Simonyan, J. K. Johnson, Hydrogen storage in carbon nanotubes and graphitic nanofibers, Journal of Alloys and Compounds 330, 659 (2002).

[5] S. Hynek, W. Fuller, J. Bentley, Int. J. Hydrogen Energy 22, 601 (1997).

[6] J.S. Noh, R.K. Agarwal, J.A. SchWARZ, Int. J. Hydrogen Energy 12 693 (1987).

[7] Peng-Xiang Hou, Shi-Tao Xu, Zhe Ying, Quan-Hong Yang, C. Liu, Hui-Ming Cheng, Carbon 41 (2003) 2471.

[8] Hui-Ming Cheng, Quan-Hong Yang, Chang Liu, Carbon 39 (2001) 1447.

[9] C. Liu, Y. Y. Fan, M. Liu, H. T. Cong, H. M. Cheng, M. S. Dresslhaus, Science 286 (1999) 1127.

[10] K. Tada, S. Furuya, K. Watanabe, Physical Review B, 63 (2001)155405.

[11] A. C. Dillon, K. M. Jones, T.A. Bekkedahl, C. H. Klang, D. S. Bethune, M. J. Heben, Nature 386 (1997), 377.

[12] Y.-Y. Fan, B. Liao, Y.-L. Wei, M.-Q. Lu, H.M. Cheng, Carbon 37 (1999) 1649.

[13] R. Strobel, L. Jorissen, T. Schliermann, V. Trapp, W. Schultz, K. Bohmammel, G. Wolf, J. Garche, J. Power Sources 84 (1999) 25.

[14] Y. Ye, C.C. Ahn, C. Witham, B. Fultz, J. Kiu, A.G. Rinzler, D. Colbert, K.A. Smith, R.E. Smalley, Apll. Phys. Lett. 74 (1999) 2307.

[15] T. Wilson, A. Tyburski, M. R. DePies, O.E. Vilches, D. Becquet, M.Bienfait, Journal of Low temperature Physics, 126 (2002) 403.

Vacuum 84 (2010) 1025–1028

Contents lists available at ScienceDirect

Vacuum

journal homepage: www.elsevier.com/locate/vacuum

Changes in electronic properties of carbon structures by evaporation and implantation of alkali metals

A. Bonanno*, M. Barberio, P. Barone, M. Camarca, D.R. Grosso, R. Vasta, F. Xu, A. Oliva

Dipartimento di Fisica, Università della Calabria and INFN-gruppo collegato di Cosenza, 87036 Arcavacata di Rende, Cosenza, Italy

Keywords:
Autoionization
Auger spectroscopy alkali implantation
Carbon structures
Carbon nanotubes

A B S T R A C T

We report an electron spectroscopy study on Na^+ ion implantation and Na atom deposition on carbon structures. Our results show that, for implanted Na at the same ion dose, the Na surface concentration decreases with the structure order, while deposited Na particles readily diffuse in the bulk.

1. Introduction

Interaction of alkali metal atoms with carbon structures actually holds an important role in scientific research because of its implications in advanced technological applications. Graphite is a highly anisotropic [1] material in terms of its structural and electronic properties, due to the relatively strong in-plane forces between carbon atoms, and to the weak interplanar forces between adjacent graphene layers. Atoms of various chemical species, intercalated or implanted within graphite layers, form atomic or molecular bonds. The interest in these intercalated compounds is due to changes in electronic and mechanical properties induced by the intercalates, which can lead to technological applications of the new materials.

In particular alkali metals have been widely studied because they can act as potential donors when intercalated within graphite layers and because of their importance in catalysis and hydrogen adsorption processes [2–6]. In addition, technological applications of lithium graphite compounds have been introduced as rechargeable solid state Li^+ batteries [2]. Recently, the studies of carbon nanotubes have attracted much interest as energy storage and nanoscale device applications [7–9]. The studies on graphite alkali deposition provide information on the surface structures and on changes in the electronic properties [1,2,10]. It has been observed that some alkali metals form a (2×2) monolayer when deposited at low temperature [1], while, due to their small sizes, Na and Li behave in a different way: Li readily intercalates into the graphite even at 100 K [1]; Na at low temperature (110 K) forms monolayer islands [1]. At room temperature, alkali deposition on graphite is scarcely studied, while recent studies of alkali deposition on carbon nanotubes showed a rapid diffusion of alkali in the bulk [9,11,12] and changes in electronic properties.

Further, the resistivity of carbon nanotubes decreases upon exposure to alkali metals denoting a progressive sample metallization [13]; the most significant change in resistivity occurring for sodium exposure. Low energy Na^+ ion implantation [14] and Na atom intercalation exhibit a quite different dopant spatial distribution, as implanted alkali atoms remain on the surface while intercalated alkali particles readily diffuse into the bulk [9,14].

These results suggested to us to study the changes in carbon structure properties after sodium exposure and implantation at room temperature. As for carbon nanotubes, we employ the CEAES technique (Collisionally Excited Autoionization Electron Spectroscopy) [15]. This technique consists in the analysis of electrons emitted by autoionization decay of sodium atoms excited by electron promotion [16] in binary sodium-sodium collisions between a beam projectile and an atom previously implanted or evaporated on the target.

This electron spectroscopy induced by atomic collisional processes, allows us to monitor the amount of implanted ions by observing the change in intensity of such atomic features as a function of the dose of sodium projectile ions [14,17]. Through this spectroscopy we are able to study changes of the sample local electrostatic potential (work function) by observing the spectral lines shift under Na irradiation, since the kinetic energy of electrons emitted by atomic particles near the surface, is strictly related to the electrostatic potential difference between the sample and the analyser [15,17].

The full width at half maximum (FWHM) of observed lines can provide information about the homogeneity of the sample region beneath the decaying atoms [15,17,18]. In fact the de-excitation should take place at a distance of ~10 Å from the surface. The electrostatic potential seen by the emitted electron is thus an average over the (macroscopically very limited) underlying sample

* Corresponding author.
E-mail address: bonanno@fis.unical.it (A. Bonanno).

0042-207X/$ – see front matter © 2009 Elsevier Ltd. All rights reserved.
doi:10.1016/j.vacuum.2009.10.039

region, and the presence of impurities (for example, Na implanted atom) on the surface should inevitably cause a broadening of the spectral lines [15].

In this work, we report on a study of the interaction of slow Na^+ ions with several carbon structures. We observe that the concentration of implanted alkali atoms is larger for amorphous graphite, suggesting that the efficacy of doping decreases with the structure order and that, contrary to the case of alkali deposition on metal surfaces [15], where alkali atoms group together to form islands [19,20], Na atoms evaporated on carbon structures diffuse into the bulk.

2. Experiment

The experiments were performed in a UHV chamber with a base pressure of 6×10^{-10} mbar. The alkali ion gun is a Kimball Physics product, with a beam current in the nA range and a spot size of ~1 mm diameter. The ion beam incident angle was fixed at 50° with respect to the surface normal. The emitted electrons were collected by a hemispherical energy analyzer whose axis was along the surface normal. The Leybold analyzer has a semi-acceptance angle of 25° and operated at a constant pass energy mode ($\Delta E = 50$ eV), therefore at an approximately constant transmission over the measured energy range. For vapour deposition of sodium atoms, carefully outgassed SAES getter dispensers were used. The amorphous graphite, the highly oriented pyrolytic graphite (HOPG) and the single wall carbon nanotubes (SWNTs) (purities greater than 95%) samples were cleaned by the appropriate technique: heating cycles for amorphous graphite and for SWNTs and a stripping procedure for HOPG. In any case the degree of cleanliness was monitored by Auger spectroscopy once the sample was under UHV conditions.

3. Results and discussions

In Fig. 1 we show the spectra of electrons emitted by HOPG surface during 300 eV Na^+ irradiation. Our spectra show the well known features of kinetic electron emission with a broad continuum background on which narrow peaks are superimposed with widths typical of atomic transitions [14].

Such peaks are due to autoionization decay of sodium atoms excited in the states $2p^5 3s^2$ (Na I) and $2p^5 3s 3p$ (Na II) [21]. According to the molecular orbital (MO) promotion model, during the collisions of a sodium projectile with an implanted sodium atom, a transient quasi-molecule is formed [16]. In the framework of this model, the atomic Na 2p orbitals are correlated to the 3dσ and 4fσ molecular levels. If the internuclear distance between the collision partners decreases to below a critical value, some molecular orbitals will be shifted towards higher energies and electrons can be transferred to other unfilled orbitals. In the case of Na-Na collisions the models predict the promotion of the 4fσ MOs. Therefore, after the collision, Na atoms may have a vacancy in the 2p level and, when ejected into vacuum, will suffer autoionization decay producing the observed peaks. From Fig. 1 we can observe that such peaks rapidly grow in intensity and rigidly shift to lower energies as a function of Na^+ irradiation. Similar behaviour (not shown) has been observed for amorphous graphite and for SWNT and also for 700 eV Na^+ beam irradiation.

To get more detailed information we subtracted the smoothed background (as showed in the inset of Fig. 1) and fitted the peak with a Gaussian curve. In Fig. 2 we show the mean features of this Gaussian (Na I peak) as a function of Na^+ dose, D, where we compare the results obtained on HOPG, amorphous graphite and SWNTs for 300 eV and 700 eV Na^+ bombardment. The work function change $\Delta\varphi$ is given by the energy shift of the Na I peak,

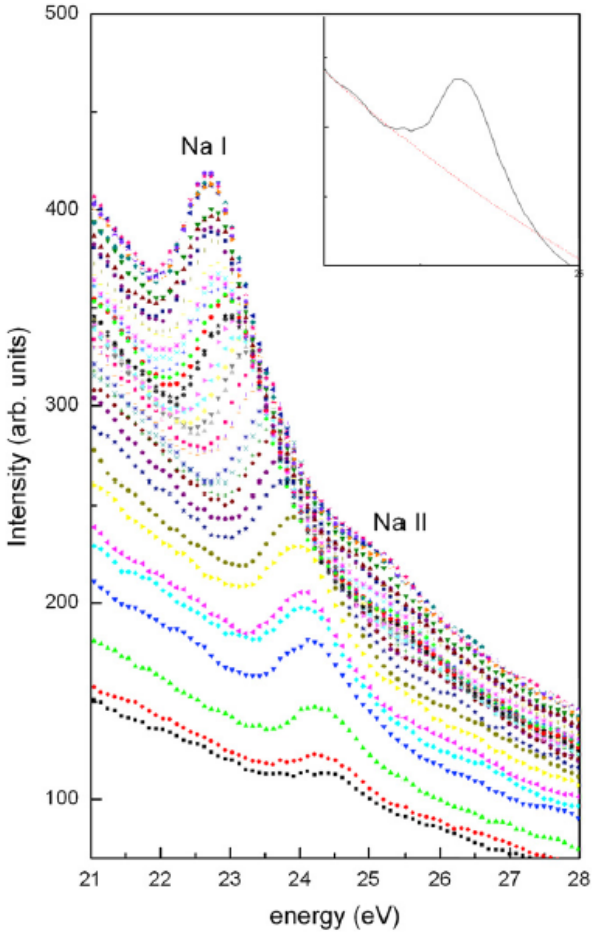

Fig. 1. Autoionization electron spectra taken during 300 eV Na^+ ion irradiation on HOPG. In the inset we show an example with the smoothed background subtracted.

assuming as reference position the peak energy extrapolated to zero dose. We attribute the reduction in the work function (φ) to the charge transfer from Na to the surface which results in the formation of a surface dipole [17]. Since the FWHM of the peak is linked to the broadening of spectral lines [15], this parameter supplies information on the spatial distribution of Na on the underlying surface, thus on the homogeneity of Na coverage on the surface. From the middle panel of Fig. 2 we can notice that the FWHM initially increases, then reaches a maximum and finally levels off. This reflects the initial inhomogeneity of the local electrostatic potentials and the gradual evolution toward a more uniform distribution of Na atoms on the surface. Additional information on the surface concentration of implanted Na is provided by the intensity of the autoionization peaks which has been obtained by evaluating the peak areas. In fact, it rapidly increases and gradually approaches a saturation value as D increases. The saturation intensity and the energy shift are significantly larger for the amorphous graphite for both energies of the irradiation beam as compared with the results for the other two ordered carbon structures (HOPG and SWNTs). This suggests that the dopant concentration on the surface decreases when the irradiated surface is a more ordered carbon structure. This seems to be in contrast with results reported in ref. [14]. Most likely this is because the sample used in [14], as pointed out in [22], conteined a large amount of amorphous carbon. Furthermore, the FWHM

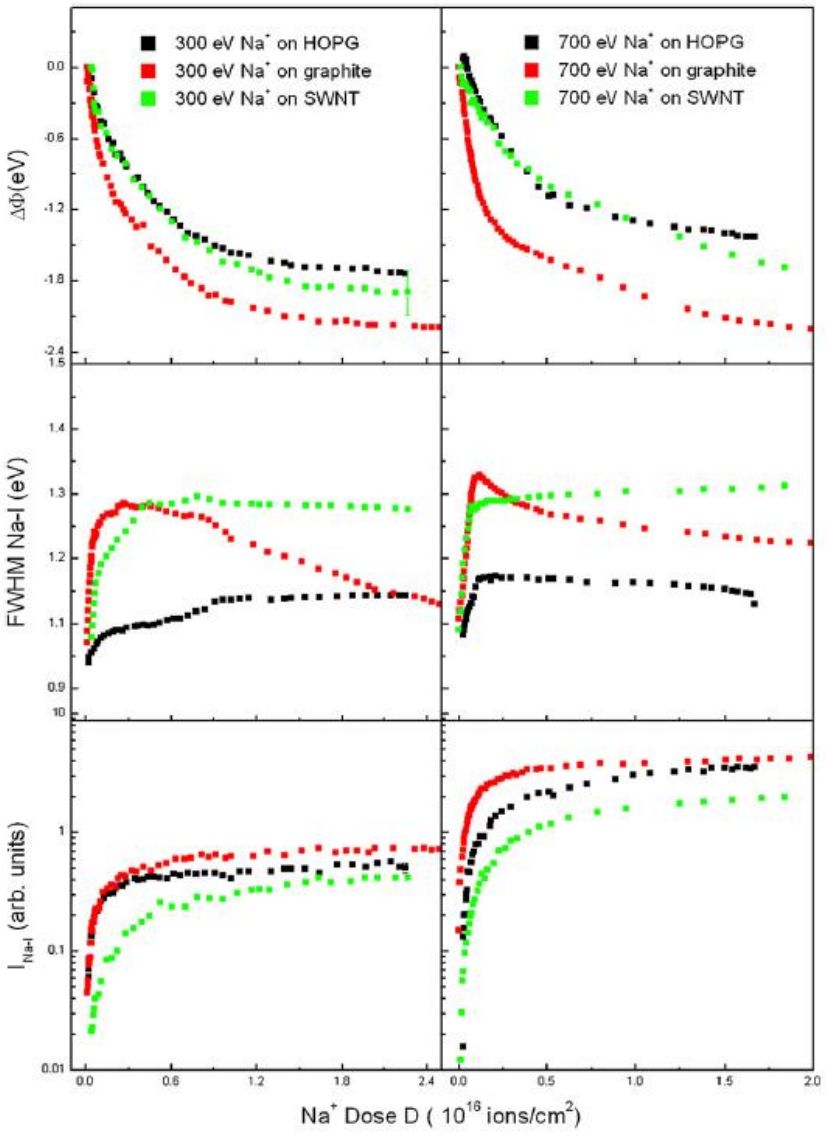

Fig. 2. Work function change $\Delta\phi$, linewidth, and intensity of Na–I autoionization peak versus Na^+ dose D for amorphous graphite, HOPG and SWNTs irradiated by 300 eV Na^+ ions (left panels) and by 700 eV Na^+ ions (right panels).

behaviour, in the case of a SWNT, shows that the dopant distribution on the surface is less homogeneous. This can be due to the disordered structures of SWNT bundles (Fig. 3) allowing the Na atoms to be implanted and/or diffused more easily into the sample. In the case of amorphous graphite the FWHM shows an increase due to the growing disorder of the initial surface as compared with HOPG. As the dose increases such differences almost disappear because, finally, there is a more uniform coverage of Na. In fact, if we increase the beam energy (right middle panel for 700 eV), the FWHM in the case of amorphous graphite levels off to a higher value due to the disorder induced by the bombarding beam. In additional studies we will investigate such behaviors at higher beam energies.

The CEAES spectroscopy has been used in the past [15,17,18] mainly for studies on alkali deposition on metal samples using outgassed dispensers. It is interesting to compare the results obtained on carbon structures after applying both techniques: alkali implantation and deposition. Recently we have observed [13] large changes in resistivity for deposition of alkali metals on carbon nanotubes. In Fig. 4 we show the spectra obtained for 300 eV Na^+

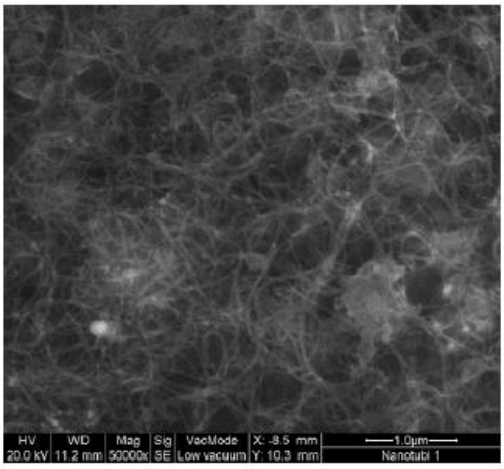

Fig. 3. Scanning electron microscopy images of SWCNT bundles.

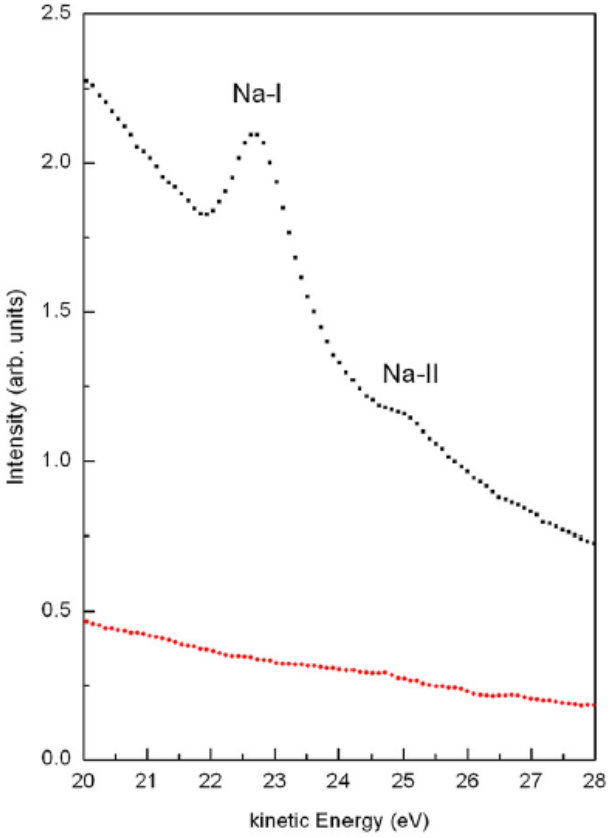

Fig. 4. Autoionization electron spectra induced by 300 eV Na^+ beam on SWNTs. The upper curve the spectrum after 300 eV Na^+ ion implantation, the lower one is for Na evaporation.

ion irradiation, for evaporated Na (lower curve) and implanted Na^+(upper curve). It can be easily seen that the autoionization peaks are completely absent in the case of Na evaporation. Similar results were obtained on the other carbon structures: amorphous graphite and HOPG. This confirms the results obtained in previous studies on carbon nanotubes exposed and bombarded by alkali atoms [9,14]. From such results we can deduce that alkali atoms, after deposition on carbon materials (amorphous, HOPG, SWNT) rapidly diffuse into the bulk structures.

4. Conclusion

From the intensity of the electron peaks it is found that implantation is more effective on disordered carbon structure (amorphous graphite) rather than on ordered carbon features (HOPG or SWNT). The effectiveness refers to the alkali concentration on the surface.

On the other hand, if we compare to the techniques used, we observe a difference between implantation and evaporation. Independent of the carbon structure used (ordered or disordered) our results show again that the implantation technique leads to a higher surface concentration of alkali atoms, or, in the case of evaporation, the alkali diffusion into the bulk is more probable.

References

[1] Caragiu M, Finberg S. J Phys Condens Matter 2005;17:R995–1024.
[2] Rytkonen K, Akola J, Manninen M. arXiv:cond-mat/0609458v1; 2008.
[3] Kotarba A, Holmlid L. Phys Chem Chem Phys 2009;11:4351–9.
[4] Mills RL, Zhao G, Akhtar K, Chang Z, Hea J, Lu Y, et al. Int J Hydrogen Energy 2009;34:573–614.
[5] Soo Han S, Mendoza-Corté s JL, Goddard WA. Chem Soc Rev 2009;38:1460–76.
[6] Purewal JJ, Keith JB, Ahn CC, Fultz B. Phys Rev B 2009;79:054305.
[7] Dai Hongjie. Surf Sci 2002;500:218–41.
[8] de Jonge N, Lamy Y, Schoots K, Oosterkamp TH. Nature 2002;420:393.
[9] Cupolillo A, Giallombardo C, Papagno L. Surf Sci 2007;601:2828.
[10] Breitholtz M, Algdal J, Kihlgren T, Lindgren SA, Wallden L. Phys Rev B 2004;70:125108.
[11] Suzuki S, Bower C, Tanigaki K, Zhou O. Chem Phys Lett 1998;285:481.
[12] Choi J, Samayoa IA, Chu Lim S, Chulso Jo, Choi YC, Lee YH, et al. Phys Lett A 2002;299:601.
[13] Barberio M, Barone P, Bonanno A, Camarca M, Masciari E, Oliva A, et al. Superlattices Microstruct 2009;46:369–73.
[14] Commisso M, Bonanno A, Minniti M, Barone P, Riccardi P, Oliva A, et al. Surf Sci 2007;601:2832–5.
[15] Xu F. Mod Phys Lett B 1995;9(6):319–41.
[16] Barat M, Litchten W. Phys Rev A 1972;6:211.
[17] Zoccali P, Bonanno A, Camarca M, Oliva A, Xu F. Phys Rev B 1994;50:9767.
[18] Oliva A, Mandarino N, Riccardi P, Zoccali P, Manicô G. Nucl Instrum Methods Phys Res Sect B 1996;116:420–3.
[19] Mandarino N, Zoccali P, Riccardi P, Bonanno A, Oliva A, Xu F. Nucl Instrum Methods Phys Res Sect B 1996;115:590–3.
[20] Riccardi P, Bonanno A, Oliva A, Xu F. Thin Solid Films 1996;289:177–9.
[21] Minniti M, Commisso M, Sindona A, Sicilia E, Bonanno A, Barone P, et al. Phys Rev B 2007;75:045424.
[22] Marianna Barberio PhD thesis –Dipartimento di Fisica, Università della Calabria- Italy; 2007.